40Ar behaviour and exhumation dynamics in a subduction channel from multi-scale 40Ar/39Ar systematics in phengite

Valentin Laurent, Stéphane Scaillet, Laurent Jolivet, Romain Augier, Vincent Roche

Journal Pre-proofs

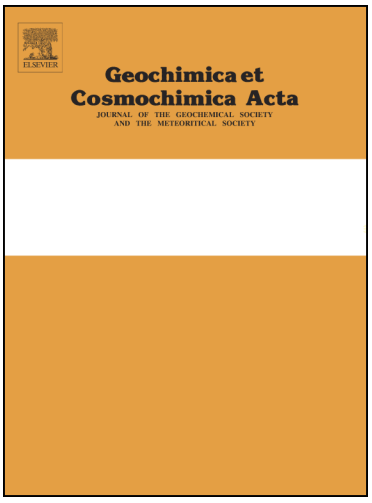

^{40}Ar behaviour and exhumation dynamics in a subduction channel from multi-scale ^{40}Ar/^{39}Ar systematics in phengite

Valentin LAURENT, Stéphane SCAILLET, Laurent JOLIVET, Romain AUGIER, Vincent ROCHE

PII: S0016-7037(21)00350-1
DOI: https://doi.org/10.1016/j.gca.2021.06.001
Reference: GCA 12244

To appear in: *Geochimica et Cosmochimica Acta*

Received Date: 26 September 2020
Revised Date: 15 March 2021
Accepted Date: 1 June 2021

Please cite this article as: LAURENT, V., SCAILLET, S., JOLIVET, L., AUGIER, R., ROCHE, V., ^{40}Ar behaviour and exhumation dynamics in a subduction channel from multi-scale ^{40}Ar/^{39}Ar systematics in phengite, *Geochimica et Cosmochimica Acta* (2021), doi: https://doi.org/10.1016/j.gca.2021.06.001

^{40}Ar behaviour and exhumation dynamics in a subduction channel from multi-scale $^{40}Ar/^{39}Ar$ systematics in phengite

Valentin LAURENT[1,2,3,5,(*)], Stéphane SCAILLET[1,2,3], Laurent JOLIVET[4], Romain AUGIER[1,2,3], Vincent ROCHE[4]

[1]Université d'Orléans, ISTO, UMR 7327, 45071, Orléans, France

[2]CNRS/INSU, ISTO, UMR 7327, 45071 Orléans, France

[3]BRGM, ISTO, UMR 7327, BP 36009, 45060 Orléans, France

[4]Institut des Sciences de la Terre Paris, UMR 7193 CNRS-UPMC, Sorbonne Université Paris, France.

[5] Present address: Imperial College London, Prince Consort Road, South Kensington, London SW7 2BP, UK.

[(*)] corresponding author

1. Introduction

Understanding the mechanical behaviour of subduction zones and unravelling the evolution of accretionary complexes requires addressing the key question of strain distribution within high-pressure low-temperature (*HP/LT*) shear zones. The complex interplay between rheology, temperature, fluid status, and deformation influences how exhumation of *HP/LT* units is accommodated by progressive localization of deformation along major crustal-scale shear zones. In *HP/LT* accretionary wedges, such strain localization and partitioning across the brittle/ductile transition may occur at large depths and, most notably, in the critical *T*-range (300-450 °C) overlapping with the argon (Ar) retention interval of *HP/LT* micas, i.e., phengite (e.g., Scaillet et al., 1992; Warren et al., 2012a). This has endowed phengite with the status of natural $^{40}Ar/^{39}Ar$ candidate for tracking temporal variations in shear distribution and exhumation dynamics of *HP/LT* units (Baldwin and Lister, 1998; Bröcker et al., 2004, 2013; Beltrando et al., 2013; Rogowitz et al., 2015; Fornash et al., 2016; Lister and Forster, 2016).

However, phengite is also known in such contexts to provide complex ^{40}Ar behaviour controlled by variable Ar diffusivity, mineral composition, parental lithology (juvenile protolith *vs.* polycyclic basement), deformation, and fluid/rock interactions (Scaillet et al., 1992; Scaillet, 1996, 1998; Giorgis et al., 2000; Di Vincenzo et al., 2006; Smye et al., 2013; Halama et al., 2014; Cossette et al. 2015; Schertl and Hammerschmidt, 2016; Fornash et al., 2016; Laurent et al., 2017). The resulting $^{40}Ar/^{39}Ar$ ages can be highly discordant and have been interpreted either in terms of closure or resetting, assisted or not by deformation. Accordingly, the extent to which $^{40}Ar/^{39}Ar$ phengite ages can constrain the thermal-kinematic behaviour of exhumed *HP/LT* rocks has been questioned and investigated using different approaches involving either *in situ* dating, bulk (population) dating, single grain step-heating or single grain fusion age distributions (e.g. Wijbrans et al., 1990; Monié and Chopin, 1991; Scaillet et al., 1992; Di

Vincenzo et al., 2006; Warren et al., 2012a; Beltrando et al., 2013; Smye et al., 2013; Laurent et al., 2017; Uunk et al., 2018).

In this work, we address these issues via the $^{40}Ar/^{39}Ar$ study of Syros and Sifnos, two key islands of the Upper Cycladic Blueschist (UCB) unit of the Aegean domain (Greece), one of the best preserved and exposed *HP/LT* subduction complexes worldwide (e.g., Hausmann, 1845; Ridley, 1982; Bonneau, 1984; Dixon et al., 1987; Schliestedt and Matthews 1987; Okay, 1989; Avigad and Garfunkel, 1991). Both islands record a major thermal-kinematic reworking marked by a sharp (ca.2 km–thick) metamorphic transition from eclogite and blueschist (*BS*) grade conditions to greenschist (*GS*) grade conditions. Our strategy is based on coupling thermobarometry, crystal-chemistry, and structural analysis with high-resolution *in situ* and step-heating $^{40}Ar/^{39}Ar$ dating. A key innovation of our approach is to combine these techniques to a level of integration never attempted before. In particular, we apply extensive (regional) $^{40}Ar/^{39}Ar$ sampling across strain gradients previously recognized at all scales through this transition (e.g. Laurent et al., 2016, 2018; Roche et al., 2016), down to the petrographic/mineral scale. We further explore the behaviour of the phengite $^{40}Ar/^{39}Ar$ system as a function of strain intensity, textural habitus, metamorphic grade, and synkinematic overprint from the regional (> 10 km) down to the mineral scale (< 1 mm).

2. Geological Setting

2.1 Geodynamic evolution of the Cyclades

The Aegean domain (eastern Mediterranean, Fig. 1) is characterized by two main tectonic and metamorphic events (Jolivet and Brun, 2010; Ring et al., 2010). The first one involves the convergence between Africa and Eurasia during Late Cretaceous-Eocene inducing

the formation of the Hellenides-Taurides chain (Bonneau and Kienast, 1982). A series of oceanic and continental units were accreted by underplating and mechanical coupling to the *HP/LT* nappe stack, which started to exhume through a set of syn-orogenic shear zones. These include the top-to-the E/NE Vari Detachment (Fig. 1, Trotet et al., 2001a; Soukis and Stockli, 2013; Laurent et al., 2016), the top-to-the-S thrust in Ios (Huet et al., 2009; Ring et al., 2010), and the top-to-the-E Pythagoras thrust in Samos (Roche et al., 2019). The second tectonometamorphic event corresponds to the progressive dislocation of the nappe stack as a consequence of the southward acceleration of the African slab retreat and tearing (e.g. Le Pichon and Angelier, 1981; Lister et al., 1984; Jolivet et al., 2004, 2013, 2015). The thickened crust of the Aegean domain was thus affected by post-orogenic extension, while the frontal zones were still under compression (Jolivet et al., 1994; Jolivet and Brun, 2010). In the Cyclades, detachment systems such as the top-to-the NE North Cycladic Detachment System (NCDS, Jolivet et al., 2010), the top-to-the S/SW West Cycladic Detachment System (WCDS, Grasemann et al., 2012), the top-to-the N Naxos-Paros Detachment System (NPDS, Gautier et al., 1993) and the top-to-the S Santorini Detachment (Schneider et al., 2018) accommodated back-arc extension and exhumation of the Cycladic Blueschist Unit (CBU, Fig. 1). During this phase, extensional tectonic was characterized by the development of Metamorphic Core Complexes (MCCs) on Naxos, Mykonos and Ikaria, where high-temperature parageneses overprint previous *HP/LT* parageneses at 21-17 Ma (Fig. 1, Lister et al., 1984; Wijbrans and McDougall, 1988; Urai et al., 1990; Gautier et al., 1993; Gautier and Brun, 1994; Jolivet and Patriat, 1999; Keay et al., 2001; Vanderhaeghe, 2004; Beaudoin et al., 2015; Laurent et al., 2015; Rabillard et al., 2018).

2.2 Geology of the Cycladic Blueschist Unit

The Cycladic archipelago (central Aegean domain) is mainly composed of the CBU (Fig. 1). This has been recently divided in two subunits: the Lower Cycladic Blueschist nappe (LCB) and the Upper Cycladic Blueschist nappe (UCB), which differ in lithology, geochemical record, and *P*-*T* conditions (Grasemann et al., 2018; Roche et al., 2018, 2019).

The LCB nappe is mainly observed in the southern and western parts of the Aegean domain (e.g., Serifos, Folegandros; Fig. 1). It is composed of metapelites, graphite-rich schists and marbles with minor metabasite (e.g. Grasemann et al., 2018; Roche et al., 2018). Published *P*-*T* data throughout this subunit indicate peak conditions of 10 ± 2 kbar and 400-500 ˚C (Katagas, 1984; Katzir et al., 2000; Baziotis et al., 2009; Iglseder et al., 2011; Augier et al., 2015; Scheffer et al., 2016; Grasemann et al., 2018; Roche et al., 2018).

The UCB nappe lies in the central part of the Aegean domain (i.e., the Cycladic archipelago, Fig. 1), and is particularly well exposed on Syros and Sifnos. On Syros, the UCB stack is classically subdivided in three subunits differing in lithology and predominant metamorphic facies (Laurent et al., 2016). These are from top to bottom the Kampos, Chroussa, and Posidonia subunits (Figs. 2, 3). The Kampos Subunit consists of a mélange of metabasites wrapped in serpentinites and minor metasediments. Eclogite- and *BS*-facies parageneses are spectacularly preserved and mostly escaped lower-*P* retrogression. The intermediate Chroussa Subunit is a lithostratigraphic sequence of alternating micaschists, thick marble layers and lenses of metabasite. Portions of this subunit are overprinted in the *GS*-grade facies while others show well-preserved eclogite- and *BS*-facies parageneses. The lowermost Posidonia Subunit consists of the structurally lower gneiss of Komito overlain by albitic micaschists with intercalated boudins of metabasite and thin marble layers. This subunit is pervasively overprinted in the *GS*-facies and shows only few preserved *HP* parageneses.

The UCB on Syros was exhumed in an overall top-to-the E non-coaxial shearing from eclogite-facies through *GS*-facies conditions (Trotet et al., 2001a; Laurent et al., 2016). Strain

localization occurred progressively toward the base of the UCB during the *HP-GS* transition, along ductile shear zones observed at all scales (Laurent et al., 2016), preserving *HP/LT* structures in the less deformed eclogite- and *BS*-grade topmost subunits (Figs. 2, 3). Similar shear zones were described on Sifnos where, as on Syros, the topmost part of the UCB shows well-preserved *HP/LT* parageneses relative to the highly *GS*-facies overprinted lowermost part (Roche et al., 2016). Despite their variable degree of retrogression, eclogite-facies parageneses are recognized throughout the UCB subunits of Syros and Sifnos with similar peak conditions around 22-20 kbar and 550 °C (Fig. 4; Trotet et al. 2001b; Groppo et al., 2009; Dragovic et al., 2012; Ashley et al., 2014; Laurent et al., 2018; Brooks et al., 2019). Laurent et al. (2018) recently refined the *P-T* exhumation path on Syros, suggesting a multi-stage evolution involving (1) a cold syn-orogenic exhumation within the subduction channel after peak metamorphic conditions, (2) isobaric heating at ca.12-10 kbar due to thermal re-equilibration of the lithosphere in the back-arc domain, and (3) exhumation and cooling related to post-orogenic extension. A quite similar *P-T* evolution of the UCB was also described on Tinos and Andros (Parra et al., 2002; Huet et al., 2015). The *P-T* record across the UCB is heterogeneous, the isobaric heating phase affecting to a lesser extent the topmost parts of the UCB (Kampos Subunit) than the intermediate and lowermost parts (respectively Chroussa and Posidonia Subunits, Fig. 4).

3. Previous geochronology

The timing of peak metamorphism in the UCB sequence has been constrained on Syros and Sifnos by U/Pb dating on zircon and Sm/Nd and Lu/Hf on garnet with ages ranging between 55-49 Ma (Fig. 4, Tomaschek et al., 2003; Lagos et al., 2007; Dragovic et al., 2015). Rb/Sr and $^{40}Ar/^{39}Ar$ dating of white mica from well-preserved *HP/LT* parageneses provided similar

(though more variable) ages between 55-30 Ma (e.g. Putlitz et al., 2005; Bröcker et al., 2013; Cliff et al., 2016; Lister and Forster, 2016; Laurent et al., 2017; Uunk et al., 2018).

Syros has been the focus of many (and especially $^{40}Ar/^{39}Ar$) geochronological studies (Fig. 4), mainly in the northern part featuring spectacularly preserved *HP/LT* parageneses (Tomaschek et al., 2003; Putlitz et al., 2005; Lagos et al., 2007; Bröcker et al., 2013; Rogowitz et al., 2015; Cliff et al., 2016; Lister and Forster, 2016; Laurent et al., 2017; Uunk et al., 2018; Skelton et al., 2019). There, Rb/Sr dating constrains the timing of retrogression from 42 Ma to as young as 25-21 Ma in *BS* and *GS*-facies associated with extensional fabrics. The syn-kinematic *GS*-facies retrogression and associated age range is mostly viewed as a continuum process rather than a single discrete event (Fig. 4, Bröcker et al., 2013; Cliff et al., 2016). The question as to which extent these data can constrain the timing of the *HP* to *GS*-facies transition remains open (Bröcker et al., 2013), however, Ring et al. (2011) obtained a well defined Rb/Sr phengite isochron at 22.8 ± 0.2 Ma (MSWD = 1.6) on *GS*-grade rocks of Sifnos contrasting with the scatterchron obtained on phengites from a pristine *BS*-grade sample at 29.4 ± 3.4 Ma (MSWD = 46). Such disequilibrium systematics are suggested to result from partial resetting of *HP* isotopic and chemical signatures by way of deformation-induced incomplete recrystallization during the *BS-GS* transition.

The latest contribution to the $^{40}Ar/^{39}Ar$ geochronology of Syros (Uunk et al., 2018) revealed the existence of phengite age gradients regionally correlated with metamorphic grade and overprinting with single-grain total-fusion ages ranging from 54 to 31 Ma. To get rid of local deformation effects, that study avoided targeting complex fabrics developed in connection with local and regional strain gradients. Also, the total-fusion approach of dating isolated single grains provides no textural control on intra- and inter-grains $^{40}Ar/^{39}Ar$ relationships. This is in contrast with our multi-scale approach that contributes *in situ* ages regionally and locally tied to deformation structures and metamorphic fabrics, allowing to substantially refine the

significance of local and grain-scale $^{40}Ar/^{39}Ar$ systematics in the context of the regional metamorphic transition.

4. Methods

4.1. Sampling strategy

As just stated, a major limitation of previous $^{40}Ar/^{39}Ar$ studies of the UCB has been the lack of exhaustive sampling to permit the ^{40}Ar record of *HP* phengite to be studied in connection with large-scale structures and metamorphic gradients and gaps recognized across the UCB stack. This has hampered the interpretation of $^{40}Ar/^{39}Ar$ ages lacking a clearly established link with (1) regional metamorphic gradients, (2) the finite strain pattern locally imposed by deformation across the eclogite/*BS*-*GS* grade transition, and (3) the isotope distribution at the mineral scale.

Our focus is on exploring the behaviour of the phengite $^{40}Ar/^{39}Ar$ system across strain gradients and regional strain distribution patterns previously studied by our group and others (Trotet et al., 2001; Rogowitz et al., 2015; Laurent et al., 2016; Roche et al., 2016). In these studies, strain gradients were qualitatively determined via standard field practice based on strain-intensity indicators such as: (i) the development of increasingly pronounced foliation (planar fabric) and stretching (linear fabric) toward the core of the shear zones (synkinematically elongated phengite, glaucophane, epidote, etc.), (ii) the development of shear structures such as shear bands and narrow ductile shear zones and C-S shear fabrics, (iii) mineral fish and sheared porphyroblasts, (iv) in some shear zones and toward their core, the progressive synkinematic retrogression from eclogite to *BS* or from *BS* to *GS*, and (v) the

192 progressive alignment/parallelisation of folds hinges with the direction of stretching toward the
193 core of the shear zone.

194 Based on these structural data, we applied a multi-scale $^{40}Ar/^{39}Ar$ sampling strategy to
195 provide, first, a regional coverage across the UCB and the overlying Vari Unit (Fig. 2) both
196 across the island and along the southern coast of Syros where all subunits are continuously
197 exposed and relationships between deformation and metamorphic recrystallization can be
198 observed. We next focused on individual shear zones previously studied in detail across
199 smaller-scale (ca. 500 m) sections (Lia shear zone, northern Syros, Laurent et al., 2016; Delfini
200 shear zone, western Syros, Rogowitz et al., 2015; Laurent et al., 2016; Chryssopigi shear zone,
201 southern Sifnos, Roche et al., 2016; Figs. 2, 3). These display characteristic high-strain
202 gradients distinctly developed across the eclogite-*BS* (Lia shear zone) and the *BS*-*GS* (Delfini
203 shear zone) metamorphic transitions on Syros. A further section developed entirely in the *GS*
204 facies (Chryssopigi shear zone, Sifnos), but characterized by variable extent of deformation-
205 assisted retrogression, was also investigated. Strain and facies variations suggest that these
206 shear zones were not coevally active during the whole exhumation and, thus, that they
207 potentially bear a distinct $^{40}Ar/^{39}Ar$ signature in connection with temporal variations in the 3-
208 D strain pattern at the scale of the UCB stack. Lastly, we applied spatially resolved (< 100 µm)
209 *in situ* UV-ablation on mm-scale rock sections from the targeted sections to investigate
210 $^{40}Ar/^{39}Ar$ systematics in connection with well-characterized microstructures and crystal
211 chemical patterns. Integration of the data collected through all scales is a major innovation of
212 this study that proved essential in understanding the temporal $^{40}Ar/^{39}Ar$ pattern recorded by
213 phengite in this part of the UCB.
214
215 4.2. EPMA analyses
216

Geochemical analyses of phengite crystals were performed to determine the degree of recrystallization in the studied samples, a key parameter to understand $^{40}Ar/^{39}Ar$ ages. A CAMECA SX100 electron probe microanalyzer (EPMA) housed at ISTO (Orléans, France) was used to acquire spot analyses of phengite. Analytical conditions were 15 kV accelerating voltage and 12 nA beam current with 10 s integration times for all elements (spot mode).

X-ray maps were acquired to check crystal-scale compositional variations in phengite (from half a mm to a few µm) and for linking geochemistry with microstructures and $^{40}Ar/^{39}Ar$ ages using a JEOL JXA-8230 instrument housed at ISTerre (University of Grenoble-Alpes, France; de Andrade et al., 2006). Mapping conditions were 15 kV accelerating voltage, 100 nA specimen current and 15 kV accelerating voltage, and 12 nA specimen current for spot analyses. Compositional mapping was carried out with dwell time of 200 ms and a step size (corresponding to the pixel size in the final image) of 2 µm. The X-ray compositional map was processed with the program XMAPTOOLS 2.2.1 (Lanari et al., 2014). Representative microprobe analyses of phengites from the $^{40}Ar/^{39}Ar$ analysed samples are provided in Appendix S3.

4.3. $^{40}Ar/^{39}Ar$ methods

We applied $^{40}Ar/^{39}Ar$ CO_2-laser step-heating on single grains and populations handpicked from the 0.5-1.0 mm fraction (single grains) and 0.25-0.50 mm (populations) obtained by gently crushing the samples. For spatially resolved UV-laser *in situ* mapping, diagnostic microstructures were drilled out from carefully sectioned samples, then cut and polished to 1 µm (adhesive such as superglue was not used) to obtain 0.9-1.3 mm thick × 10 mm circular rock sections. Rock sections, mineral grains and separates were washed in acetone, ethanol and de-ionised water in ultrasonic bath, dried at 50 °C in an oven, weighed and finally microscopically analysed and photographed.

All samples were irradiated for 5 h at Corvallis (CLICIT in-core position, Oregon, USA) along with sanidine standard FCT (28.02 ± 0.28 Ma, Renne et al., 1998) and analysed at the $^{40}Ar/^{39}Ar$ laboratory housed at ISTO (Orléans, France). Upon return from irradiation, they were unwrapped and placed in a stainless steel sample holder and loaded in a laser port pumped to ultra-high vacuum and baked to 195 °C over 48 hours. Extracted gases were purified using two air-cooled GP50 SAES® getters during 6 minutes before admission into the mass spectrometer. Ar and Cl isotopes were sequentially measured in 20 cycles with an electron multiplier (^{35}Cl, $^{36}Ar \pm {}^{1}H^{35}Cl$, $^{37}Ar \pm {}^{37}Cl$, $^{38}Ar \pm {}^{1}H^{37}Cl$, ^{39}Ar, ^{40}Ar isotopes) and a Faraday cup (^{40}Ar only) by peak-switching on one of the three static noble gas Helix-SFT® (Thermo Fisher Scientific, GmbH) mass-spectrometers operated at ISTO with a mass-resolution in excess of 750. Gas handling and mass-spectrometer operations are fully automated using stand-alone LabView-based software. Procedural blanks were monitored according to their evolution: every third heating step (typically the initial low-*T* heating steps featuring little or no ^{39}Ar) to every sample gas admission (all *in situ* experiments and mid to high-T extraction steps) in the same conditions as the sample. Typical values were 0.1 fA, 0.001 fA, 0.001 fA, 0.001 fA, and 0.001 fA for m/e = 40, 39, 38, 37, 36, respectively. Data regression and age calculations/corrections were made following Scaillet (2000). Regressed $^{40}Ar/^{39}Ar$ isotopic data are tabulated in the supplementary material. Individual age errors include propagation of all instrumental and procedural uncertainties. Plateau ages (PA) are calculated as integrated (inverse-variance weighted) mean ages over the corresponding steps, and total-gas ages (TGA) by individually summing the Ar isotopes of all steps (equivalent to a K-Ar age). These are quoted at ± 1σ.

Phengites were step-heated either as single grains (size permitting), or as small populations (clusters) typically comprising 6-7 grains, rarely more (up to 30 gains). For *in situ* dating, target-matching techniques were employed whereby the section surface analysed by SEM and probed with the EPMA was uncoated (i.e., repolished to 1 µm, then ultrasonically

rinsed in acetone and alcohol) to allow direct $^{40}Ar/^{39}Ar$ targeting of mineral zones and structures previously imaged and compositionally characterized by electron microscopy. A high-resolution deep 213-UV laserprobe (Photon Machines LXG2+ model) was used to excavate 100 to 50 µm–wide square or circular-shaped ablation pits about 50-70 µm–deep at a repetition rate of 20 Hz and 4-5 mJ/pulse. White light interferometry scanning of individual spots revealed steep-walled pits with variable bottom geometry (from nearly flat at integrated pulse counts < 600, to progressively cone-shaped due to progressive defocusing and internal reflections past 1000 pulses). Complete $^{40}Ar/^{39}Ar$ data are provided in Appendix S4 and S5. Except for a few analyses, $^{37}Ar_{Ca}$ and $^{36}Ar_{Cl}$ isotopes were all measured close to background values. Overall, they provide no insight on geochemical-ages relationships and are not discussed further below.

5. Results

5.1. Regional gradient: Southern Syros Section

5.1.1. Petrology, structure, and mineral chemistry

The most complete section across all subunits of the UCB and the Vari Unit can be studied sub-parallel to the regional E-W stretching lineation dominating across the southern part of Syros (Fig. 2, Laurent et al., 2016). This section shows strain gradients at all scales, across which 17 samples were collected for $^{40}Ar/^{39}Ar$ dating (Figs. 2, 3). The mineralogy and structure of the analysed samples as well as the petro-textural characteristics of phengite are described below and summarized in Tables 1 and 2.

Lowermost Posidonia Subunit. Three samples (SY-14-21, SY-14-18 and SY-13-02) were taken from the structurally lower felsic gneiss of Komito intercalated with boudins of

metabasite (Fig. 2). SY-14-21 is a chlorite micaschist partly overprinted in *GS*-facies conditions with the preservation of garnet and glaucophane. SY-14-18 is a Grt-Ep blueschist that was collected in the core of a metabasic boudin preserved from retrogression. Phengite is little deformed and compositionally homogeneous in this sample (Fig. 5). SY-13-02 is a gneissic sample, strongly foliated and showing top-to-the E shear bands. Phengite shows a spread in composition with no clear correlation with microstructures (Fig. 5). SY-16-10, SY-14-80, SY-14-76 and SY-14-77 were collected in the metapelite sequence pervasively overprinted in the *GS*-facies composing the upper parts of the Posidonia subunit (Fig. 2). SY-16-10 is a calcschist with coarse-grained primary phengite crystals. SY-14-80 is a strongly stretched and sheared *GS*-facies micaschist displaying top-to-the E kinematics with fine-grained secondary phengites set in a quartz matrix and oriented parallel to small shear bands (Fig. 5). Phengite composition is quite homogeneous and characterized by a low Si-content (Fig. 5). SY-14-76 is a weakly foliated and stretched chlorite-bearing calcschist statically overprinted in the *GS*-facies. Phengite is little deformed microscopically and is compositionally characterized by variable X_{Mg} values (Fig. 5). SY-14-77 is a strongly deformed metapelite overprinted under *GS*-facies conditions. There, phengite forms interconnected layers parallel to shear bands affecting a quartz and chlorite-dominated matrix. Phengite composition displays two distinct groups characterized by different X_{Mg} values (Fig. 5).

Intermediate Chroussa Subunit. Two samples were collected in this subunit (Fig. 2). SY-16-06 is a well-preserved *BS*-facies metabasite that is foliated and sheared (Fig. 6). SY-16-15 is made up of cm-scale phengite grains that were directly collected within the extensional gap of a neck formed at the tip of an eclogite boudin (Fig. 6). The association with glaucophane in the syn-kinematic neck indicates crystallization under *BS*-facies conditions.

Topmost Kampos Subunit. Five samples displaying varying degrees of retrogression were collected below the Vari Detachment, a major tectonic structure delimiting the *HP-LT*

317 UCB rocks from the amphibolite-facies Vari Unit (e.g. Trotet et al., 2001; Ring et al., 2003;
318 Keiter et al., 2011; Soukis and Stöckli, 2013; Laurent et al., 2016). Sample SY-14-40b is a
319 metabasite showing a complex deformation and retrogression pattern. While the top parts of
320 the sample (SY-14-40b_2) preserves a *HP/LT* mineralogy (glaucophane and garnet) affected by
321 both syn-*BS* top-to-the W and syn-*GS* top-to-the E shear bands, the base (SY-14-40b_4) displays
322 overprinted *HP/LT* minerals with only top-to-the E syn-*GS* shear bands (Fig. 7). This gradient
323 is mirrored by variations in phengite composition from the top (SY-14-40$b_{2,}$) to the base (SY-
324 14-40b_4). While the first shows homogeneous high Si-content, the second exhibits two distinct
325 compositional groups with a trend toward lower Si-content and X_{Mg} values from coarse-grained
326 phengites in foliation to fine-grained phengites in shear bands (Fig. 7). SY-14-60, SY-14-63
327 and SY-14-64 were collected from the same outcrop (Fig. 7). SY-14-60 and SY-14-64
328 correspond to eclogite boudins preserved in a strongly foliated *BS*-facies matrix. SY-14-63 is a
329 strongly foliated, m-long, *BS*-facies metabasic boudin. In these samples, some phengite crystals
330 are characterized by a high-Si core and lower-Si rims with a large Si *vs.* X_{Mg} compositional
331 span.

332 *Vari Unit*. Three samples were collected in the Vari gneiss (SY-14-68) and the
333 underlying mylonitic *GS*-facies metasediments (SY-16-18 and SY-13-10). None of these
334 displays evidence of *HP/LT* metamorphism. Phengite in SY-13-10 has a relatively
335 homogeneous composition similar to other UCB phengite (e.g. SY-14-40b_4, Fig. 7) while the
336 Vari gneiss SY-14-68 contains significantly lower X_{Mg} phengite (Fig. 7).

337

338 5.1.2. $^{40}Ar/^{39}Ar$ results

339

340 *Lowermost Posidonia Subunit*. $^{40}Ar/^{39}Ar$ step-heating of the phengite population SY-
341 14-21 yielded a complex age spectrum with apparent ages ranging from 35 Ma to 23 Ma (Fig.

8). The fine-grained population SY-14-18 yielded an overall flat age spectrum with a total gas age of 28.9 ± 0.5 Ma. The single grain SY-13-02 yielded a flat spectrum past the first three heating steps with an age of ca. 21 Ma for 93 % of total ^{39}Ar released. The paired phengite grains of SY-16-10 yielded a hump-shaped spectrum with apparent ages ranging from 26 Ma to 20 Ma (Fig. 8). The population SY-14-80 yielded a flat age spectrum with a plateau at 18.0 ± 0.1 Ma for 100 % of total ^{39}Ar released. This plateau corresponds to the youngest ^{40}Ar/^{39}Ar age obtained on Syros. A population of nine phengite grains from SY-14-76 yielded progressively increasing apparent ages ending with a flat segment at ca. 32 Ma over the six last heating steps (64 % of total ^{39}Ar released, Fig. 8). The phengite single grain SY-14-77, collected just below the contact zone delimiting the lowermost Posidonia Subunit and intermediate Chroussa Subunit (i.e. the Posidonia-Chroussa shear zone, Figs. 2, 3, Laurent et al., 2016), yields initially climbing low-T ages followed by a flat segment at ca. 20 Ma for 81 % of total ^{39}Ar released.

Intermediate Chroussa Subunit. The 3-grain phengite cluster SY-16-06, structurally located 10 m above the Posidonia-Chroussa shear zone, yielded three sharply increasing initial ages followed by a flat segment over the last six temperature steps around 38 Ma (67 % of total ^{39}Ar released, Fig. 8). The single phengite grain SY-16-15 yielded a slightly discordant age spectrum with apparent ages declining from 42 to 41 Ma. Additionally, 4 single phengite grains of different size were dated *in situ* (Fig. 9). Three crystals, SY-16-15b, SY-16-15c and SY-16-15d, yield very consistent apparent ages comprised between 45-40 Ma with broadly consistent TGA at 43.7 ± 0.3 Ma, 43.6 ± 0.2 Ma and 42.0 ± 0.2 Ma, respectively (Fig. 9). Interestingly, SY-16-15a, the larger and heavier grain, yields consistent but significantly younger *in situ* apparent ages with 88% of the data comprised between 38-35 Ma (TGA = 37.2 ± 0.2 Ma).

Topmost Kampos Subunit. ^{40}Ar/^{39}Ar step-heating of single grain SY-14-40b$_2$ yielded a decreasing age spectrum with apparent ages ranging from 30 Ma to 20 Ma (Fig. 8). The

measured amount of released ^{39}Ar for this grain is significantly lower than expected from sensitivity calculations assuming 10 wt.% K_2O, implying that this grain was not pure phengite but some interlayered phengite + paragonite ± chlorite. The population SY-14-40b$_4$ yielded a discordant age spectrum with apparent ages ranging from 40 Ma to 33 Ma (Fig. 8). Two paired phengite grains from SY-14-60 and SY-14-63 yielded equally discordant spectra with apparent ages varying between 44 and 40 Ma. The first five heating steps of SY-14-60 define a flat segment at ca. 42 Ma and the three consecutive steps an age of ca. 44 Ma for 55% of total ^{39}Ar released. SY-14-63 is characterized by an initial hump climbing to 44 Ma followed by a more regular segment stabilizing around 40 Ma at the end of degassing. The age spectrum measured on the 3-grain cluster SY-14-64 is characterized by a sharp increase of apparent $^{40}Ar/^{39}Ar$ ages over the first three degassing steps and by a flat segment at ca. 42 Ma over the last four steps comprising 60 % of total ^{39}Ar released (Fig. 8). *In situ* analyses were measured on rock-section SY-14-64 previously SEM mapped to study the relationships between composition, microstructures and $^{40}Ar/^{39}Ar$ record (Fig. 10). A coarse phengite crystal displaying a core to rim Si decrease show core ages of 46-43 Ma indistinguishable from those obtained in the lower-Si rim (45-43 Ma). Noteworthy, younger apparent ages of 38-35 Ma were measured in phengites of intermediate and lower Si-content located at the contact with a garnet and within a pressure shadow (Fig. 10).

Vari Unit (Fig. 8). The phengite population SY-16-18b yielded an erratic pattern with apparent ages ranging from 144 to 105 Ma, all characteristically older than any other sample elsewhere on Syros. The single grain SY-14-68 is characterized by a sharp increase of apparent ages over the first 4 temperature steps followed by a general decrease from 80 to 67 Ma (Fig. 8). A more consistent age pattern was obtained from the single grain SY-13-10 with a progessive increase from 42 to 59 Ma until fusion, closely mimicking a diffusive-loss profile.

Of particular interest, the earlier steps define the youngest ages obtained in the Vari Unit and are associated with the most deformed sample in the upper part of the Vari Detachment.

5.2. Local metamorphic and strain gradients.

5.2.1. Lia Shear Zone (Northern Syros): Eclogite to *BS* transition

Sample description and mineral chemistry

The northern part of Syros exposes the upper portion of the UCB (i.e. the topmost Kampos subunit), where the *HP/LT* parageneses are best preserved (Fig. 2). Increasing retrogression in the *BS*-facies is observed toward the Lia shear zone. While the less deformed samples preserve eclogitic parageneses, these are no longer recognized in the most deformed ones (Table 1), indicating strain localization early during exhumation.

Three samples were selected across this gradient (Fig. 2). SY-14-74 was sampled away from the shear zone (structurally 150 m below) in an undeformed eclogitic metagabbro showing no planar fabric (Figs. 11, 12). It is unaffected by the dynamic *BS* overprint, and thus serves as a local unretromorphosed reference. SY-14-71 was collected 100 m below the core of the shear zone, in an eclogite-*BS* metabasite included in serpentinite (Fig. 11). This sample is only incipiently deformed, probably recording the first steps of exhumation at the transition between eclogite and *BS*-facies conditions. Phengite is moderately deformed, compositionally homogeneous, and oriented parallel to foliation-forming glaucophane indicating growth near peak-pressure conditions. A rock section was cut across an omphacitic pressure shadow around a circular-shaped polycrystalline phengite aggregate, possibly a pseudomorph after lawsonite, embedded in a glaucophane-dominated matrix (± phengite, Fig. 12). This was analysed *in situ*

with the UV-laser probe and with the continuous-CO_2 laser probe on separated single grain (step-heating). SY-14-73 was collected within the Lia Shear Zone proper, where syn-*BS* grade deformation is extreme and marked by a strong planar fabric with top-to-the E kinematics (Figs. 11, 12). One step-heating experiment (single phengite grain) was conducted. Additionally, *in situ* $^{40}Ar/^{39}Ar$ UV-mapping was performed on a rock section drilled across a well-preserved syn-*BS* micro-shear band (Fig. 12).

$^{40}Ar/^{39}Ar$ results

Twenty-eight *in situ* $^{40}Ar/^{39}Ar$ ages were measured on SY-14-74 rock section (undeformed eclogitic metagabbro) with 25 analyses showing a homogeneous age distribution between 51 and 48 Ma (Fig. 12). The three oldest ages between 57-52 Ma are associated with a distinctly higher content in both ^{36}Ar and ^{37}Ar possibly indicating contribution from a shallow omphacite crystal hidden underneath the sample surface.

Step-heating of one single-grain of SY-14-71 (incipiently deformed eclogite/blueschist metabasite) resulted in a flat age spectrum with a total fusion age of 47.1 ± 0.2 Ma (Fig. 12). Thirty-three *in situ* analyses from this sample yielded ages vary between 49 and 45 Ma in the circular-shaped pseudomorph after lawsonite (Fig. 13) and more tightly grouped ages around 50-49 Ma in the eclogitic pressure shadow developed around it (four *in situ* analysis). This age range is broadly consistent with the one obtained for SY-14-74 (51-48 Ma). Less than 30% of the data are younger than 48 Ma (down to 42 Ma) and found in the main glaucophanitic matrix (Fig. 12). In stark contrast with the two previous samples, the 44 *in situ* apparent ages obtained on the strongly deformed SY-14-73 sample define a much broader range from 51 Ma (maximum age, shared with SY-14-74 and SY-14-71) to 23 Ma (Fig. 12). Of particular interest, the youngest apparent ages between 25-23 Ma are found both in little deformed coarse-grained

phengite away from the shear band as well as in fine-grained deformed phengite in the shear band. Note that this also holds for the older (51-45 Ma) and intermediate (45-30 Ma) apparent ages measured both within and away from the micro-shear band (Fig. 12). The companion single-grain age spectrum is characterized by a flat segment at ca. 39 Ma for 70 % of the total ^{39}Ar released (excluding the first and last step, Fig. 12).

5.2.2. Delfini Shear Zone (Central Syros): *BS* to *GS* transition

Sample description and mineral chemistry

Two *BS* to *GS*-grade shear zones cut across the Delfini peninsula on Syros (Figs. 2, 3, Laurent et al., 2016) characterized by intensely deformed rocks displaying a NE dipping foliation carrying a stretching lineation oriented E-W (Fig. 2). Asymmetric ductile deformation is characterized by top-to-the E kinematics indicated by shear bands and sigmoidal pressure shadows on garnets (Fig. 13). Six ^{40}Ar/^{39}Ar samples were collected across the shear zone and analysed by step-heating (Figs. 2, 3, Table 1). SY-16-23 is a *GS*-overprinted micaschist with pronounced foliation. Phengite is fine-grained and either intensely sheared or little deformed (Fig. 13). SY-14-30 is a metabasite preserving *BS*-facies minerals. Phengite is locally deformed in *BS*-grade shear bands, but otherwise parallel in the foliation. SY-14-24 is a *BS*-facies boudin of metabasite preserved in pervasively retrogressed *GS*-facies rocks. Again, phengite is intensely deformed in local shear bands but otherwise little deformed in the foliation (Fig. 13). The different textural habitus is paralleled by a trend toward lower Si and X_{Mg} content in phengite inside the shear bands. SY-14-26 is a retrogressed micaschist preserving coarse-grained garnet. This sample is intensely sheared with top-to-the E kinematics (Fig. 13). Phengite exhibits a similar trend toward lower Si and X_{Mg} content as in sample SY-14-24 (Fig.

13). SY-14-28 is a tightly folded garnet and glaucophane-bearing calcschist preserving *BS*-facies parageneses with primary phengite displaying relatively homogeneous composition and less deformation than previous samples (Fig. 13). SY-14-29 is a phengite-bearing marble displaying top-to-the W kinematic shear criteria previously studied by Rogowitz et al. (2014, 2015, 2016) for which they inferred extremely fast strain rates (10^{-10} s^{-1}) with grain-scale deformation partitioning into the weaker calcite crystals leaving phengite less deformed.

$^{40}Ar/^{39}Ar$ results

Step-heating of the fine-grained population SY-16-23 yielded discordant apparent ages comprised between 39-33 Ma (Fig. 14). The 6-grain phengite cluster SY-14-30 is characterized by ages slightly increasing from 34 Ma to 39 Ma and a flat segment at ca. 36 Ma for 60 % of total ^{39}Ar released (Fig. 14). Single grain SY-14-24 shows an initial increase over the first temperature step then a decrease from 34 to 31 Ma over a relatively flat segment at ca. 34 Ma (65 % of total ^{39}Ar released, Fig. 14). The single grain of SY-14-26 yielded a hump-shaped age spectrum with apparent ages ranging from 34 Ma to 29 Ma (Fig. 14). SY-14-28 and SY-14-29 single grains yielded two mutually consistent plateaux at 38.5 ± 0.2 Ma and 39.0 ± 0.2 Ma (Fig. 14), broadly concordant with the step-heating ages of 40 ± 1.6 Ma and 37 ± 1.3 Ma obtained in these marbles by Rogowitz et al. (2016).

5.2.3. Chryssopigi Shear Zone (Sifnos): *GS*-facies deformation

Sample description and mineral chemistry

A strain gradient associated with pervasive retrogression in the *GS*-facies was described on Sifnos as the Chryssopigi Shear Zone (Figs. 2, 3, Roche et al., 2016). In the regional-scale tectonostratigraphic sequence of the UCB, this shear zone is located within the lateral equivalent of the lowermost Posidonia Subunit of Syros (Roche et al., 2016). Top-to-the NE shearing gradually increases toward the core of the shear zone where fold axes are deflected parallel to the stretching lineation (Roche et al., 2016). The Chryssopigi Shear Zone displays the strongest *GS*-facies finite strain gradient observed in this study.

Eight $^{40}Ar/^{39}Ar$ samples were collected across the shear zone (Fig. 2). All samples are foliated and stretched, with deformation increasing toward the core of the shear zone (Fig. 15). Sample SF-14-55 is a foliated albite and epidote-bearing blueschist metabasite that was collected 300 m above the shear zone (Fig. 2). Two slightly different compositional groups are observed in phengite Si-content with no clear correlation with microstructures (Fig. 15). SF-14-52 is a *GS*-facies calcschist affected by top-to-the NE shearing. Phengite shows a trend toward lower Si-content within core-rim gradients (Fig. 15). SF-14-51 is a *GS*-facies calcschist with phengite characterized by a relatively homogeneous composition and little deformation (Fig. 15). SF-14-50 is a phengite-chlorite bearing marble overprinted under *GS*-facies conditions. Phengite is aligned in the main foliation and two distinct phengite compositions are characterized by different Si-contents with core-rim gradients (Fig. 15). SF-14-49 is a *GS*-facies calcschist showing top-to-the-NE shearing. Phengite appears either intensely sheared or little deformed with sectorial zoning toward lower Si-content, probably reflecting partial re-equilibration during exhumation (Fig. 15). SF-14-44 is a pervasively overprinted *GS*-facies micaschist sampled just above the core of the Chryssopigi Shear Zone and displaying top-to-the NE cm-scale shear bands. Phengite is relatively homogeneous with a low Si-content and slightly decreasing trend toward lower X_{Mg} values (Fig. 15). SF-14-43 and SF-14-39 are two pervasively overprinted *GS*-facies micaschists from the core of the shear zone proper (Fig. 15).

Phengite is intensely deformed and partially re-equilibrated (SF-14-43), with two well-defined compositional groups, or extensively recrystallized (SF-14-39), with a trend toward lower Si-content (zonal gradient and population trend, Fig. 15).

$^{40}Ar/^{39}Ar$ results

The grain pair and 6-grain phengite cluster of SF-14-55 yielded two mutually discordant spectra, the first with a plateau age at 21.5 ± 0.3 Ma distinctly younger (by about 3-6 Myr) than the companion age spectrum showing internally discordant ages between 26-22 Ma (Fig. 16). Two very similar (but internally discordant) age spectra were obtained from the single grain and 3-grain cluster of SF-14-52. Both age patterns evolve between 32 and 37 Ma and stabilize around 35 Ma near the end of the gas release. The minor internal variations occurring near the last steps of the single grain SF-14-52 may result from imprecise ^{36}Ar blank correction (Fig. 16). The phengite population SF-14-51 displays a flat age spectrum with a plateau age at ca. 35 Ma for 90 % of the total ^{39}Ar released. Single phengite grain SF-14-50 displays a hump-shaped age spectrum between 26-20 Ma with minor internal variations possibly reflecting imprecise ^{36}Ar blank correction after a large step again (Fig. 16). A discordant age spectrum was obtained from the 8-grain population of SF-14-49, with apparent ages wandering between 35-30 Ma with no well-defined trend. *In situ* laser ablation analyses (50 spots) of this sample are distributed between 38-22 Ma with the oldest apparent ages (38-30 Ma) found in undeformed phengites included in quartz and the youngest (30-22 Ma) in phengites located in shear bands (Fig. 17). The overall distribution is random, however, and apparently unrelated to microstructure with older ages also found in secondary shear bands. A discordant spectrum was obtained from the 3-grain cluster of SF-14-44 with initial ages rising from 22 to 28 Ma, declining to 23 Ma across a flat segment spanning the last 60 % of ^{39}Ar released (Fig. 16). The 7-phengite cluster SF-14-

43 is broadly similar in shape and total-gas age (23.4 ± 0.2 Ma). A similar age range is reproduced by the companion 33-grain population, yet with a slightly different discordant pattern. SF-14-39 provided two mutually discordant population age spectra (TGA = 20.8 ± 0.1 Ma *vs.* 22.7 ± 0.2 Ma), the 6-grain cluster appearing more regular with a flat segment over the last 8 steps defining an age of ca. 21 Ma (90 % of the total ^{39}Ar released, Fig. 16).

6. Discussion

We first discuss the ^{40}Ar/^{39}Ar systematics at the different scales investigated. These are then interpreted in terms of domainal-scale phengite Ar record involving (prograde) growth dynamics followed by dynamic overprinting in the *BS*- then *GS*-facies. We conclude with a short discussion of the regional implications of the new ^{40}Ar/^{39}Ar phengite data.

6.1. ^{40}Ar/^{39}Ar spatio-temporal trends

6.1.1. Regional ^{40}Ar/^{39}Ar trends across metamorphic transitions

Unlike previous geochronologic work mostly focused on the best preserved *HP-LT* occurrences in northern Syros (Bonneau, 1984; Wijbrans et al., 1990; Tomaschek et al., 2003; Putlitz et al., 2005; Lagos et al., 2007; Bröcker et al., 2013; Rogowitz et al., 2015; Cliff et al., 2016; Lister and Forster, 2016; Laurent et al., 2017; Uunk et al., 2018; Skelton et al., 2019), our ^{40}Ar/^{39}Ar sampling coverage across both Syros and Sifnos allows to study in much greater detail the correlation of apparent ages with deformation and retrogression throughout the different scales investigated (Fig. 18). Despite local complexities, and taken as a whole, the data reveal a clear regional trend toward younger ages from top to bottom across the UCB (Fig.

565 18). This finding is consistent with previous (but more local and scattered) studies on Syros
566 documenting an $^{40}Ar/^{39}Ar$ age decrease across the UCB, from the well-preserved eclogite-facies
567 samples at the top to the extensively developed *GS*-facies prevailing at the base (Maluski et al.,
568 1987; Putlitz et al., 2005; Bröcker et al., 2013; Rogowitz et al., 2015; Lister and Forster 2016;
569 Laurent et al., 2017; Uunk et al., 2018). Our oldest ages (51-48 Ma) come from *in situ* UV data
570 from the top of the UCB stack (Kampos Subunit, Figs. 10, 12). They are consistent with (or just
571 slightly younger than) previous Sm/Nd and Lu/Hf garnet ages and U/Pb zircon ages near 53-50
572 Ma interpreted to date peak-metamorphic conditions in *HP*-index rock types of Syros and
573 Sifnos (Fig. 4, Tomaschek et al., 2003; Lagos et al., 2007; Dragovic et al., 2015). *BS*-facies
574 metabasites from the intermediate Chroussa Subunit yielded consistently younger step-heating
575 or *in situ* $^{40}Ar/^{39}Ar$ ages between 41-37 Ma (Fig. 18). Samples structurally underneath in the
576 lowermost Posidonia Subunit provided still younger ages comprised between 35-18 Ma, all
577 together defining a coherent and progressive $^{40}Ar/^{39}Ar$ younging toward the base of the UCB
578 that correlates with the stronger *GS*-grade overprint of primary *HP* assemblages and the
579 associated progressive finite strain gradient described in previous studies (Fig. 18, Laurent et
580 al., 2016; Roche et al., 2016).

581 Similar to previous $^{40}Ar/^{39}Ar$ studies (e.g., Reddy et al., 1996; Dunlap, 1997; Rogowitz
582 et al., 2015) our data document a strong strain-age relationships with the youngest $^{40}Ar/^{39}Ar$
583 ages along the regional section corresponding to the more intensely deformed samples,
584 particularly those involving phengite (re)crystallization (here and in the following the term
585 (re)crystallization refers either to recrystallized phengite or to newly-formed phengites during
586 exhumation when these processes cannot be differentiated). This is illustrated by sample SY-
587 14-80 from the structurally deeper part of the section, which displays both the lowest average
588 Si-content in phengite (3.24 apfu) and youngest well-defined age plateau (18.0 ± 0.1 Ma; Figs.
589 5, 8). Except this extreme sample, there is no systematic correlation between phengite Si-

content and $^{40}Ar/^{39}Ar$ age across the entire section (i.e., with younger ages associated with decreasing Si-contents, Fig. 19). The compositional-age relationships are examined in more details at the scale of single shear zones below.

6.1.2. Local $^{40}Ar/^{39}Ar$ systematics across shear zones

A main result of our multi-scale approach is the observation that, across Syros, younger ages locally depart from the main regional trend close to (or within) highly deformed zones or lithologic contrast controlling strain localization and accommodation (Fig. 18). The 15 Myr gap found across the shear zone between the lowermost Posidonia and intermediate Chroussa subunits (between samples SY-16-06 and SY-14-77, Fig. 8) is one of such breaks in the regional trend. At the scale of a single shear zone, strain gradients are also mirrored by local $^{40}Ar/^{39}Ar$ age gradients (Fig. 18). The most ductilely deformed and retrogressed samples are correlated with the younger ages toward the core of all studied shear zones, including on Sifnos, with a maximum interval up to ca. 15 Myr in the Northern Lia (Syros) and Chryssopigi (Sifnos) shear zones (Fig. 18).

A compositional control is not apparent across these shear zones (Fig. 19). Age *vs.* phengite geochemistry relationships show poorly defined trends (R^2 = 0.08-0.15), similar to what observed at the regional scale along the entire section across Syros. The Lia and Delfini shear zones show a faint correlation between phengite Si-content and apparent ages, but without a well-defined trend in Si-content against the distance to the core of the shear zone (R^2 = 0.01, Fig. 19). Our results show that there is no first-order relationship between geochemistry and age either across the *GS*-grade Chryssopigi shear zone. Overall, while a slight $^{40}Ar/^{39}Ar$ younging is associated with (re)crystallization toward lower Si-content, the correlation is weak and the main drive for younging appears to be intracrystalline deformation rather than

615 composition. This is locally seen as a faint decrease of Si-content in phengite toward the core
616 of the shear zone, pointing to a greater degree of recrystallization/recombination associated
617 with increasing strain intensity and $^{40}Ar/^{39}Ar$ younging (Fig. 19). This is illustrated by samples
618 SF-14-39 and SF-14-44 that show the lowest average Si-content in phengite (3.40 and 3.38 apfu
619 respectively) and youngest $^{40}Ar/^{39}Ar$ ages obtained across the Chryssopigi shear zone (Figs. 15,
620 16).

621 Deformation is a major controlling factor for rejuvenation that is most spectacularly
622 illustrated by the *in situ* data collected across the Lia shear zone, north of Syros (Figs. 12 and
623 18). Grain-scale systematics from the three *in situ* rock sections sampled across the shear zone
624 (SY-14-71, SY-14-73, SY-14-74, Fig. 12) are discussed in the section to follow. The salient
625 feature they document at the scale of the shear zone (Fig. 3) is a progressive broadening of the
626 age range recorded *in situ* with the increasing synkinematic *BS*-grade overprinting (up to 23
627 Myr for the more deformed sample SY-14-73, *cf.* spectra in Fig. 12). Remarkably, deformation
628 at these conditions does not homogenize the ^{40}Ar signature toward a well-defined younger age
629 component. Instead, it produces mixed-scale inter-sample and within-sample age variations
630 spanning the entire range recorded across Syros.

631

632 6.1.3. Sample and grain-scale $^{40}Ar/^{39}Ar$ systematics

633

634 In terms of sample-scale $^{40}Ar/^{39}Ar$ systematics, two fundamental observations arise
635 from the *in situ* data, i) the absence of systematic correlation with microstructure, ii) the wide
636 range of ages locally recorded at the scale of a single specimen. Unlike the coupled
637 synkinematic overprinting and younging progression noted regionally, the *in situ* UV ablation
638 data show no relationships between microstructures, chemical composition, re-equilibrations,
639 and apparent ages at the scale of the rock sections. The most notable example is section SY-14-

73 across a *BS*-facies shear band that displays young ages around 25 Ma both in the core of the shear band and in coarse, little deformed, phengite aggregates away from the shear band (Fig. 12). A faint correlation can be observed between ages and microstructures in section SF-14-49 but the evidence is tenuous and far from systematic across the section (Fig. 17). In sample SY-14-64 (topmost Kampos subunit, southern Syros section), a compositionally zoned phengite crystal characterised by decreasing Si-content from core to rim was dated *in situ*. Results show undistinguishable apparent ages from core to rim (Fig. 10). Such a lack of correlation between $^{40}Ar/^{39}Ar$ age, microstructure, and mineral composition has been noted elsewhere in the UCB (Laurent et al., 2017), as well as in other *HP* localities worldwide (e.g., Scaillet et al., 1992; Di Vincenzo et al., 2006; Beltrando et al., 2013; McDonald et al., 2016; Fornash et al., 2016). Note that this is in other respects more faithfully documented here considering the better resolution afforded by our data (1σ typically round ± 0.5 Ma for spots just 100-65 µm wide). It is remarkable that large variations do exist between grains that are otherwise characterized by homogeneous within-grain patterns such as SY-16-15 (Fig. 9) characterized by static strain-free growth in an extensional gash.

In contrast with the lack of age-textural correlation, the interval (or range Δt) of *in situ* ages recorded by each section is correlated with the finite strain intensity and degree of retrogression recorded by each sample, much like the overall age *vs.* overprinting trend noted regionally. Indeed, Δt extends into progressively younger ages with increasing deformation and extent of retrogression through the sequence (Fig. 20):

(i) Δt = 3 Myr: undeformed eclogite SY-14-74 (51-48 Ma),

(ii) Δt = 9 Myr: slightly deformed eclogite/*BS* SY-14-71 (51-42 Ma),

(iii) Δt = 15 Myr: slightly deformed eclogite/*BS* SY-14-64 **(**50-35 Ma),

(iv) Δt = 26 Myr: intensely deformed *BS* SY-14-73 (51-25 Ma),

(v) Δt = 15 Myr: deformed *GS*-facies sample SF-14-49 (37-22 Ma).

Noteworthy, the Δt range in Syros samples anticorrelates almost perfectly (R^2 = 0.997) with the minimum age recorded in a given section, the trend collectively projecting to a nominal zero-spread ("undisturbed") end-member age at ca. 51 Ma (Fig. 20). This trend is tied to the remarkable preservation of a common maximum around 51-50 Ma in all these thin-sections despite their variable overprinting. Note that this trend is spatially unrelated to the sample distribution (both regionally or locally) and reflects the intrinsic degree of overprinting and the resulting heterogeneity recorded locally by the $^{40}Ar/^{39}Ar$ isotopes (sample-scale). Noteworthy, the sequence (i) to (v) above is broadly consistent with the age range spanned by the corresponding step-heating data in eclogite (54-49 Ma), blueschists (45-37 Ma), and greenschist-facies samples (35-18 Ma, Fig. 18), thus locally reproducing the trend seen regionally. Section SF-14-49 from Sifnos stands apart of the overall Δt trend essentially because it does not record any vestige of the 51 Ma *HP* age while exhibiting a modest Δt of only 15 Myr. Compared to the nearest analogue (in terms of degree of overprinting) still preserving a record of the *HP* event on Syros (SY-14-73 with Δt = 26 Myr), this break in trend in terms of internal heterogeneity correlates with the deeper structural position of this sample lying well within the regional *GS* grade overprint.

At the other end of the spectrum (i.e. lacking any *GS*-overprint) are the *in situ* $^{40}Ar/^{39}Ar$ data collected across the cleavage of the phengite flakes in the boudin neck of sample SY-16-15. These provide yet another indication of sub-homogeneous internal preservation of older ages varying from grain to grain (Fig. 9). The implications of these findings and how they may be interpreted section-wide across the UCB are discussed next.

6.2. Continuous *vs.* piecewise *HP* phengite growth

689 The coupled progression of post-*HP* deformation, phengite recrystallization, and *GS*-
690 facies overprint down-section across the UCB involved multiple mechanisms overlapping in
691 time and space. These include Ar diffusion, dynamic recrystallization, strain hardening and
692 shear localization, intracrystalline deformation and fluid-assisted dissolution/precipitation.
693 These mechanisms operated with potentially complex feedback relationships in P-T-t-X_{fluid}
694 space, making it inherently difficult to discriminate their respective or cumulative effects on
695 local $^{40}Ar/^{39}Ar$ systematics. However, close examination and quantitative evaluation of our data
696 allows a number of critical observations to be made that bear on the significance of $^{40}Ar/^{39}Ar$
697 phengite ages in *HP/LT* settings.

698 The consistent preservation of a common $^{40}Ar/^{39}Ar$ age maximum coeval with the 51
699 Ma *HP* age derived from Sm/Nd-garnet systematics both regionally (topmost sample from well-
700 preserved Kampos eclogite) and locally (UV *in situ* sections from the variably retrogressed Lia
701 Shear Zone; see also *in situ* data of Putlitz et al., 2005; Laurent et al., 2017 and the single grain
702 data of Uunk et al., 2018) indicates that this primary component is robustly recorded by
703 phengite on Syros. The lack of remanence of this component in step-heating spectra from
704 pristine *HP* samples dated here and elsewhere (Bröcker et al., 2013; Laurent et al., 2017; Uunk
705 et al., 2018), suggest that this component is irregularly preserved at the sample scale. The
706 apparent lack of such component in most step-heating data is probably genuine rather than an
707 artifact (e.g., in vacuo homogenization, cf. Sletten and Onstott, 1998). It is due to the low
708 probability of picking up fully-preserved, early-grown crystals from texturally complex *HP*
709 assemblages exhibiting grain-scale Ar variations resolved only by *in situ* dating.

710 Wijbrans and McDougall (1986), and later Putlitz et al. (2005), emphasized that episodic
711 or continuous *HP/LT* deformation may result in several microstructural generations in the same
712 sample. Putlitz et al. (2005) were among the first to show that even *HP*-static mineralogies can
713 contain grain-scale Ar disequilibrium interpretable as prograde crystallization ages during

protracted *HP* phengite growth. Our *in situ* data from SY-16-15 strengthen this interpretation by showing that texturally-equilibrated phengite flakes grown in a single, cm-scale, extensional gash at the tip of an eclogite boudins, record inter-grain age differences as high as 10 Myr while displaying homogeneous crystal-scale $^{40}Ar^*$ compositions (Fig. 9). Such inter-grain isotopic disequilibrium, if interpreted as temporally distinct crystallization ages, is along with Putlitz et al. (2005) the first *in situ* evidence of protracted *HP/LT* conditions recorded by punctuated phengite growth over 10 Myr at conditions presumably unable to eradicate steady-state radiogenic build-up. Coupled with the oldest *HP* age of 51 Ma, this constrains the minimum residence time at such conditions in the interval 51-37 Ma on Syros. More generally, this implies that pristine (static or dynamic) *HP* fabrics can potentially record a mixture of crystallization phengite ages in this range.

Grain-scale disequilibrium has already been reported from well-preserved *HP* mineralogies from the UCB recording complex $^{40}Ar/^{39}Ar$ age spectra varying in the range 51-37 Ma (e.g., Wijbrans and McDougall, 1986; Baldwin and Lister, 1998; Bröcker et al., 2004, 2013; Uunk et al., 2018; see also discussion in Fornash et al., 2016). Flat Eocene age spectra are comparatively rare. Among all *BS*-grade samples analysed by step-heating, we did not get any homogeneous (nor even near) plateau ages younger than ca. 40-38 Ma (cf. SY-14-28 and SY-14-29, Fig. 14). Coupled with the homogeneous grain-scale *in situ* ages of SY-16-15a (Fig. 9), this appears to set a lower limit about 37 Ma to syn-*BS* $^{40}Ar/^{39}Ar$ ages on Syros. Such older homogeneous ages are regarded here as time-resolved (i.e., discrete) *HP* crystallization events exceptionally preserved in the subduction channel. This bound expands significantly the time interval usually ascribed to the waning stages of the *HP* event from phengite Rb/Sr data (42-40 Ma, Bröcker et al., 1993, 2013). In this connection, we note that recent phengite Rb/Sr data from Syros have been found to record ages ranging from 42 Ma down to 30 Ma in *BS* facies assemblages associated with extensional fabrics linked to exhumation (Cliff et al., 2016). This

suggests that extensional deformation under *BS* facies conditions possibly lasted much longer than previously thought.

The preservation of closure/crystallization ages throughout a complete *HP-LT-t* loop in excess of 500 °C is consistent with theoretical residence time analysis (Lister and Baldwin, 1996; Baldwin and Lister, 1998; Warren et al., 2012a; Uunk et al., 2018), as well as empirical (Scaillet, 1998; Warren et al., 2011, 2012b) and more quantitative (Smye et al., 2013) fluid-rock integrated models suggesting that solid-state diffusional Ar kinetics in *HP* phengites may be strongly hindered by pressure (Harrison et al., 2009), fluid-kinetic-lithologic control (Scaillet, 1996, 1998; Giorgis et al., 2000), and compositional effects (Scaillet et al., 1992; Dahl, 1996). In a context such as the Cyclades where the intrinsic Ar-phengite retentiveness may be promoted by a steeply depressed *T/P* geotherm, our findings have far-reaching implications in terms of closed-system behaviour and crystal-growth kinetics. Using target-matching techniques (SEM + EMPA + UV laser ablation) coupled on the same rock sections (e.g., sample SY-16-15, Fig. 9), our $^{40}Ar/^{39}Ar$, mineral geochemistry and petrographic observations document sample-scale preservation of multiple *HP*-phengite generations, or sub-grain $^{40}Ar/^{39}Ar$ domains. This is evidence that replacement by dissolution-precipitation (± crystal-plastic flow) at static/dynamic *HP* conditions may be assisted by a grain-boundary fluid phase capable to drive off any Ar accumulated and released by prograde phengites recrystallized at or before near-peak conditions. This is corroborated by the single grain data from Andros by Huet et al. (2015), and the *in situ* data of Putlitz et al. (2005). On Syros as elsewhere throughout the UCB, Upper Eocene $^{40}Ar/^{39}Ar$ phengite ages are scanty but strikingly coeval with garnet Sm/Nd pulsatory growth ages (Dragovic et al., 2015). The narrow $^{40}Ar/^{39}Ar$ time span measured *in situ* in eclogite SY-14-74 (54-51 Ma, Fig. 12) and within the phengite flakes of SY-16-15 (37-43 Ma, Fig. 9) is commensurate with the garnet growth span determined by Sm/Nd dating on Sifnos (1-7 Myr, Dragovic et al., 2012, 2015). Such a convergence also

764 suggests extensive eradication at peak-*P* conditions of prior (prograde) $^{40}Ar/^{39}Ar$ phengite ages
765 which are no longer seen due to continuous recrystallization. By analogy with the Sm/Nd
766 record, phengite growth may be thus postulated to have been controlled by prograde, lithology-
767 buffered, phengite forming/breakdown equilibria. As discussed elsewhere (Scaillet, 1998;
768 Dragovic et al., 2015), these may keep the system open to continuous or pulsatory exchange
769 phenomena as the downgoing slab was experiencing devolatilization until peak-*P* conditions.
770 Eradication of prograde (i.e. pre-peak) features at peak-*P* conditions is qualitatively consistent
771 with the core-to-rim decrease in Si-content seen in most compositionally zoned *HP* phengites.
772 It is also expected from large-scale extensional deformation kinematic analysis indicating that
773 finite *HP* strain fabric in the UCB was predominantly acquired along the exhumation path
774 (Jolivet et al., 2003).
775
776 6.3. Thermal *GS*-grade resetting *vs.* dynamic overprinting
777 The spatial Δt *vs.* overprinting grade trend across Syros (Fig. 20) is qualitatively
778 consistent with the similar age *vs.* Δt trend found by Uunk et al. (2018) across the upper *HP*
779 subunit (Kampos) through the underlying (increasingly *GS*-overprinted) unit in the northern-
780 middle part of Syros (*cf.* their Fig. 9). A major difference is that our data record a spectrum of
781 intermediate ages at the scale of a single hand-specimen that goes well beyond the Δt of ca.10
782 Myr revealed by their total fusion experiments on single grains. This is most notably shown by
783 the wide age range recorded by SY-14-73 (Δt = 51-25 Ma, Fig. 20) that reproduces almost the
784 full spectrum measured at the scale of the entire UCB (Δt = 51-18 Ma, Fig. 20). Uunk et al.
785 (2018) focused their sampling away from local shear zones to get rid of complications due to
786 deformation. They observed that dispersion of the ages at the outcrop scale (100 m) is correlated
787 to grain size, suggesting thermally activated volume diffusion as a primary control on final
788 retention ages in the absence of deformation.

Quantitative Ar-closure modelling of the age *vs.* grain size relationships documented by Uunk et al. (2018) in the middle part of the Chroussa subunit (Myttakas section) allows to calculate sample-specific cooling rates assuming that Ar loss is controlled by the physical grain size across [001]. The inferred cooling rates reveal strong temporal variations between samples only 100 m apart (Fig. 21), with a major difference in temporal phasing near 38 Ma between their samples 12SR19 and 12SR16. The first records cooling at 24 °C/Myr near 40 Ma, then 9 °C/Myr at 38 Ma. The second 36 °C/Myr at 38 Ma, then 11 °C/Myr at 37 Ma, and finally 7 °C/Myr at 34 Ma. These calculations show that purely diffusion-controlled closure by monotonous and wholesale cooling cannot reproduce the age trend across the grain-size of these samples, unless by invoking sharply diachronous cooling at the scale implied (100 m). Such grain-size trends rather involve partial resetting (disequilibrium diffusion) complicated by inheritance and overlapping recrystallization, with variable retention of initial ^{40}Ar heterogeneities that the *GS* overprinting could not completely eradicate. This again reinforces the view that the UCB rocks probably left the *HP/LT* field with already considerable sample-scale ^{40}Ar* disequilibrium prior to the *GS* overprinting.

6.4. Domainal-scale Ar behaviour and the role of deformation

It is a general observation in the UCB that relict *HP* phengites yield increasingly complex (loss-like or hump-shaped) ^{40}Ar/^{39}Ar age spectra with increasing retrogression and progressive younging (e.g., Naxos: Wijbrans and McDougall, 1986; Tinos: Bröcker et al., 1993, 2004; Serifos: Schneider et al., 2011; Sifnos and Syros: Wijbrans et al., 1990; Bröcker et al., 2013; Lister and Forster, 2016; Andros: Huet et al., 2015). Many of the ^{40}Ar/^{39}Ar step-heating experiments in the present study provide non-ideal stepwise degassing patterns as well (Figs. 8, 12, 14, 16). Likewise, and except for the pristine eclogite sample SY-14-74 and the syn-

blueschist-facies phengite flakes of SY-16-15, the *in situ* data are also characterized by complex $^{40}Ar/^{39}Ar$ systematics.

Most of these spectra reflect mixing of heterogeneous populations or internal ^{40}Ar gradients as already pointed out by Wijbrans and McDougall (1986) and discussed above. Sharply defined age plateaus suggestive of simple fast cooling in the interval 35-25 Ma are the exception rather than the rule throughout the UCB. In many regional *HP-GS* transitional gradients recorded throughout the UCB, $^{40}Ar/^{39}Ar$ spectra generally become flat again only close to - or within - the *GS*-dominated domain (i.e. downward through the pile). On Syros, a strong age polarity has been evidenced from the texturally and isotopically well-preserved 51 Ma ages found atop of the pile toward the fully reset/recrystallized ages around 20-18 Ma at the base (including Sifnos). This is a characteristic feature across the UCB that brackets the transition from full retention to complete resetting, with intermediate ages in between reflecting the interplay between partial resetting/retention and full recrystallization across the *HP-GS* transition.

Deformation has been frequently invoked to explain such patterns in the Cyclades (e.g., Lister and Forster, 2016), mainly on account of the presumably high-*T* Ar closure of phengites permitting the preservation of crystallization (hence deformation) ages in *HP/LT* settings. The lack of textural control on *in situ* $^{40}Ar/^{39}Ar$ ages demonstrated in this and previous (Laurent et al., 2017) work indicates that the situation is considerably more complex than a well-resolved sequence of texturally preserved crystallization ages. The picture is rather one of overlapping (mixed) ages cryptically preserved at the sub-crystal (lattice) scale. Physically, the interplay between partial resetting/retention and (re)crystallization can be understood in the realm of the Dodsonian formalism via the effect of grain-size reduction in progressively deformed and exhumed systems (Goodwin and Renne, 1991) and the lowered kinetic thresholds for (re)crystallization and compositional-structural recombination promoted by deformation

(Dunlap, 1997; Mulch and Cosca, 2004). Coupled with the enhanced retention properties of white mica at *HP*, such grain-scale processes easily explain why younger ages, out-of-sequence, or breaks in $^{40}Ar/^{39}Ar$ regional trends occur locally next (and within) shear zones in which smaller, recrystallized and/or partly reset grains dominate (see also discussion on $^{40}Ar/^{39}Ar$ mixing sytematics by Sanchez et al., 2011, and Kula and Spell, 2012). Emblematic of such a situation is sample SY-14-73 (northern Lia Shear Zone) dominated by a pristine (syn-blueschist facies) fabric but in which 50 % of *in situ* apparent ages are younger than 37 Ma (to as young as 25 Ma, Fig. 12). This is much younger than the allowed residence time of the UCB at *HP* conditions inferred above (ending probably near 37 Ma, see Section 6.2 and below). Our interpretation is that grain-scale ^{40}Ar disequilibrium is preserved in this sample as a mosaic of *HP* and newly/partially (re)crystallized domains, each having a specific physical size, domain-structure, and $^{40}Ar^*$ inventory reflecting micro-scale gradients in chemical potentials, fluid availability, partial diffusional resetting, and extent of chemical/structural recombination.

As a rule, mixed ages from microstructural domains remain largely unresolved by the UV laser probe (50 µm spatial resolution). Perhaps the only exception in this study are the youngest *in situ* $^{40}Ar/^{39}Ar$ ages (37-35 Ma) measured on SY-14-64 (Fig. 10). The lack of compositional control on *in situ* ages noted there (see Section 6.1.3) shows that $^{40}Ar/^{39}Ar$ relationships to ongoing recrystallization processes cannot be simply inferred based on compositional grounds. But, at the same time, the 35-37 Ma ages actually happen to occur in a dilatant site formed at the interface of the garnet due to expansion of the matrix flowing away from it. Such a mechanism apparently allowed late crystal growth of *HP* phengites younger than the matrix specimens displaying ages between 42-46 Ma (above the garnet) and 40-44 Ma (along the flat lying matrix extending laterally away from the pressure shadow).

Aside from this case, our data show that the significance of intermediate, mixed, $^{40}Ar/^{39}Ar$ ages on Syros and Sifnos cannot be easily extracted from micro-scale $^{40}Ar/^{39}Ar$

relationships, and let alone from complex $^{40}Ar/^{39}Ar$ spectra lacking direct relevance to textural habitus (e.g., Lister and Forster, 2016). Our results conclusively show that (1) phengite domainal-scale behaviour occurs below the spatial resolution of the UV probe (50 µm), and (2), single-grain step-heating data are clearly affected by such sub-grain effects as well. The parallel with the phengite Rb/Sr record is striking both in terms of age and spread (Ring et al., 2011; Bröcker et al., 2013; Cliff et al., 2016), suggesting much in common in terms of retention behaviour and isotope-crystal disequilibrium kinetics. At the same time, our study conclusively shows that bulk $^{40}Ar/^{39}Ar$ patterns and large-scale variations may be used for tracking bulk temporal trends that reflect the time-averaged effect of deformation and associated Ar thermal-kinetic interaction operating across a major metamorphic transition. One major outcome of this study is that the imbrication of such widely varying spatial scales can be understood only through the combined application of large-scale sampling with *in situ* dating.

6.5. Regional implications

From a regional perspective, this study has implications both on the overall geometry of the *HP-LT* nappe stack and its geodynamic evolution. The lack of preservation of *HP* relicts in the Vari Unit and the stark age contrast between this (with pre-metamorphic ages largely in excess of 55 Ma, Fig. 8) and the underlying UCB (Kampos) unit argue in favour of the Vari fault being a detachment bringing shallower (cooler) rocks on top of exhumed *HP* slices as proposed previously (Trotet et al., 2001a; Soukis and Stöckli, 2013; Laurent et al., 2016), but disputed by some (Philippon et al., 2011). The older ages in the *HP*-free Vari Unit confirm earlier findings by Maluski et al. (1987) and indicate that it was exhumed much earlier than the UCB. Syn-*HP* crystallization $^{40}Ar/^{39}Ar$ ages measured between 50 and 37 Ma (Figs. 8, 9, 10) below the detachment are consistent with $^{40}Ar/^{39}Ar$ ages obtained elsewhere on *HP* rocks of the

Cycladic Islands such as Tinos and Andros (Bröcker et al., 1993; Huet et al., 2015; Laurent et al., 2017, Fig. 2). If, as discussed in section 6.2, these are indeed crystallization ages, this range constrains the timelife (in the ductile regime) of the Vari Detachment to at least this interval.

The Vari detachment accommodated the first steps of ductile exhumation from peak metamorphism to *BS*-facies conditions (Trotet et al., 2001; Jolivet et al., 2010; Huet et al., 2015; Laurent et al., 2016), and was later reactivated as a more localized brittle structure (Ring et al., 2003; Soukis and Stöckli, 2013). On Syros, the coupled $^{40}Ar/^{39}Ar$ downward overprinting progression shows that deformation localized toward the base (the lowermost Posidonia Subunit) in the UCB stack until crossing the ductile-brittle transition at 20-18 Ma. This stage corresponds to a major reconfiguration at the scale of the entire CBU with strain migration and localization on major post-orogenic detachments (NCDS, WCDS, and PNDS; Fig. 1; Jolivet et al., 2010; Grasemann et al., 2012). Such a temporal progression reflects major thermo-rheological changes driving the exhumation dynamics of the UCB stack. It remains for further work to investigate how similarly aged *GS*-facies rocks across the CBU (e.g., on Sifnos, Tinos, Andros, Kea, Kithnos; Altherr et al., 1982; Wijbrans et al., 1990; Bröcker & Franz, 1998, 2006; Iglseder et al., 2011; Ring et al., 2011; Grasemann et al., 2012; Bröcker et al., 2013; Cossette et al., 2015) relate to the last increments of ductile exhumation across the ductile-brittle transition along the main NCDS and WCDS detachment systems (Fig. 1).

7. Conclusions and outlook

Our detailed $^{40}Ar/^{39}Ar$, geochemical and structural analysis of the UCB exposed across Syros and Sifnos allows the following conclusions to be reached.

(1) Early peak-metamorphic phengite $^{40}Ar/^{39}Ar$ crystallization ages of ca. 51-48 Ma are preserved in pristine eclogites and blueschists formed at *P* ca. 22 kbar and 550 ± 50 °C

with grain-scale homogeneous ^{40}Ar patterns consistent with independent Sm/Nd garnet ages around 53-50 Ma, and inter-grain age differences locally reflecting protracted or piecewise phengite growth under sluggish ^{40}Ar diffusional kinetics at *T* in excess of 500 °C.

(2) During decompression and incipient overprinting at lower *P*, strong grain-scale $^{40}Ar/^{39}Ar$ age variations were produced as a result of domain-like Ar behaviour; this is manifested in the form of partially reset to fully preserved relicts of early *HP* clasts (or dislocated sub-grain domains) coexisting with neo-crystallized domains formed during metamorphic re-equilibration and *BS*- then *GS*-grade pervasive deformation. Such ^{40}Ar domains cannot be matched with clear-cut compositional or micro-textural domains at the scale resolved with the $^{40}Ar/^{39}Ar$ UV laser probe (ca. 50 µm). Structural and thermal-kinetic crystallographic processes driving ^{40}Ar and stoichiometric recombinations are coupled at a much more elementary level than currently accessible via the UV microprobe (i.e. possibly down the K-interlayer scale and lattice-scale nano-domains).

(3) A regional younging of bulk $^{40}Ar/^{39}Ar$ ages is documented across a regionally consistent (but locally irregular) eclogite/*BS* to *GS* grade transition culminating in fully reset (± newly crystallized) 20-18 Ma old phengites at the very base of the pile. We interpret this pattern as the progressive migration and localization of extensional deformation during exhumation through the *GS* facies. A major switch from syn-*HP* closed-system behaviour to thermal-kinetic resetting/opening occurred as the result of the progressive establishment of *GS* grade conditions around 37 Ma. Grain-scale $^{40}Ar^*$ inheritance from the *HP* stage and the switch to domain-like diffusional Ar exchange across the transition precludes resolving discrete deformation events associated to local/regional shear zones. However, the overall younging progression allows to temporally track the bulk migration of deformation through the nappe stack.

(4) A notable feature of our $^{40}Ar/^{39}Ar$ findings is the isotopic resilience of *HP* phengites preserving well-defined ages down to 37 Ma in pristine *BS* mineralogies (most notably our sample SY-16-15, Fig. 9); these ages reflect the ultimate stages of residence in the *HP/LT* subduction channel prior to mechanical destabilization and exhumation of the orogenic wedge. These ages are consistent with sedimentological and radiometric evidence indicating that the main stacking events lasted until the Eocene (Godfriaux and Mercier, 1965; Dubois and Bignot, 1979; Schermer, 1990, 1993; Godfriaux and Ricou, 1991; Shaked et al., 2000; Cliff et al., 2016).

(5) A major outcome of this study is that it is clearly not possible to properly interpret $^{40}Ar/^{39}Ar$ phengite ages from *HP/LT* settings without integrating the information at all scales, from the crystal proper (and below) to the regional relationships linking nappe-scale structures to time-varying thermo-kinematics. On Syros and Sifnos, the interplay between thermal-induced volume diffusion and strain localization is temporally and spatially related to the exhumation dynamics at the scale of the UCB, but these appear locally decoupled at the microscale. Such a complex behaviour is likely to be prevalent in other *HP/LT* successions exhumed elsewhere. Extensive combination of step-heating with high-resolution *in situ* dating is shown to be essential to better understand the processes governing Ar-mineral-deformation interactions at the crystal scale in such settings.

Acknowledgements

This work was funded by the European Research Council (ERC) under the seventh Framework Programme of the European Union (ERC Advanced Grant, grant agreement No 290864, RHEOLITH) and from the Institut Universitaire de France. The $^{40}Ar/^{39}Ar$ facility at ISTO is supported by the LABEX project VOLTAIRE (ANR-10- LABX-100-01), the Région Centre project ARGON, and the project EQUIPEX PLANEX (ANR-11-EQPX-0036). Careful and instructive reviews by Jan Wijbrans and an anonymous reviewer helped to considerably improve a two-round submission of the manuscript.

Research data

Research Data associated with this article can be accessed at http://dx.doi.org/10.17632/5kgjjhmcgg.1

References

Altherr, R., Kreuzer, H. A. N. S., Wendt, I., Lenz, H., Wagner, G. A., 1982. A late Oligocene/early Miocene high temperature belt in the Attic-Cycladic crystalline complex (SE Pelagonian, Greece). Geologisches Jahrbuch. Reihe E, Geophysik 23, 97-164.

Ashley, K.T., Caddick, M.J., Steele-MacInnis, M.J., Bodnar, R.J., Dragovic, B. (2014). Geothermobarometric history of subduction recorded by quartz inclusions in garnet. *Geochemistry, Geophysics, Geosystems*, 15, 350–360.

Augier, R., Jolivet, L., Gadenne, L., Lahfid, A., Driussi, O., 2015. Exhumation kinematics of the Cycladic Blueschists unit and back-arc extension, insight from the Southern Cyclades (Sikinos and Folegandros Islands, Greece), Tectonics, 34, 152-185, doi: 10.1002/2014TC003664.

983 Avigad, D., Garfunkel, Z., 1991. Uplift and exhumation of high-pressure metamorphic terrains:
984 the example of the Cycladic blueschist belt (Aegean Sea). Tectonophysics 188, 357–
985 372.
986 Baldwin, S.L., Lister, G.S., 1998. Thermochronology of the South Cyclades Shear Zone, Ios,
987 Greece: Effects of ductile shear in the argon partial retention zone. Journal of
988 Geophysical Research: Solid Earth 103, 7315–7336.
989 Baziotis, I., Proyer, A., Mposkos, E., 2009. High-pressure/low-temperature metamorphism of
990 basalts in Lavrion (Greece): implications for the preservation of peak metamorphic
991 assemblages in blueschists and greenschists. European Journal of Mineralogy 21, 133-
992 148.
993 Beaudoin, A., Augier, R., Laurent, V., Jolivet, L., Lahfid, A., Bosse, V., Arbaret, L., Rabillard,
994 A., Menant, A., 2015. The Ikaria high-temperature Metamorphic Core Complex
995 (Cyclades, Greece): Geometry, kinematics and thermal structure. Journal of
996 Geodynamics 92, 18–41. doi:10.1016/j.jog.2015.09.004.
997 Beltrando, M., Di Vincenzo, G., Ferraris, C., 2013. Preservation of sub-microscopic structural
998 relicts in micas from the Gran Paradiso Massif (Western Alps): Implications for
999 $^{40}Ar/^{39}Ar$ geochronology. Geochimica et Cosmochimica Acta 119, 359–380.
1000 Bonneau, M. (1984). Correlation of the Hellenide nappes in the south-east Aegean and their
1001 tectonic reconstruction. *Geological Society, London, Special Publications*, 17, 517–527.
1002 Bonneau, M., Kienast, J.R., 1982. Subduction, collision et schistes bleus; l'exemple de l'Egée
1003 (Grece). Bulletin de la société Géologique de France 785–791.
1004 Bröcker, M., Baldwin, S., Arkudas, R., 2013. The geological significance of $^{40}Ar/^{39}Ar$ and Rb–
1005 Sr white mica ages from Syros and Sifnos, Greece: a record of continuous (re)
1006 crystallization during exhumation? Journal of Metamorphic Geology 31, 629–646.
1007 Bröcker, M., Bieling, D., Hacker, B., Gans, P., 2004. High-Si phengite records the time of

greenschist facies overprinting: implications for models suggesting mega-detachments in the Aegean Sea. Journal of Metamorphic Geology 22, 427–442.

Bröcker, M., Franz, L., 1998. Rb–Sr isotope studies on Tinos Island (Cyclades, Greece): additional time constraints for metamorphism, extent of infiltration-controlled overprinting and deformational activity. Geological Magazine 135, 369–382.

Bröcker, M., Franz, L., 2006. Dating metamorphism and tectonic juxtaposition on Andros Island (Cyclades, Greece): results of a Rb–Sr study. Geological Magazine 143, 609–620.

Bröcker, M., Kreuzer, H., Matthews, A., Okrusch, M., 1993. $^{40}Ar/^{39}Ar$ and oxygen isotope studies of polymetamorphism from Tinos Island, Cycladic blueschist belt, Greece. Journal of Metamorphic Geology 11, 223–240.

Brooks, H. L., Dragovic, B., Lamadrid, H. M., Caddick, M. J., Bodnar, R. J., 2019. Fluid capture during exhumation of subducted lithologies: A fluid inclusion study from Sifnos, Greece. Lithos 332, 120–134.

Cliff, R. A., Bond, C. E., Butler, R. W. H., Dixon, J. E., 2017. Geochronological challenges posed by continuously developing tectonometamorphic systems: insights from Rb–Sr mica ages from the Cycladic Blueschist Belt, Syros (Greece). Journal of Metamorphic Geology 35, 197-211.

Cossette, É., Schneider, D.A., Warren, C.J., Grasemann, B., 2015. Lithological, rheological, and fluid infiltration control on $^{40}Ar/^{39}Ar$ ages in polydeformed rocks from the West Cycladic detachment system, Greece. Lithosphere 7, 189–205.

Dahl, P. S., 1996. The effects of composition on retentivity of argon and oxygen in hornblende and related amphiboles: A field-tested empirical model. Geochimica et Cosmochimica Acta 60, 3687-3700.

De Andrade, V., Vidal, O., Lewin, E., O'Brien, P., Agard, P., 2006. Quantification of electron

microprobe compositional maps of rock thin sections: an optimized method and examples. Journal of Metamorphic Geology 24, 655–668.

Di Vincenzo, G., Tonarini, S., Lombardo, B., Castelli, D., Ottolini, L., 2006. Comparison of $^{40}Ar/^{39}Ar$ and Rb–Sr data on phengites from the UHP Brossasco–Isasca Unit (Dora Maira Massif, Italy): implications for dating white mica. Journal of Petrology 47, 1439–1465.

Dixon, J. E., Feenstra, A., Jansen, J. B. H., Kreulen, R., Ridley, J., Salemink, J., Schuiling, R. D., 1987. Excursion guide to the field trip on Seriphos, Syros, and Naxos. Chemical Transport in Metasomatic Processes, 467–518.

Dragovic, B., Baxter, E.F., Caddick, M.J., 2015. Pulsed dehydration and garnet growth during subduction revealed by zoned garnet geochronology and thermodynamic modeling, Sifnos, Greece. Earth and Planetary Science Letters 413, 111–122.

Dragovic, B., Samanta, L.M., Baxter, E.F., Selverstone, J., 2012. Using garnet to constrain the duration and rate of water-releasing metamorphic reactions during subduction: An example from Sifnos, Greece. Chemical Geology 314, 9–22.

Dubois, R., Bignot, G., 1979. Presence d'un 'hard-ground' nummulitique au de la serie crétacée d'Almyropotamos (Eubee meridionale, Grece). CR Seances Acad. Sci., Ser. D 289, 993-995.

Dunlap, W. J.,1997. Neocrystallization or cooling? $^{40}Ar/^{39}Ar$ ages of white micas from low-grade mylonites. Chemical Geology 143, 181-203.

Fornash, K. F., Cosca, M. A., Whitney, D. L., 2016. Tracking the timing of subduction and exhumation using $^{40}Ar/^{39}Ar$ phengite ages in blueschist-and eclogite-facies rocks (Sivrihisar, Turkey). Contributions to Mineralogy and Petrology 171, 67.

Gautier, P., Brun, J.-P., Jolivet, L., 1993. Structure and kinematics of upper Cenozoic extensional detachment on Naxos and Paros (Cyclades Islands, Greece). Tectonics 12,

1180–1194.

Gautier, P., Brun, J.P., 1994. Ductile crust exhumation and extensional detachments in the central Aegean (Cyclades and Evvia Islands). Geodinamica Acta 7, 57–85.

Giorgis, D., Cosca, M., Li, S., 2000. Distribution and significance of extraneous argon in UHP eclogite (Sulu terrain, China): insight from in situ $^{40}Ar/^{39}Ar$ UV-laser ablation analysis. Earth and Planetary Science Letters 181, 605–615.

Godfriaux, I., Mercier, J., 1965. Essai de comparaison des massifs métamorphiques de Thessalie et de Macédoine. Annls Soc. géol. N. 84, 205-221.

Godfriaux, I., Ricou, L. E., 1991. Le Paikon, une fenêtre tectonique dans les Hellénides internes (Macédoine, Grèce). Comptes rendus de l'Académie des sciences. Série 2, Mécanique, Physique, Chimie, Sciences de l'univers, Sciences de la Terre 313, 1479-1484.

Goodwin, L. B., Renne, P. R., 1991. Effects of progressive mylonitization on Ar retention in biotites from the Santa Rosa mylonite zone, California, and thermochronologic implications. Contributions to Mineralogy and Petrology 108, 283-297.

Grasemann, B., Huet, B., Schneider, D. A., Rice, A. H. N., Lemonnier, N., Tschegg, C., 2018. Miocene postorogenic extension of the Eocene synorogenic imbricated Hellenic subduction channel: New constraints from Milos (Cyclades, Greece). GSA Bulletin 130, 238-262.

Grasemann, B., Schneider, D.A., Stöckli, D.F., Iglseder, C., 2012. Miocene bivergent crustal extension in the Aegean: Evidence from the western Cyclades (Greece). Lithosphere L164–1.

Groppo, C., Forster, M., Lister, G., Compagnoni, R., 2009. Glaucophane schists and associated rocks from Sifnos (Cyclades, Greece): New constraints on the P–T evolution from oxidized systems. Lithos 109, 254–273.

Halama, R., Konrad-Schmolke, M., Sudo, M., Marschall, H.R., Wiedenbeck, M., 2014. Effects

of fluid–rock interaction on $^{40}Ar/^{39}Ar$ geochronology in high-pressure rocks (Sesia-Lanzo Zone, Western Alps). Geochimica et Cosmochimica Acta 126, 475–494.

Harrison, T.M., Célérier, J., Aikman, A.B., Hermann, J., Heizler, M.T., 2009. Diffusion of ^{40}Ar in muscovite. Geochimica et Cosmochimica Acta 73, 1039–1051.

Hausmann, H., 1845. Beiträge zur Oryktographie von Syra. Advanced Synthesis & Catalysis 34, 238–241.

Huet, B., Labrousse, L., Jolivet, L., 2009. Thrust or detachment? Exhumation processes in the Aegean: insight from a field study on Ios (Cyclades, Greece). Tectonics 28.

Huet, B., Labrousse, L., Monié, P., Malvoisin, B., Jolivet, L., 2015. Coupled phengite $^{40}Ar/^{39}Ar$ geochronology and thermobarometry: PTt evolution of Andros Island (Cyclades, Greece). Geological Magazine 152, 711–727.

Iglseder, C., Grasemann, B., Rice, A.H.N., Petrakakis, K., Schneider, D.A., 2011. Miocene south directed low-angle normal fault evolution on Kea Island (West Cycladic Detachment System, Greece). Tectonics 30.

Jolivet, L., Brun, J.-P., 2010. Cenozoic geodynamic evolution of the Aegean. International Journal of Earth Sciences 99, 109–138.

Jolivet, L., Daniel, J.M., Truffert, C., Goffé, B., 1994. Exhumation of deep crustal metamorphic rocks and crustal extension in arc and back-arc regions. Lithos 33, 3–30.

Jolivet, L., Faccenna, C., Goffé, B., Burov, E., Agard, P., 2003. Subduction tectonics and exhumation of high-pressure metamorphic rocks in the Mediterranean orogens. American Journal of Science 303, 353–409.

Jolivet, L., Faccenna, C., Huet, B., Labrousse, L., Le Pourhiet, L., Lacombe, O., Lecomte, E., Burov, E., Denèle, Y., Brun, J.-P., others, 2013. Aegean tectonics: Strain localisation, slab tearing and trench retreat. Tectonophysics 597, 1–33.

Jolivet, L., Lecomte, E., Huet, B., Denèle, Y., Lacombe, O., Labrousse, L., Le Pourhiet, L.,

1108 Mehl, C., 2010. The north cycladic detachment system. Earth and Planetary Science
1109 Letters 289, 87–104.
1110 Jolivet, L., Menant, A., Sternai, P., Rabillard, A., Arbaret, L., Augier, R., Laurent, V.,
1111 Beaudoin, A., Grasemann, B., Huet, B., others, 2015. The geological signature of a slab
1112 tear below the Aegean. Tectonophysics. doi:10.1016/j.tecto.2015.08.004
1113 Jolivet, L., Patriat, M., 1999. Ductile extension and the formation of the Aegean Sea. Geological
1114 Society, London, Special Publications 156, 427–456.
1115 Jolivet, L., Rimmelé, G., Oberhänsli, R., Goffé, B., Candan, O., 2004. Correlation of syn-
1116 orogenic tectonic and metamorphic events in the Cyclades, the Lycian nappes and the
1117 Menderes massif. Geodynamic implications. Bulletin de la Société Géologique de
1118 France 175, 217–238.
1119 Katagas, C. G., 1984. High pressure metamorphism in Ghiaros island, Cyclades, Greece.
1120 Geological Society, London, Special Publications 17, 537–544.
1121 Katzir, Y., Avigad, D., Matthews, A., Garfunkel, Z., Evans, B. W., 2000. Origin, HP/LT
1122 metamorphism and cooling of ophiolitic mélanges in southern Evia (NW Cyclades),
1123 Greece. Journal of Metamorphic Geology 18, 699–718.
1124 Keay, S., Lister, G., Buick, I., 2001. The timing of partial melting, Barrovian metamorphism
1125 and granite intrusion in the Naxos metamorphic core complex, Cyclades, Aegean Sea,
1126 Greece. Tectonophysics 342, 275–312.
1127 Keiter, M., Ballhaus, C., Tomaschek, F., 2011. A new geological map of the Island of Syros
1128 (Aegean Sea, Greece): Implications for lithostratigraphy and structural history of the
1129 Cycladic Blueschist Unit. Geological Society of America Special Papers 481, 1–43.
1130 Kula, J., Spell, T. L., 2012. Recovery of muscovite age gradients by $^{40}Ar/^{39}Ar$ vacuum furnace
1131 step-heating analysis. Chemical Geology 304, 166-174.
1132 Lagos, M., Scherer, E.E., Tomaschek, F., Münker, C., Keiter, M., Berndt, J., Ballhaus, C., 2007.

1133 High precision Lu–Hf geochronology of Eocene eclogite-facies rocks from Syros,
1134 Cyclades, Greece. Chemical Geology 243, 16–35.
1135 Lanari, P., Vidal, O., De Andrade, V., Dubacq, B., Lewin, E., Grosch, E.G., Schwartz, S., 2014.
1136 XMapTools: A MATLAB\copyright-based program for electron microprobe X-ray
1137 image processing and geothermobarometry. Computers & Geosciences 62, 227–240.
1138 Laurent, V., Beaudoin, A., Jolivet, L., Arbaret, L., Augier, R., Rabillard, A., Menant, A., 2015.
1139 Interrelations between extensional shear zones and synkinematic intrusions: The
1140 example of Ikaria Island (NE Cyclades, Greece). Tectonophysics 651, 152–171.
1141 doi:10.1016/j.tecto.2015.03.020
1142 Laurent, V., Huet, B., Labrousse, L., Jolivet, L., Monie, P., Augier, R., 2017. Extraneous argon
1143 in high-pressure metamorphic rocks: Distribution, origin and transport in the Cycladic
1144 Blueschist Unit (Greece). Lithos.
1145 Laurent, V., Jolivet, L., Roche, V., Augier, R., Scaillet, S., Cardello, G.L., 2016. Strain
1146 localization in a fossilized subduction channel: Insights from the Cycladic Blueschist
1147 Unit (Syros, Greece). Tectonophysics 672, 150–169. doi:10.1016/j.tecto.2016.01.036.
1148 Laurent, V., Lanari, P., Naïr, I., Augier, R., Lahfid, A., Jolivet, L., 2018. Exhumation of eclogite
1149 and blueschist (Cyclades, Greece): Pressure–temperature evolution determined by
1150 thermobarometry and garnet equilibrium modelling. Journal of metamorphic geology
1151 36, 769–798. DOI: 10.1111/jmg.12309.
1152 Le Pichon, X., Angelier, J., 1981. The Aegean Sea. Royal Society of London Philosophical
1153 Transactions Series A 300, 357–372.
1154 Lister, G.S., Baldwin, S.L., 1996. Modelling the effect of arbitrary PTt histories on argon
1155 diffusion in minerals using the MacArgon program for the Apple Macintosh.
1156 Tectonophysics 253, 83–109.
1157 Lister, G., Forster, M., 2016. White mica $^{40}Ar/^{39}Ar$ age spectra and the timing of multiple

episodes of high-pressure metamorphic mineral growth in the Cycladic eclogite-blueschist belt, Syros, Aegean Sea, Greece. Journal of Metamorphic Geology.

Lister, G.S., Banga, G., Feenstra, A., 1984. Metamorphic core complexes of Cordilleran type in the Cyclades, Aegean Sea, Greece. Geology 12, 221–225.

Maluski, H., Bonneau, M., Kienast, J.R., 1987. Dating the metamorphic events in the Cycladic area; $^{40}Ar/^{39}Ar$ data from metamorphic rocks of the Island of Syros (Greece). Bulletin de la Société géologique de France 3, 833–842.

McDonald, C. S., Warren, C. J., Mark, D. F., Halton, A. M., Kelley, S. P., Sherlock, S. C., 2016. Argon redistribution during a metamorphic cycle: Consequences for determining cooling rates. Chemical Geology 443, 182-197.

Monie, P., Chopin, C., 1991. $^{40}Ar/^{39}Ar$ dating in coesite-bearing and associated units of the Dora Maira massif, Western Alps. European Journal of Mineralogy, 239-262.

Mulch, A., Cosca, M. A., 2004. Recrystallization or cooling ages: in situ UV-laser $^{40}Ar/^{39}Ar$ geochronology of muscovite in mylonitic rocks. Journal of the Geological Society 161, 573-582.

Okay, A. I. (1989). Alpine-Himalayan blueschists. Annual Review of Earth and Planetary Sciences, 17(1), 55-87.

Parra, T., Vidal, O., Jolivet, L., 2002. Relation between the intensity of deformation and retrogression in blueschist metapelites of Tinos Island (Greece) evidenced by chlorite–mica local equilibria. Lithos 63, 41–66.

Philippon, M., Brun, J.-P., Gueydan, F., 2011. Tectonics of the Syros blueschists (Cyclades, Greece): From subduction to Aegean extension. Tectonics 30.

Putlitz, B., Cosca, M.A., Schumacher, J.C., 2005. Prograde mica $^{40}Ar/^{39}Ar$ growth ages recorded in high pressure rocks (Syros, Cyclades, Greece). Chemical Geology 214, 79–98.

Rabillard, A., Jolivet, L., Arbaret, L., Bessière, E., Laurent, V., Menant, A., Augier, R., Beaudoin, A., 2018. Synextensional Granitoids and Detachment Systems Within Cycladic Metamorphic Core Complexes (Aegean Sea, Greece): Toward a Regional Tectonomagmatic Model. Tectonics 37, 2328–2362.

Reddy, S. M., Kelley, S. P., Wheeler, J., 1996. A $^{40}Ar/^{39}Ar$ laser probe study of micas from the Sesia Zone, Italian Alps: implications for metamorphic and deformation histories. Journal of Metamorphic Geology 14, 493-508.

Renne, P.R., Swisher, C.C., Deino, A.L., Karner, D.B., Owens, T.L., DePaolo, D.J., 1998. Intercalibration of standards, absolute ages and uncertainties in $^{40}Ar/^{39}Ar$ dating. Chemical Geology 145, 117–152.

Ridley, J., 1982. Arcuate lineation trends in a deep level, ductile thrust belt, Syros, Greece. Tectonophysics 88, 347–360.

Ring, U., Glodny, J., Will, T., Thomson, S., 2010. The Hellenic subduction system: high-pressure metamorphism, exhumation, normal faulting, and large-scale extension. Annual Review of Earth and Planetary Sciences 38, 45–76.

Ring, U., Glodny, J., Will, T., Thomson, S., 2011. Normal faulting on Sifnos and the South Cycladic Detachment System, Aegean Sea, Greece. Journal of the Geological Society 168, 751–768.

Ring, U., Thomson, S.N., Bröcker, M., 2003. Fast extension but little exhumation: the Vari detachment in the Cyclades, Greece. Geological Magazine 140, 245–252.

Roche, V., Conand, C., Jolivet, L., Augier, R., 2018. Tectonic evolution of Leros Island (Dodecanese, Greece) and correlations between the Aegean Domain and the Menderes Massif. Journal of the Geological Society jgs2018-028.

Roche, V., Jolivet, L., Papanikolaou, D., Bozkurt, E., Menant, A., & Rimmelé, G., 2019. Slab fragmentation beneath the Aegean/Anatolia transition zone: Insights from the tectonic

and metamorphic evolution of the Eastern Aegean region. Tectonophysics 754, 101-129.

Roche, V., Laurent, V., Cardello, G.L., Jolivet, L., Scaillet, S., 2016. Anatomy of the Cycladic Blueschist Unit on Sifnos Island (Cyclades, Greece). Journal of Geodynamics 97, 62–87. doi:10.1016/j.jog.2016.03.008.

Rogowitz, A., Grasemann, B., Huet, B., Habler, G., 2014. Strain rate dependent calcite microfabric evolution–An experiment carried out by nature. Journal of Structural Geology 69, 1–17.

Rogowitz, A., Huet, B., Schneider, D., Grasemann, B., 2015. Influence of high strain rate deformation on $^{40}Ar/^{39}Ar$ mica ages from marble mylonites (Syros, Greece). Lithosphere 7, 535–540.

Rogowitz, A., White, J.C., Grasemann, B., 2016. Strain localization in ultramylonitic marbles by simultaneous activation of dislocation motion and grain boundary sliding (Syros, Greece). Solid Earth 7, 355.

Sanchez, G., Rolland, Y., Schneider, J., Corsini, M., Oliot, E., Goncalves, P., Verati, C., Lardeaux, J-M,. Marquer, D., 2011. Dating low-temperature deformation by $^{40}Ar/^{39}Ar$ on white mica, insights from the Argentera-Mercantour Massif (SW Alps). Lithos 125, 521-536.

Scaillet, S., 1996. Excess ^{40}Ar transport scale and mechanism in high-pressure phengites: A case study from an eclogitized metabasite of the Dora-Maira nappe, western Alps. Geochimica et Cosmochimica Acta 60, 1075–1090.

Scaillet, S., 1998. K-Ar ($^{40}Ar/^{39}Ar$) geochronology of ultrahigh pressure rocks, in: When Continents Collide: Geodynamics and Geochemistry of Ultrahigh-Pressure Rocks. Springer, pp. 161–201.

Scaillet, S., 2000. Numerical error analysis in $^{40}Ar/^{39}Ar$ dating. Chemical Geology 162, 269-

298.

Scaillet, S., Feraud, G., Ballevre, M., Amouric, M., 1992. Mg/Fe and [(Mg,Fe)Si-Al_2] compositional control on argon behaviour in high-pressure white micas: A $^{40}Ar/^{39}Ar$ continuous laser-probe study from the Dora-Maira nappe of the internal western Alps, Italy. Geochimica et Cosmochimica Acta 56, 2851-2872.

Scheffer, C., Vanderhaeghe, O., Lanari, P., Tarantola, A., Ponthus, L., Photiades, A., France, L., 2016. Syn-to post-orogenic exhumation of metamorphic nappes: Structure and thermobarometry of the western Attic-Cycladic metamorphic complex (Lavrion, Greece). Journal of Geodynamics 96, 174–193.

Schermer, E. R., 1990. Mechanisms of blueschist creation and preservation in an A-type subduction zone, Mount Olympos region, Greece. Geology 18, 1130-1133.

Schermer, E. R., 1993. Geometry and kinematics of continental basement deformation during the Alpine orogeny, Mt. Olympos region, Greece. Journal of Structural Geology 15, 571-591.

Schertl, H. P., Hammerschmidt, K., 2016. Tracking the incidence of excess argon in white mica Ar–Ar data from UHP conditions to upper crustal levels in the Dora-Maira Massif, Western Alps. European Journal of Mineralogy 28, 1255–1275.

Schliestedt, M., Matthews, A., 1987. Transformation of blueschist to greenschist facies rocks as a consequence of fluid infiltration, Sifnos (Cyclades), Greece. Contributions to Mineralogy and Petrology 97, 237–250.

Schneider, D. A., Grasemann, B., Lion, A., Soukis, K., Draganits, E., 2018. Geodynamic significance of the Santorini Detachment System (Cyclades, Greece). Terra Nova 30, 414–422.

Schneider, D.A., Senkowski, C., Vogel, H., Grasemann, B., Iglseder, C., Schmitt, A.K., 2011. Eocene tectonometamorphism on Serifos (western Cyclades) deduced from zircon

depth-profiling geochronology and mica thermochronology. Lithos 125, 151–172.

Shaked, Y., Avigad, D., Garfunkel, Z., 2000. Alpine high-pressure metamorphism at the Almyropotamos window (southern Evia, Greece). Geological Magazine 137, 367-380.

Skelton, A., Peillod, A., Glodny, J., Klonowska, I., Månbro, C., Lodin, K., Ring, U., 2019. Preservation of high‐P rocks coupled to rock composition and the absence of metamorphic fluids. Journal of Metamorphic Geology 37, 359–381. https://doi.org/10.1111/jmg.12466.

Sletten, V. W., Onstott, A. T., 1998. The effect of the instability of muscovite during in vacuo heating on $^{40}Ar/^{39}Ar$ step-heating spectra. Geochimica et Cosmochimica Acta 62, 123-141.

Smye, A.J., Warren, C.J., Bickle, M.J., 2013. The signature of devolatisation: Extraneous ^{40}Ar systematics in high-pressure metamorphic rocks. Geochimica et Cosmochimica Acta 113, 94–112.

Soukis, K., Stockli, D.F., 2013. Structural and thermochronometric evidence for multi-stage exhumation of southern Syros, Cycladic islands, Greece. Tectonophysics 595, 148–164.

Tomaschek, F., Kennedy, A.K., Villa, I.M., Lagos, M., Ballhaus, C., 2003. Zircons from Syros, Cyclades, Greece—recrystallization and mobilization of zircon during high-pressure metamorphism. Journal of Petrology 44, 1977–2002.

Trotet, F., Jolivet, L., Vidal, O., 2001a. Tectono-metamorphic evolution of Syros and Sifnos islands (Cyclades, Greece). Tectonophysics 338, 179–206.

Trotet, F., Vidal, O., Jolivet, L., 2001b. Exhumation of Syros and Sifnos metamorphic rocks (Cyclades, Greece). New constraints on the PT paths. European Journal of Mineralogy 13, 901–902.

Urai, J.L., Schuiling, R.D., Jansen, J.B.H., 1990. Alpine deformation on Naxos (Greece). Geological Society, London, Special Publications 54, 509–522.

1283 Uunk, B., Brouwer, F., ter Voorde, M., Wijbrans, J., 2018. Understanding phengite argon
1284 closure using single grain fusion age distributions in the Cycladic Blueschist Unit on
1285 Syros, Greece. Earth and Planetary Science Letters 484, 192-203.
1286 Vanderhaeghe, O., 2004. Structural development of the Naxos migmatite dome. Geological
1287 Society of America Special Papers 380, 211–227.
1288 Warren, C. J., Hanke, F., Kelley, S. P., 2012a. When can muscovite $^{40}Ar/^{39}Ar$ dating constrain
1289 the timing of metamorphic exhumation? Chemical Geology 291, 79–86.
1290 Warren, C. J., Kelley, S. P., Sherlock, S. C., McDonald, C. S., 2012b. Metamorphic rocks seek
1291 meaningful cooling rate: Interpreting $^{40}Ar/^{39}Ar$ ages in an exhumed ultra-high pressure
1292 terrane. Lithos 155, 30-48.
1293 Warren, C. J., Sherlock, S. C., Kelley, S. P., 2011. Interpreting high-pressure phengite $^{40}Ar/^{39}Ar$
1294 laserprobe ages: an example from Saih Hatat, NE Oman. Contributions to Mineralogy
1295 and Petrology 161, 991-1009.
1296 Whitney, D.L., Evans, B.W., 2010. Abbreviations for names of rock-forming minerals.
1297 American mineralogist 95, 185.
1298 Wijbrans, J.R., McDougall, I., 1986. $^{40}Ar/^{39}Ar$ dating of white micas from an Alpine high-
1299 pressure metamorphic belt on Naxos (Greece): the resetting of the argon isotopic
1300 system. Contributions to Mineralogy and Petrology 93, 187–194.
1301 Wijbrans, J.R., McDougall, I., 1988. Metamorphic evolution of the Attic Cycladic
1302 Metamorphic Belt on Naxos (Cyclades, Greece) utilizing $^{40}Ar/^{39}Ar$ age spectrum
1303 measurements. Journal of Metamorphic Geology 6, 571–594.
1304 Wijbrans, J.R., Schliestedt, M., York, D., 1990. Single grain argon laser probe dating of
1305 phengites from the blueschist to greenschist transition on Sifnos (Cyclades, Greece).
1306 Contributions to Mineralogy and Petrology 104, 582–593.
1307

Figure captions

Figure 1: Geological framework of the Aegean domain and the Cycladic archipelago. a) Tectonic map of the Aegean domain showing the distribution of metamorphic units and the age of magmatic intrusions highlighting southward slab retreat (Modified after Roche et al., 2019). b) Simplified geological map of the Cycladic archipelago, localizing Syros and Sifnos islands (after Jolivet et al., 2015). Major tectonic structures include the syn-orogenic Vari Detachment (VD) and the post-orogenic North Cycladic Detachment System (NCDS), the West Cycladic Detachment System (WCDS) and Naxos-Paros Detachment System (NPDS) with the local kinematics indicated. c) Cross-sections showing the current position of the plunging slab below Crete (after Jolivet and Brun, 2010), and the present-day structure of the Cyclades, characterized by metamorphic domes exhumed below detachment systems (after Augier et al., 2015). Abbreviations: AD (Alaşehir Detachment); BD (Büyük Menderes Detachment); CD (Crete Detachment); LCB (Lower Cycladic Blueschist Nappe); MMCC (Menderes Metamorphic Core Complex); NAF (North Anatolian Fault); SD (Simav Detachment); SDS (Santorini Detachment System); T-C.T (Trans-Cycladic Thrust); UCB (Upper Cycladic Blueschist Nappe).

Figure 2: Structural-metamorphic map of Syros with sample location. Sampling across the Chryssopighi Shear Zone on Sifnos is also shown as well as the location of cross-sections reported in Figure 3.

Figure 3: $^{40}Ar/^{39}Ar$ ages measured in this study across strain gradients in Syros and Sifnos islands. The cross-sections are modified after Laurent et al., 2016.

Figure 4: Compilation of previous geochronological data measured on Syros and Tinos and *P-T* path of the UCB (after Laurent et al., 2018). All detailed ages with their references are synthetized in Appendix S1 and S2. $^{40}Ar/^{39}Ar$ and Rb/Sr ages are represented by a curve defined by a normalized probability law (see Laurent et al., 2017 for more details). Maximum and minimum ages given by hump-shaped $^{40}Ar/^{39}Ar$ spectra are represented by orange rectangles connected by dashed lines.

Figure 5: Structural and geochemical setting of $^{40}Ar/^{39}Ar$ samples collected in the Posidonia Subunit. Samples are generally strongly deformed and pervasively overprinted in *GS*-facies (a), however some samples locally preserved *HP-LT* parageneses (e.g. SY-14-18) (b). Thin sections revealed the impact of lithology on the intensity of phengite deformation (b) and recrystallization (c). Phengites in samples containing calcite (e.g. SY-14-76) are less intensely deformed and recrystallized than in quartzitic samples (e.g. SY-14-80) as previously suggested by Cossette et al. (2015) and Rogowitz et al. (2015). Geochemical data (c) represented by squares correspond to EPMA spot analyses of phengite composition while the data represented by small blue circles are derived from the X-Ray compositional map. Mineral abbreviations are after Whitney and Evans (2010).

Figure 6: Structural and outcrop setting of $^{40}Ar/^{39}Ar$ samples collected in Chroussa Subunit. The 3-D sketch shows the outcrop relationships of SY-16-06 and SY-16-15 (a). SY-16-15 sample consists of phengite crystals collected from the neck of an eclogite boudins. While the outcrop shows a clear foliation (b) and some syn-blueschist facies shear deformation such as shear bands (a), phengite crystals of SY-16-06 show a low deformation (c). Microscope picture of SY-16-15 phengite grains shows relatively undeformed primary crystals (d).

Figure 7: Structural and geochemical setting of $^{40}Ar/^{39}Ar$ samples collected in Kampos and Vari Units. a) Outcrop characterization of samples from the Kampos Subunit. b) Thin-section microphotographs of phengite textural habitus showing moderately deformed crystals. c) Chemical composition of phengite in Si *vs.* X_{Mg} space. A clear partial recrystallization of phengites is observed in sample SY-14-40b$_4$. Phengite composition in samples from the Vari Unit is not significantly different to composition of phengite in the UCB. Geochemical data represented by squares correspond to EPMA spot analyses of phengite composition while the data represented by small blue circles are derived from the X-Ray compositional map.

Figure 8: Step-heating $^{40}Ar/^{39}Ar$ age spectra of phengite single grain and population from the southern Syros section. TGA: total gas age. Error boxes and TGA are ± 1σ. The colour of the age spectra refers to the grade of metamorphism of each sample (all shades of green: greenschist; all shades of blue: blueschist; all shades of red: eclogite; all shades of yellow: samples of the Vari Unit that shows no *HP* metamorphism). Note that the scale of the vertical axis is different for samples of the Vari Unit due to a significantly older range of apparent ages (37-145 Ma) compare to the UCB (18-45 Ma).

Figure 9: Range of *in situ* phengite apparent $^{40}Ar/^{39}Ar$ ages measured in sample SY-16-15 showing inter-grain age differences as high as 10 Ma while displaying homogeneous crystal-scale $^{40}Ar^*$ compositions. Note that the larger phengite grain (SY-16-15a) yields to younger *in situ* apparent ages than all the other smaller phengite grains. TGA: total gas age. Error boxes and TGA are ± 1σ.

Figure 10: Distribution of *in situ* apparent $^{40}Ar/^{39}Ar$ ages measured in phengites from sample SY-14-64 collected in the Kampos Subunit. a) Picture of the analysed rock-section showing the

1383 presence of garnets embedded in an omphacitic matrix. b) Results of *in situ* laser ablation
1384 analyses. c) Correlation between measured apparent $^{40}Ar/^{39}Ar$ ages and specific phengite
1385 compositions highlighted on the compositional map. d) *In situ* laser ablation results represented
1386 on BSE images. Squares (65 μm) and circles (50 μm) correspond to the geometry of the laser
1387 ablation and numbers inside refer to the corresponding analysis (see Appendix S5). TGA: total
1388 gas age. Error boxes and TGA are ± 1σ.
1389
1390
1391 Figure 11: Structural and geochemical setting of $^{40}Ar/^{39}Ar$ samples collected across the *BS*-
1392 facies Lia Shear Zone. a) Outcrop characterization of samples from the Lia Shear Zone
1393 including top-to the east syn-*BS*-facies deformation in sample SY-14-73. b) Thin-section
1394 microphotographs of phengite textural habitus showing a clear deformation gradient from SY-
1395 14-74 to SY-14-73. c) Chemical composition of phengite in Si *vs.* X_{Mg} space showing partial
1396 recrystallization in SY-14-73.
1397
1398 Figure 12: *in situ* $^{40}Ar/^{39}Ar$ laserprobe data from the Lia Shear Zone. a) SY-14-73 rock section
1399 analysed by the *in situ* UV-laser ablation technique and displaying a top-to-the E shear band
1400 associated with glaucophane. b) Results of *in situ* laser ablation analyses for all three rock-
1401 sections showing a clear trend toward younger apparent ages in the most deformed SY-14-73
1402 sample. c) BSE close-up showing *in situ* age distribution in SY-14-73. No clear correlation
1403 between microstructures and *in situ* $^{40}Ar/^{39}Ar$ ages can be seen. Squares (65 μm) and circles
1404 (50 μm) correspond to the diameter of the laser beam with numbers indicating the
1405 corresponding analysis (see Appendix S5). Ablation trenches are indicated by tie-lines
1406 connecting the endpoints of the rastered area. d) BSE close-up of SY-14-71 displaying
1407 homogenous ages around 48-50 Ma in and around phengite aggregate pseudomorph after

(presumably) lawsonite. e) Step-heating $^{40}Ar/^{39}Ar$ age spectra obtained on single phengite grains of samples SY-14-71 and SY-14-73. TGA: total gas age. Error boxes and TGA are ± 1σ.

Figure 13: Structural and geochemical setting of $^{40}Ar/^{39}Ar$ samples collected across the *BS*- to *GS*-facies Delfini Shear Zone. a) Outcrop characterization of samples from the Delfini Shear Zone. In general, samples are highly deformed. All analysed samples show a well-developed foliation and stretching lineation sometimes associated with top-to-the E shear bands (e.g. SY-14-26) and/or isoclinal folds (e.g. SY-14-28). b) Thin-section microphotographs of phengite textural habitus showing extent of deformation, more pronounced in SY-16-23 and SY-14-26. c) Chemical composition of phengite in Si *vs.* X_{Mg} space indicating partial recrystallization in SY-14-26 and, to a lesser extent, in SY-14-24.

Figure 14: Step-heating $^{40}Ar/^{39}Ar$ phengite age spectra on single grain and populations from the Delfini Shear Zone. The colour of the age spectra refers to the grade of metamorphism of each sample (green: greenschist; shades of blue: blueschist). Note apparent lack of correlation between the degree of retrogression and apparent age (i.e., the older apparent ages are not systematically measured in *BS*-facies samples). However, the older apparent ages have been measured in calcite-rich samples collected at some distance of the core of the shear zone (i.e. SY-14-28, SY-14-29). TGA: total gas age. Error boxes and TGA are ± 1σ.

Figure 15: Structural and geochemical setting of $^{40}Ar/^{39}Ar$ samples collected across the *GS*-facies Chryssopigi Shear Zone on Sifnos. a) Outcrop characterization of samples collected close to the core of the Chryssopigi Shear Zone. Progressive alignment/parallelisation of folds hinges with the direction of stretching lineation toward the core of the shear zone indicates increasing of deformation (see Roche et al., 2016 for further details). b) Thin-section microphotographs of

phengite textural habitus showing the increasing deformation gradient toward the core of the shear zone (i.e. from SF-14-52 to SF-14-39). c) Chemical composition of phengite in Si *vs.* X_{Mg} space indicating partial recrystallization in SF-14-39 and SF-14-44 and, to a lesser extent, in SF-14-43.

Figure 16: Step-heating $^{40}Ar/^{39}Ar$ phengite age spectra on single grains and populations from the Chryssopigi Shear Zone. The colour of the age spectra refers to the grade of metamorphism of each sample (shades of green: greenschist; shades of blue: blueschist). Excluding sample SF-14-55, the measured apparent ages are younger toward the core of the shear zone (i.e. toward SF-14-43 and SF-14-39). TGA: total gas age. Error boxes and TGA are ± 1σ.

Figure 17: Distribution of *in situ* phengite apparent $^{40}Ar/^{39}Ar$ ages in rock section SF-14-49. a) Picture of the analysed rock-section. b) Range of apparent *in situ* $^{40}Ar/^{39}Ar$ data ranked by age. c) *in situ* laser ablation results located on BSE images. Squares (65 μm) and circles (50 μm) correspond to the diameter of the laser beam with numbers indicating the corresponding analysis (see Appendix S5). Ablation trenches are indicated by tie-lines connecting the endpoints of the rastered area. TGA: total gas age. Error boxes and TGA are ± 1σ.

Figure 18: Projected distribution of $^{40}Ar/^{39}Ar$ ages over regional- to sample-scale strain and retrogression gradients. a) At Syros scale, increasing retrogression and finite deformation from top to base of the UCB is associated with a trend toward younger $^{40}Ar/^{39}Ar$ ages. b) At the scale of a shear zone, the first-order distribution of $^{40}Ar/^{39}Ar$ ages is correlated with strain gradient with younger ages in the most deformed zones. c) At the rock-section scale, *in situ* $^{40}Ar/^{39}Ar$ ages are not correlated with deformation gradients.

Figure 19: Relationships between phengite geochemistry, $^{40}Ar/^{39}Ar$ total-gas ages (TGA) and structural position of dated samples at regional and local scales. The red line corresponds to the trend curve calculated from the data. Error bars correspond to the range of Si-content in phengite and the range of apparent ages measured in each sample. A general but faint trend is observed between lower Si-content in phengite and younger apparent ages in each section.

Figure 20: *In situ* $^{40}Ar/^{39}Ar$ delta age range *versus* the minimum age recorded in a given section. The delta age range anticorrelates almost perfectly (R^2 = 0.997) with the minimum age recorded in a given section, the trend collectively projecting to a nominal zero-spread end-member age around ca. 51 Ma.

Figure 21: Cooling rate (°C/Myr) *vs.* apparent ages (Ma) modelled from grainsize *vs.* $^{40}Ar/^{39}Ar$ relationships reported in the Chroussa subunit (Myttakas section) by Uunk et al. (2018). An apparent phase-lag up to 2 Myr is revealed for these samples merely 100 m apart, indicating that the ages recorded most probably reflect variable diffusion-driven resetting rather than true cooling ages.

endpoints of the rastered area. TGA: total gas age. Error boxes and TGA are ± 1σ.

Figure 18: Projected distribution of $^{40}Ar/^{39}Ar$ ages over regional- to sample-scale strain and retrogression gradients. a) At Syros scale, increasing retrogression and finite deformation from top to base of the UCB is associated with a trend toward younger $^{40}Ar/^{39}Ar$ ages. b) At the scale of a shear zone, the first-order distribution of $^{40}Ar/^{39}Ar$ ages is correlated with strain gradient with younger ages in the most deformed zones. c) At the rock-section scale, *in situ* $^{40}Ar/^{39}Ar$ ages are not correlated with deformation gradients.

Figure 19: Relationships between phengite geochemistry, $^{40}Ar/^{39}Ar$ total-gas ages (TGA) and structural position of dated samples at regional and local scales. The red line corresponds to the trend curve calculated from the data. Error bars correspond to the range of Si-content in phengite and the range of apparent ages measured in each sample. A general but faint trend is observed between lower Si-content in phengite and younger apparent ages in each section.

Figure 20: *In situ* $^{40}Ar/^{39}Ar$ delta age range *versus* the minimum age recorded in a given section. The delta age range anticorrelates almost perfectly (R^2 = 0.997) with the minimum age recorded in a given section, the trend collectively projecting to a nominal zero-spread end-member age around ≃ca. 51 Ma.

Figure 21: Cooling rate (°C/Myr) *vs.* apparent ages (Ma) modelled from grainsize *vs.* $^{40}Ar/^{39}Ar$ relationships reported in the Chroussa subunit (Myttakas section) by Uunk et al. (2018). An apparent phase-lag up to 2 Myr is revealed for these samples merely 100 m apart, indicating that the ages recorded most probably reflect variable diffusion-driven resetting rather than true cooling ages.

Table 1: Lithology and mineralogy of dated samples. Mineral abbreviations after Whitney and Evans (2010).

Samples	Location	Mineralogy										Lithology	GPS coordinate (WGS 84)	
		Ph	Pg	Omp	Grt	Gln	Ep	Chl	Ab	Qz	Cal		Latitude	Longitude
SY-14-21	Posidonia	x			x	x	x	x		x	x	Chl micaschist	37.363221	24.877139
SY-14-18	Posidonia	x		x	x	x	x	x	x	x	x	Grt-Ep blueschist	37.370155	24.884351
SYR-13-02	Posidonia	x						x	x	x		Gneiss	37.373456	24.892570
SY-16-10	Posidonia	x	?					x		x	x	Calcschist	37.375466	24.906279
SY-14-80	Posidonia	x					x	x	x	x	x	Chl micaschist	37.381565	24.916839
SY-14-76	Posidonia	x					x	x	x	x	x	Chl calcschist	37.385748	24.931293
SY-14-77	Posidonia	x			x			x	x	x		Chl micaschist	37.385892	24.934383
SY-16-06	Chroussa	x	?			x	x	x				Grt-Ep blueschist	37.385203	24.937226
SY-16-15	Chroussa	x	?			x						Blueschist	37.388568	24.941572
SY-14-40b2	Kampos	x	x		x	x	x	x	x	x		Grt-Ep blueschist	37.386778	24.951097
SY-14-40b4	Kampos	x					x	x	x	x		Greenschist	37.386778	24.951097
SY-14-60	Kampos	x		x	x	x	x			x	x	Gln eclogite	37.389130	24.953722
SY-14-63	Kampos	x		x	x	x	x	x	x		x	Gln eclogite	37.389130	24.953722
SY-14-64	Kampos	x		x	x		x		x	x		Gln eclogite	37.389130	24.953722
SY-16-18	Vari Unit	x						x	x	x		Greenschist	37.392992	24.953989
SY-14-68	Vari Unit	x						x	x	x		Gneiss	37.403223	24.969233
SY-13-10	Vari Unit	x						x	x	x		Chl micaschist	37.408158	24.965869
SY-14-74	Lia SZ	x		x								Eclogite	37.492053	24.907270
SY-14-71	Lia SZ	x		x		x						Gln eclogite	37.491166	24.900779
SY-14-73	Lia SZ	x		x	x	x		x		x		Omp-Grt blueschis	37.492934	24.900877
SY-16-23	Delfini SZ	x	?				x	x	x	x		Chl micaschist	37.458322	24.890958
SY-14-30	Delfini SZ	x	?			x	x	x		x		Ep blueschist	37.460031	24.891500
SY-14-24	Delfini SZ	x			x	x	x	x	x	x		Grt-Ep blueschist	37.461260	24.893487
SY-14-26	Delfini SZ	x	x		x			x		x	x	Grt micaschist	37.463579	24.894134
SY-14-28	Delfini SZ	x			x	x	x	x		x	x	Grt-Gln calcschist	37.464079	24.893883
SY-14-29	Delfini SZ	x				x		x			x	Marble	37.464260	24.893912
SF-14-55	Chryssopigi SZ	x				x	x	x		x		Ab-Ep-Gln bluesch	36.948104	24.756036
SF-14-52	Chryssopigi SZ	x					x	x	x	x	x	Chl calcschist	36.946791	24.755715
SF-14-51	Chryssopigi SZ	x						x		x	x	Chl calcschist	36.945332	24.755298
SF-14-50	Chryssopigi SZ	x				x	x	x		x	x	Chl marble	36.943661	24.752789
SF-14-49	Chryssopigi SZ	x						x	x	x	x	Chl calcschist	36.942468	24.751587
SF-14-44	Chryssopigi SZ	x	x				x	x		x	x	Chl micaschist	36.938757	24.743623
SF-14-39	Chryssopigi SZ	x					x	x	x	x	x	Chl micaschist	36.936358	24.744940
SF-14-43	Chryssopigi SZ	x					x	x	x	x	x	Chl micaschist	36.935908	24.746873

Table 2: Petro-textural description of phengite and measured 40Ar/39Ar ages. The textural habitus of phengite was determined after pictures of grains taken before irradiation. Deformation of phengite was mainly characterised following the degree of mica alignment.

Samples	Textural habitus	Deformation	Chemical composition	Compositional zoning	Inclusion	Grain size (μm)	40Ar/39Ar age (Ma)
SY-14-21	primary - partial recrystallization	moderate	-	-	rare	125-250	35-23
SY-14-18	primary	low	homogeneous	-	rare	125-250	32-27
SYR-13-02	primary to recrystallized	intense	heterogeneous	patchy	few	250-500	20.72 ± 0.27
SY-16-10	primary - partial recrystallization	moderate	-	-	few	250-500	26-20
SY-14-80	recrystallized (secondary)	intense	homogeneous	-	few	125-250	18.00 ± 0.14
SY-14-76	primary	low	heterogeneous	patchy	rare	125-250	33-29
SY-14-77	recrystallized (secondary)	intense	heterogeneous	sectorial	few	125-250	21-18
SY-16-06	primary	low	-	-	few	250-500	40-37
SY-16-15	primary	undeformed	-	-	rare	1000-2000	42-40
SY-14-40b2	primary - partial recrystallization	moderate	homogeneous	-	rare	500-1000	30-21
SY-14-40b4	primary to recrystallized	low to intense	heterogeneous	sectorial	rare	250-500	39-36
SY-14-60	primary - partial recrystallization	moderate	heterogeneous	concentric	frequent	500-1000	44-42
SY-14-63	primary	moderate	heterogeneous	concentric	frequent	250-500	44-40
SY-14-64	primary	moderate	heterogeneous	sectorial & concentric	frequent	250-500	44-42
SY-16-18	primary - partial recrystallization	moderate	-	-	frequent	250-500	144-105
SY-14-68	primary	moderate	homogeneous	-	frequent	1000-2000	80-60
SY-13-10	recrystallized (secondary)	Intense	homogeneous	-	frequent	500-1000	42-59
SY-14-74	primary	undeformed	-	-	rare	250-500	52-48
SY-14-71	primary	moderate	homogeneous	-	frequent	1000-2000	47.09 ± 0.21
SY-14-73	primary to recrystallized	intense	heterogeneous	sectorial & concentric	frequent	250-500	51-24
SY-16-23	primary - partial recrystallization	intense	-	-	few	125-250	39-33
SY-14-30	primary	moderate	-	-	few	250-500	37-33
SY-14-24	primary - partial recrystallization	intense	heterogeneous	sectorial & concentric	few	500-1000	35-32
SY-14-26	primary - partial recrystallization	intense	heterogeneous	sectorial & concentric	rare	500-1000	34-31
SY-14-28	primary	moderate	homogeneous	-	rare	500-1000	38.45 ± 0.23
SY-14-29	primary	low	-	-	rare	1000-2000	39.04 ± 0.22
SF-14-55	primary	moderate	heterogeneous	patchy	rare	250-500	26-22
SF-14-52	primary - partial recrystallization	low to moderate	heterogeneous	concentric	few	250-500	36-31
SF-14-51	primary - partial recrystallization	moderate	homogeneous	-	rare	250-500	34.48 ± 0.2
SF-14-50	primary	moderate	heterogeneous	concentric	rare	500-1000	27-22
SF-14-49	primary - partial recrystallization	low to intense	heterogeneous	sectorial	rare	250-500	35-30
SF-14-44	primary to recrystallized	intense	homogeneous	-	few	125-250	26-22
SF-14-39	recrystallized (secondary)	intense	homogeneous	-	few	125-250	27-22
SF-14-43	primary to recrystallized	intense	heterogeneous	sectorial & concentric	few	250-500	24-20

Figure 1

Click here to access/download;Figure;Figure-1.png

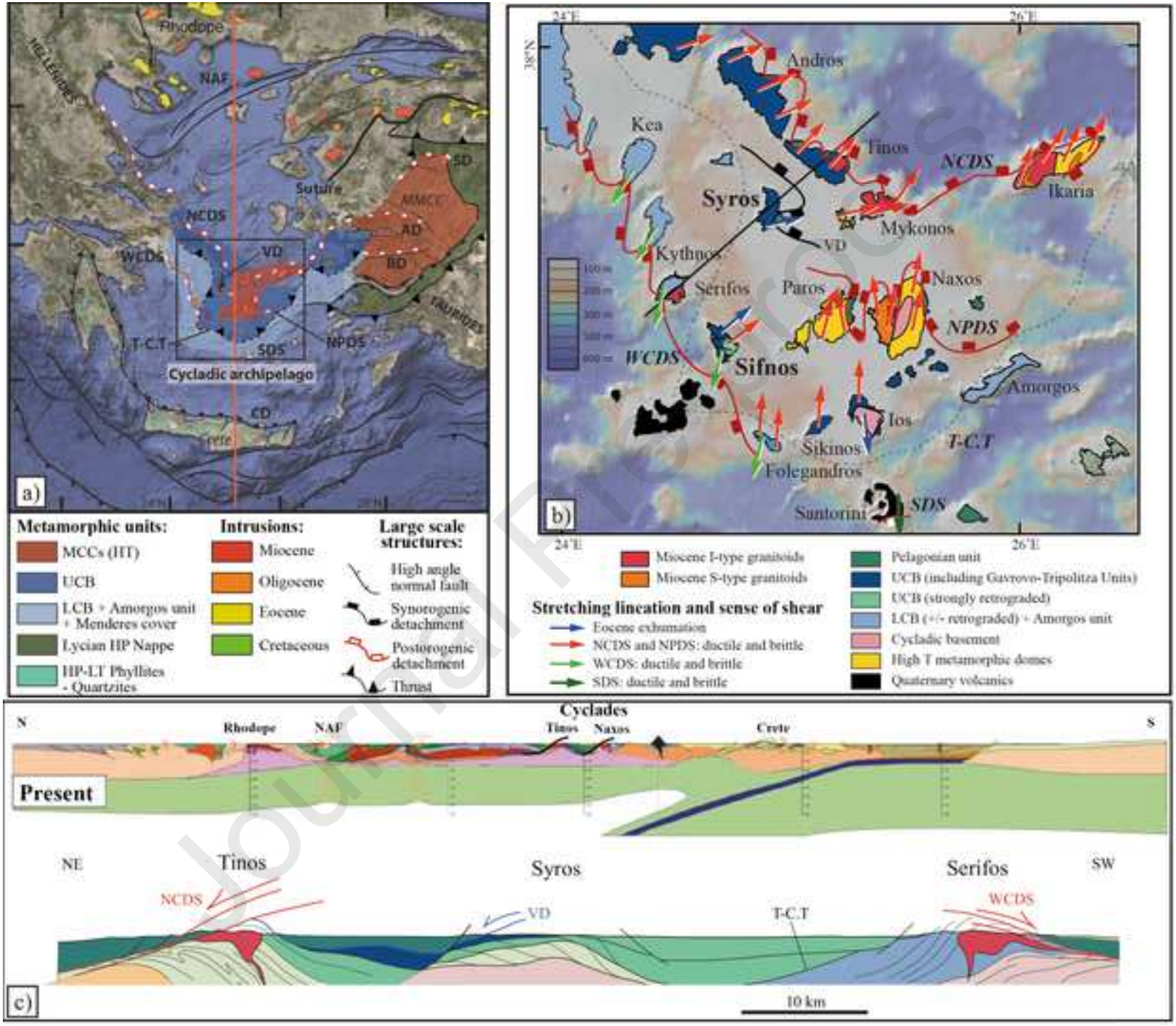

Figure 2

Click here to access/download;Figure;Figure-2.png

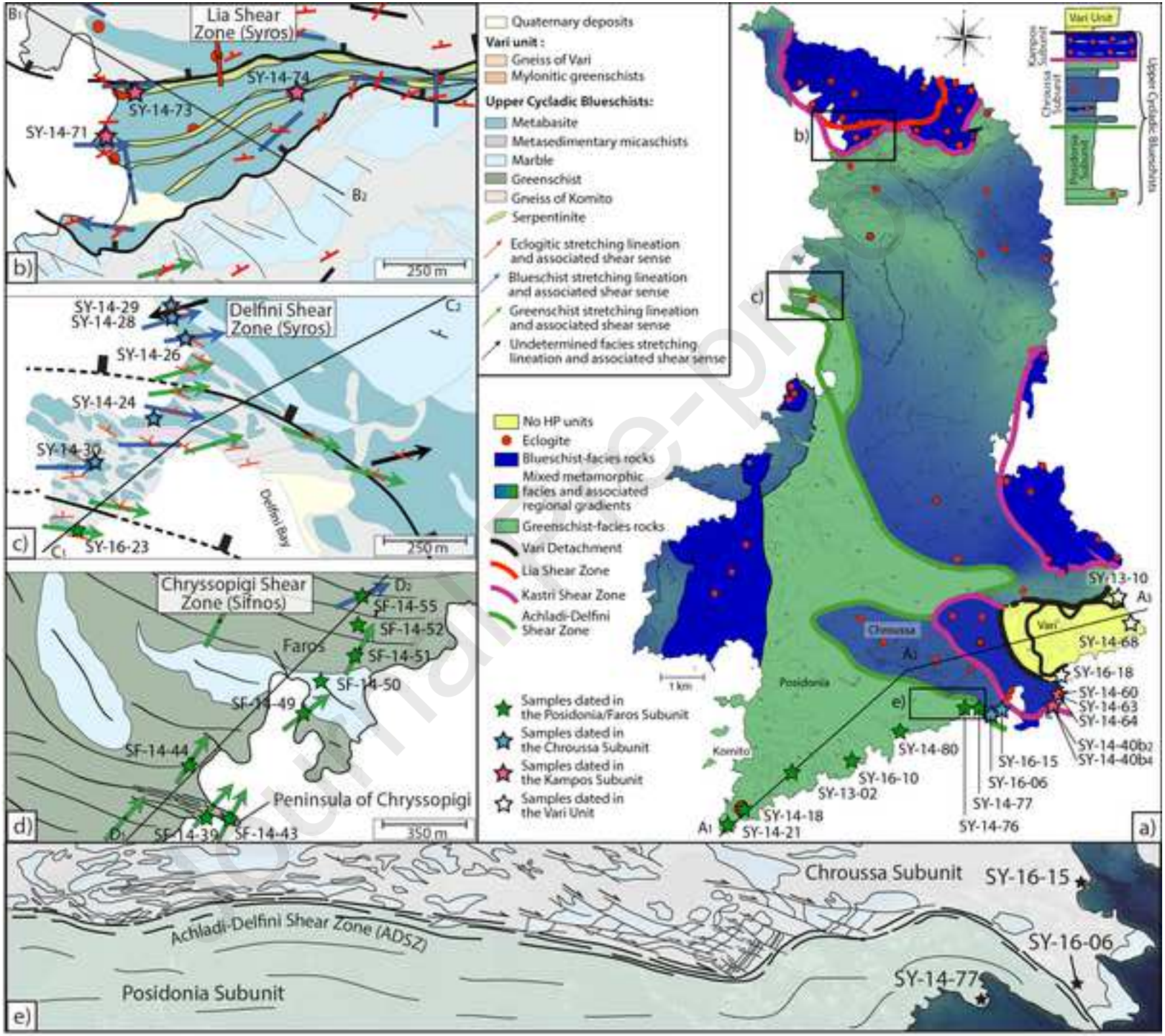

Figure 3

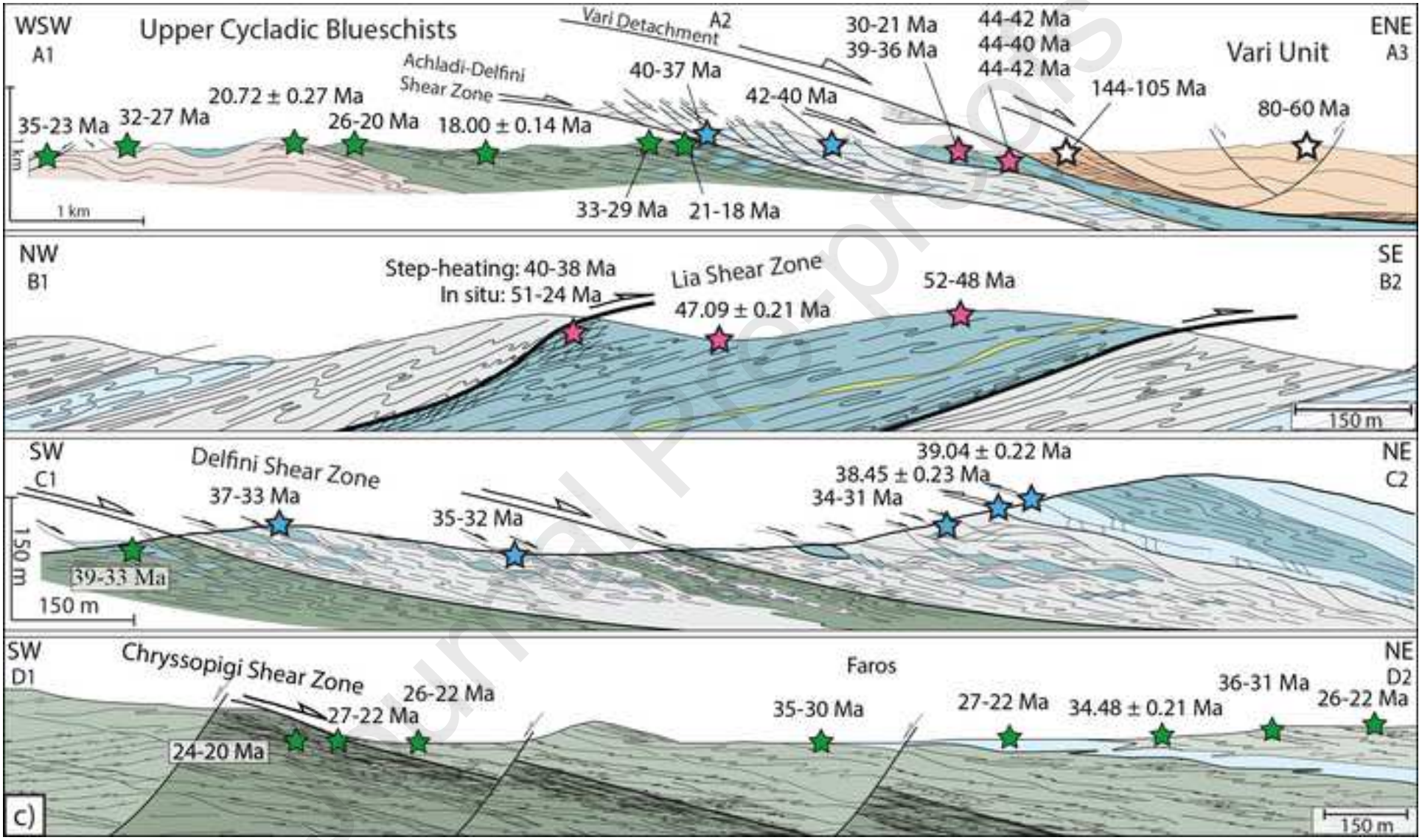

Figure 4

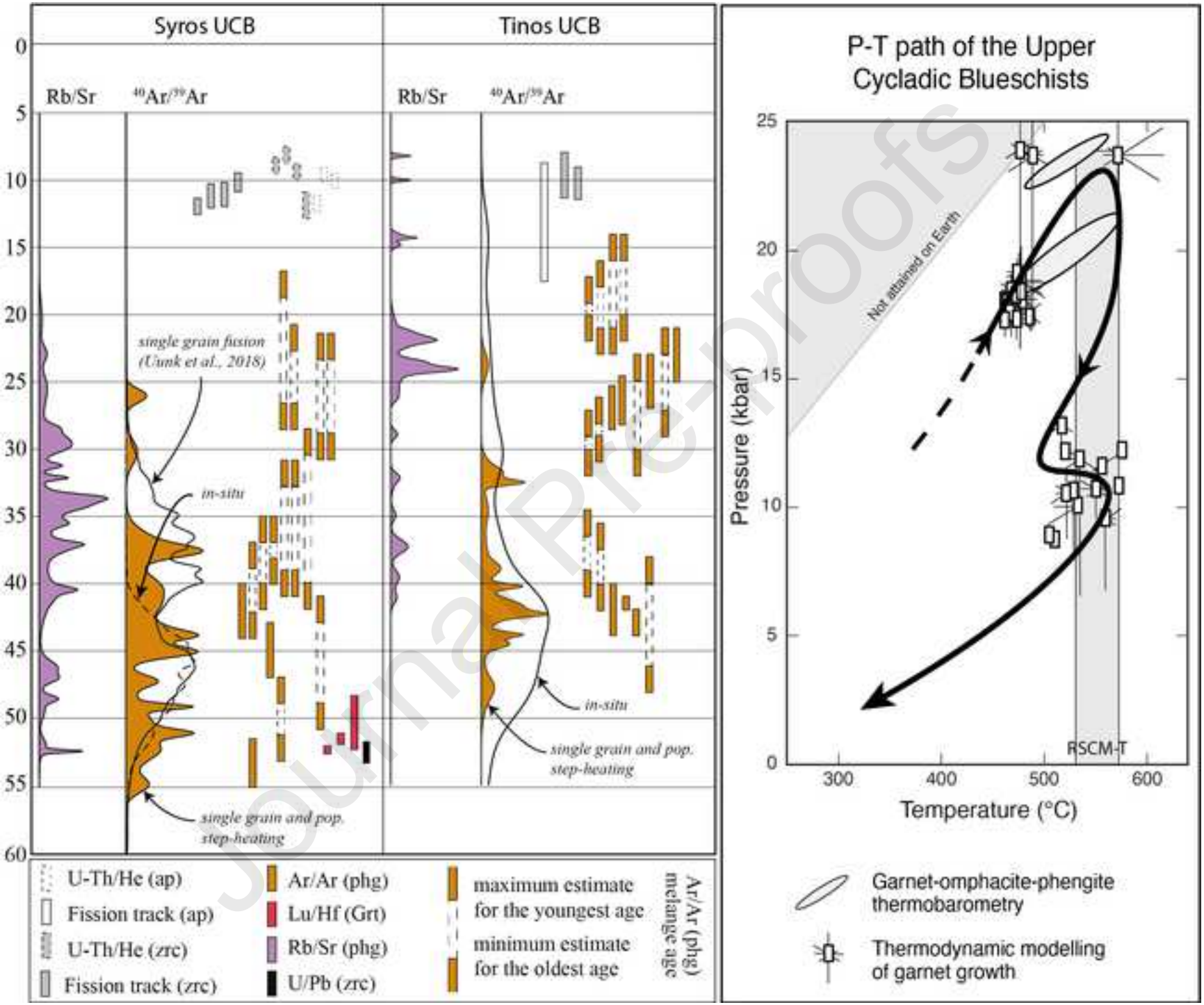

Figure 5

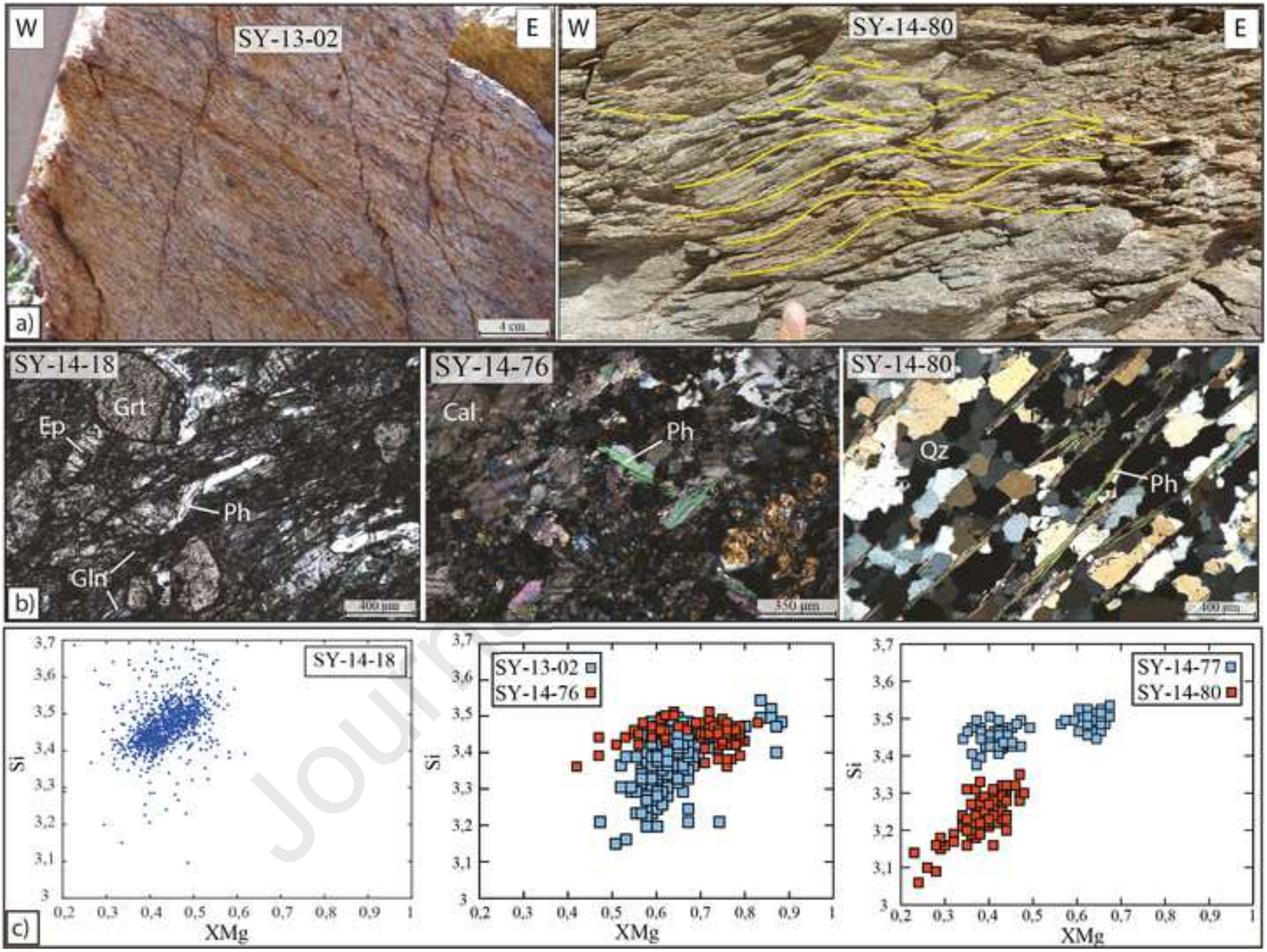

Figure 6

Click here to access/download;Figure;Figure-6.png

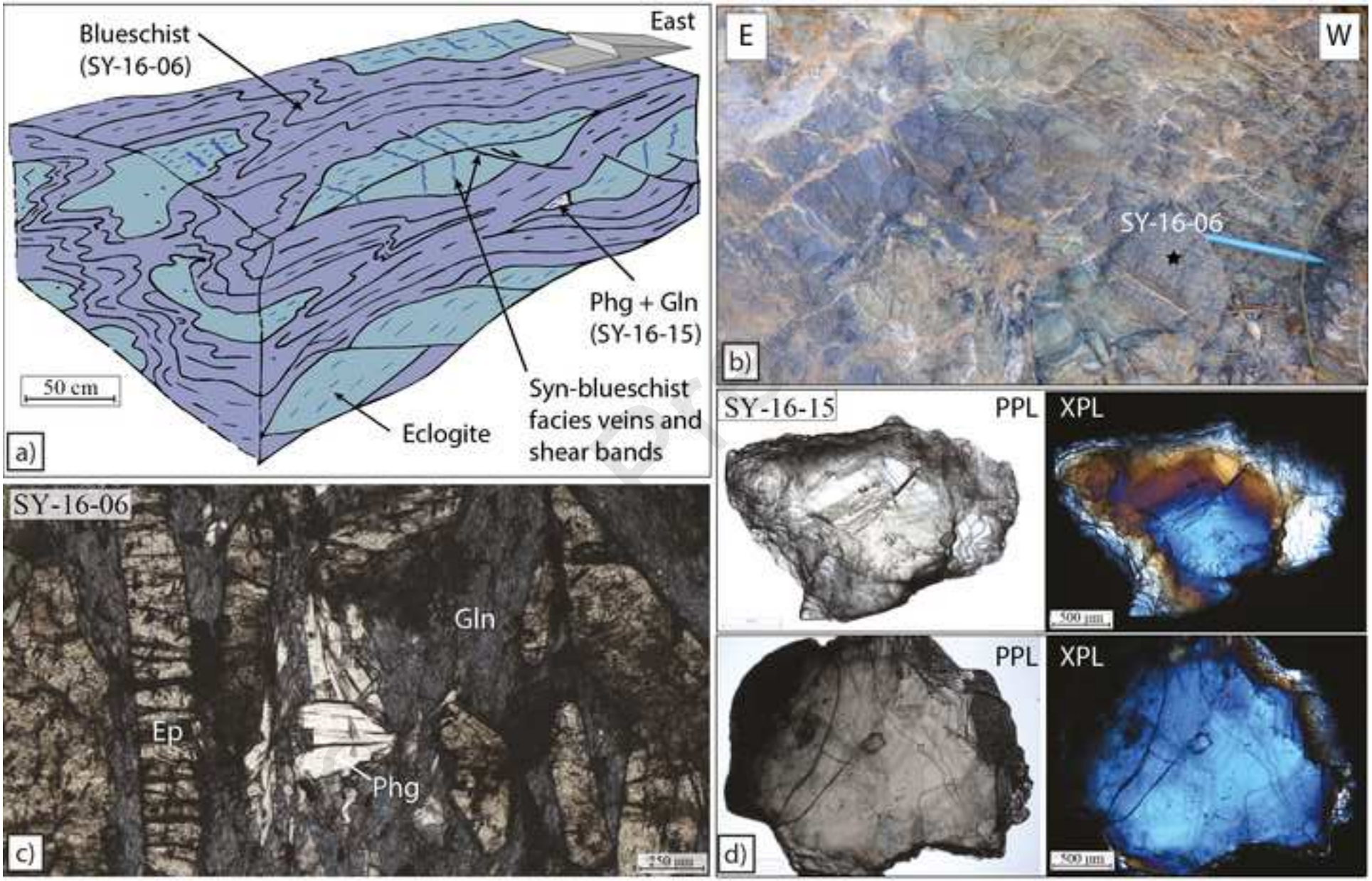

Figure 7

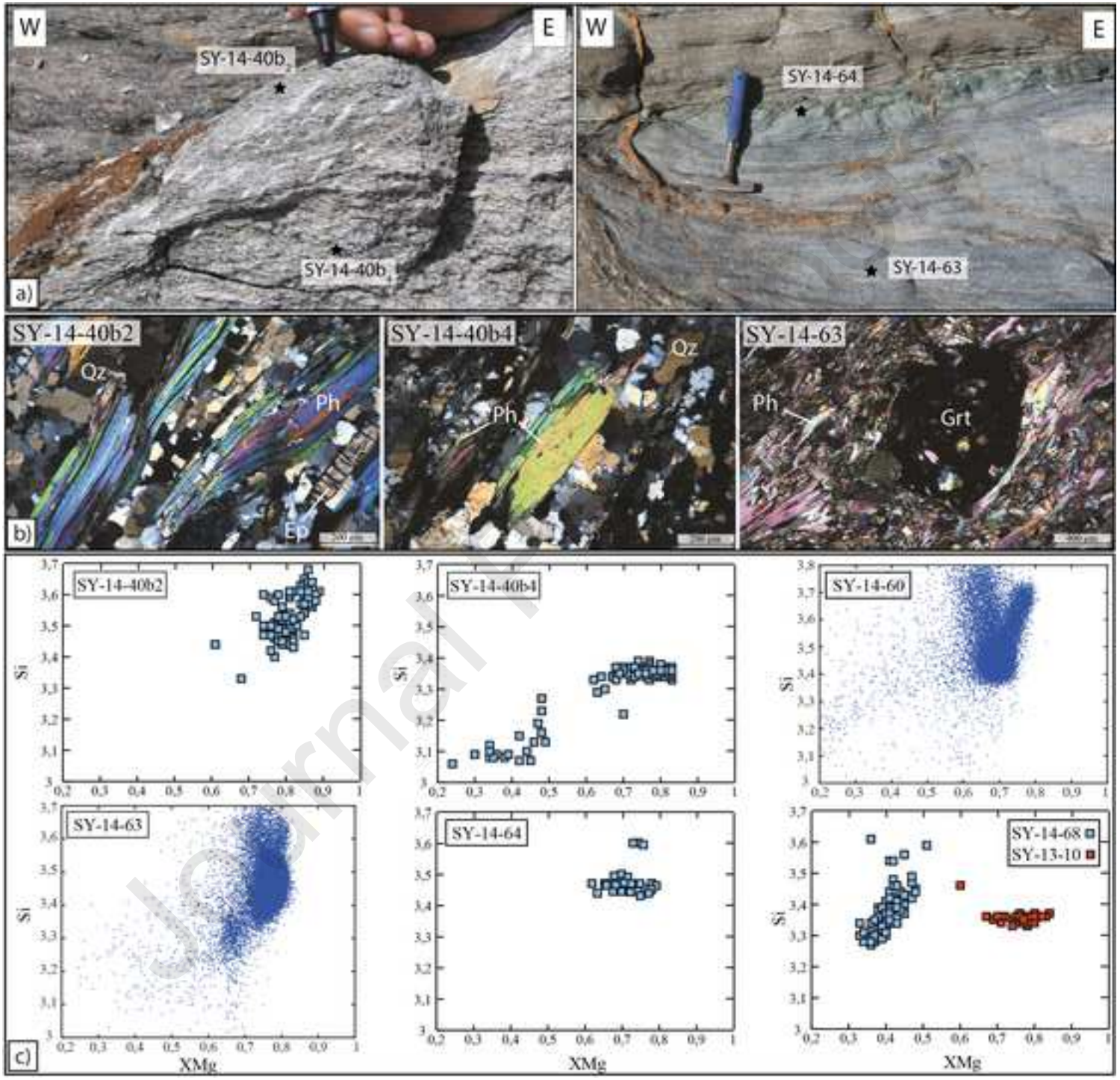

Figure 8

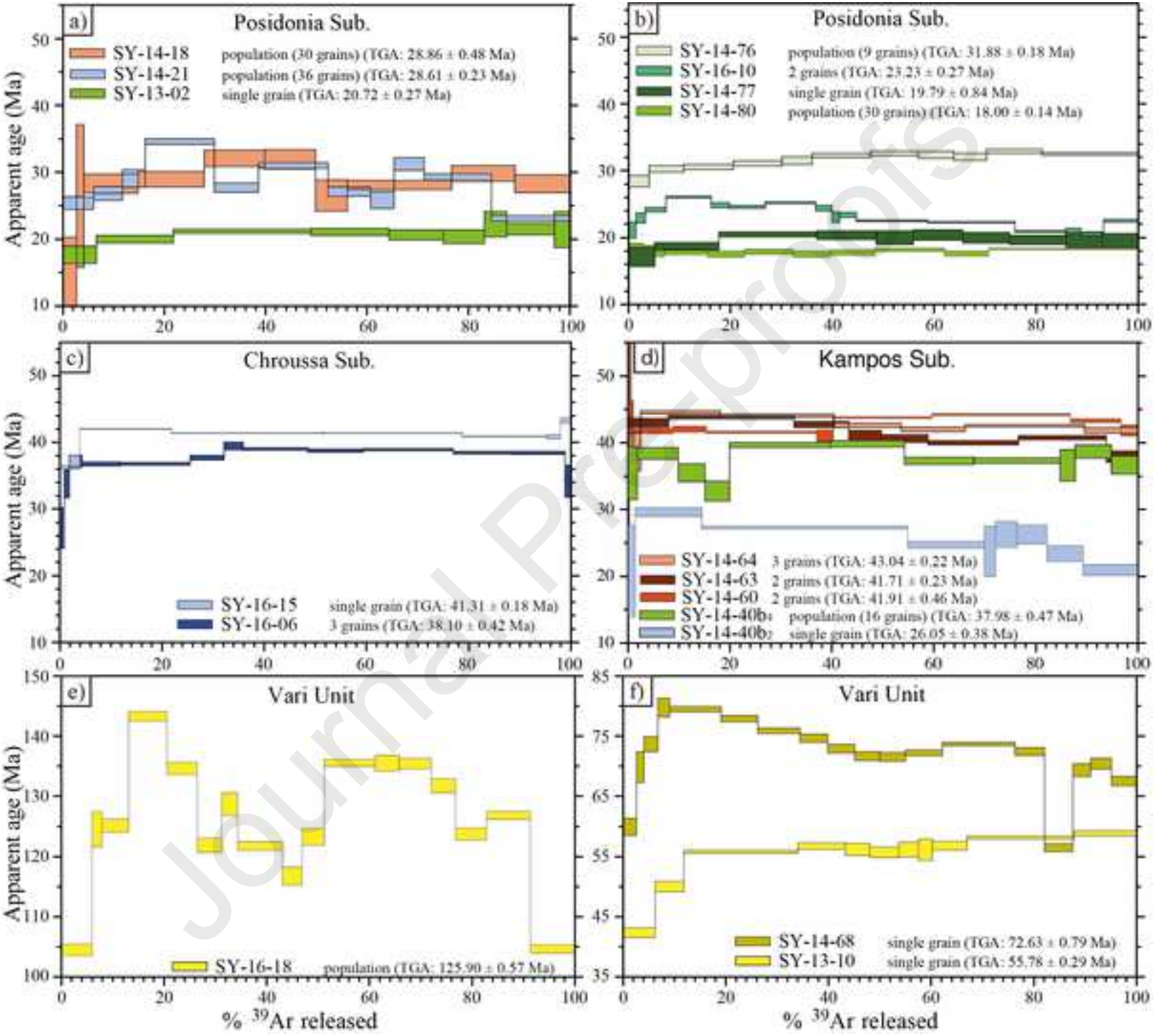

Figure 9

Click here to access/download;Figure;Figure-9.png

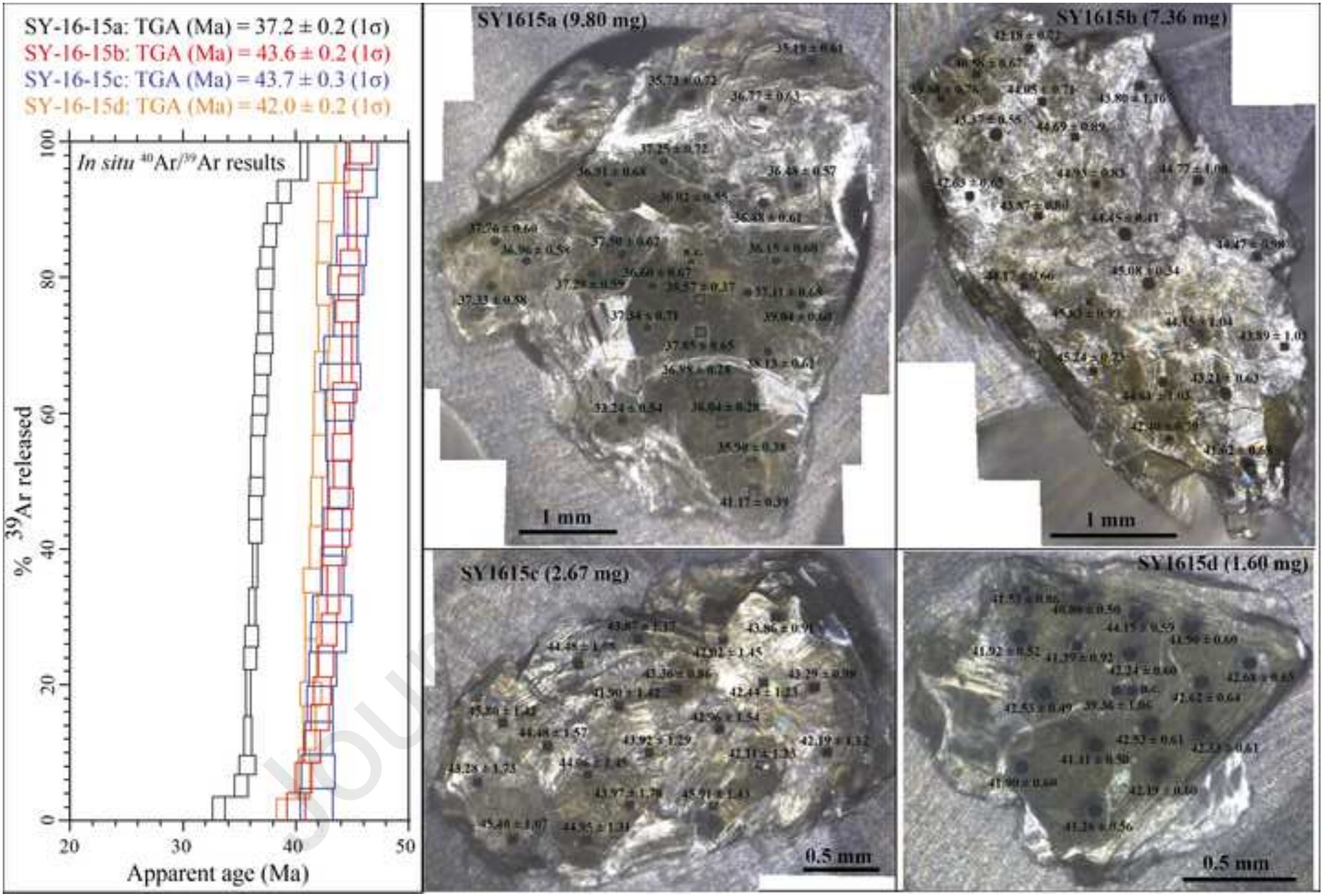

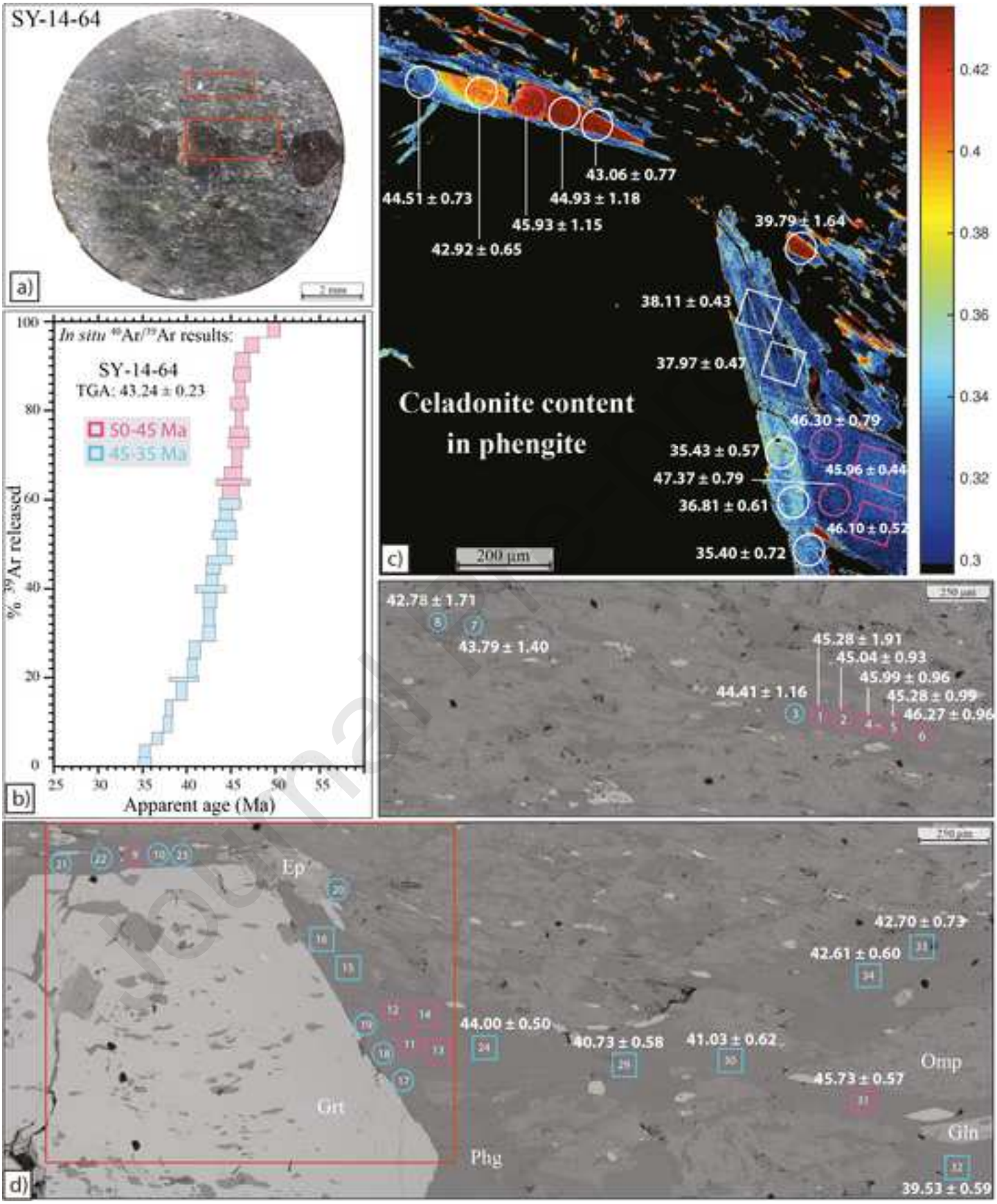

Figure 11

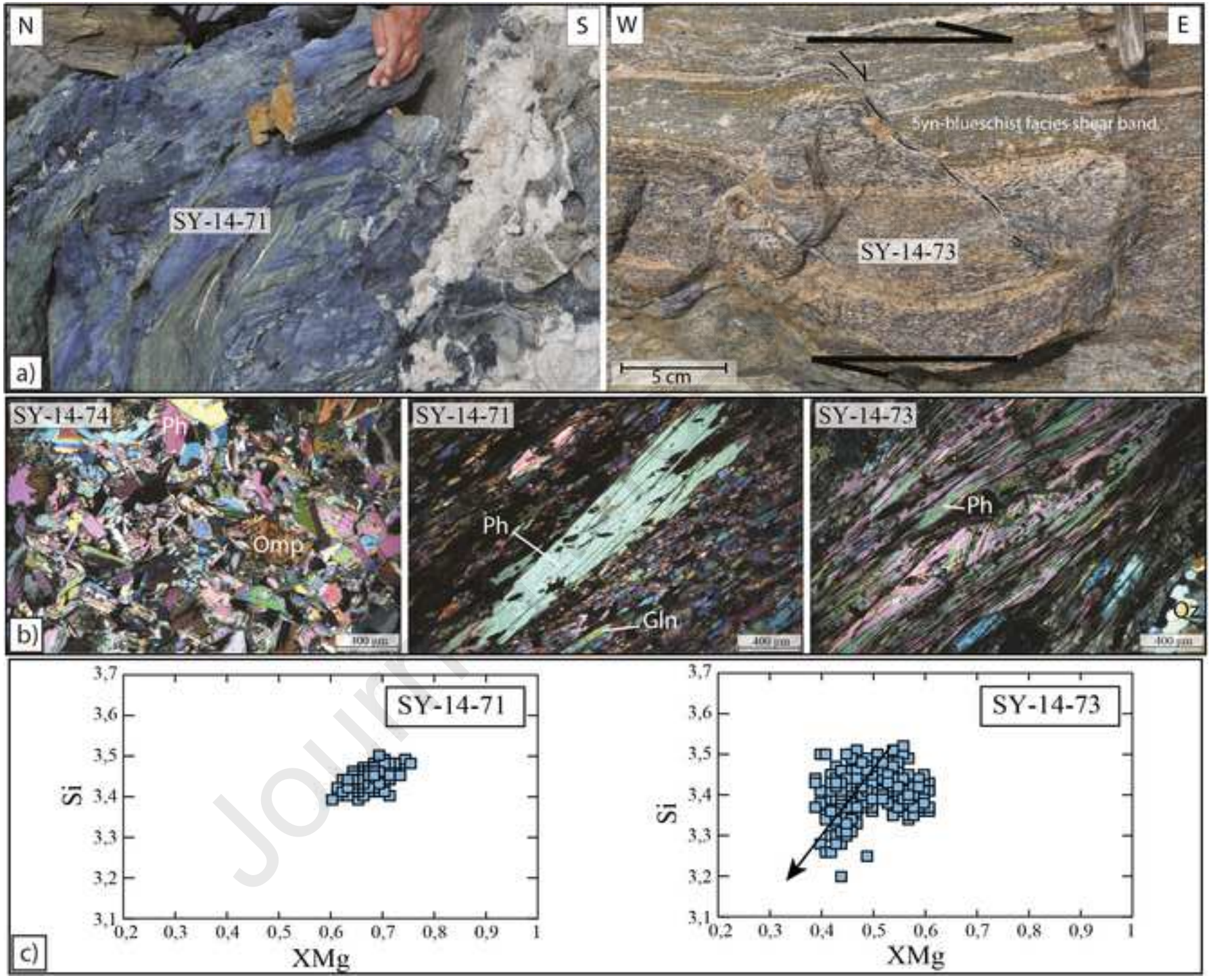

Figure 12

Click here to access/download;Figure;Figure-12.png

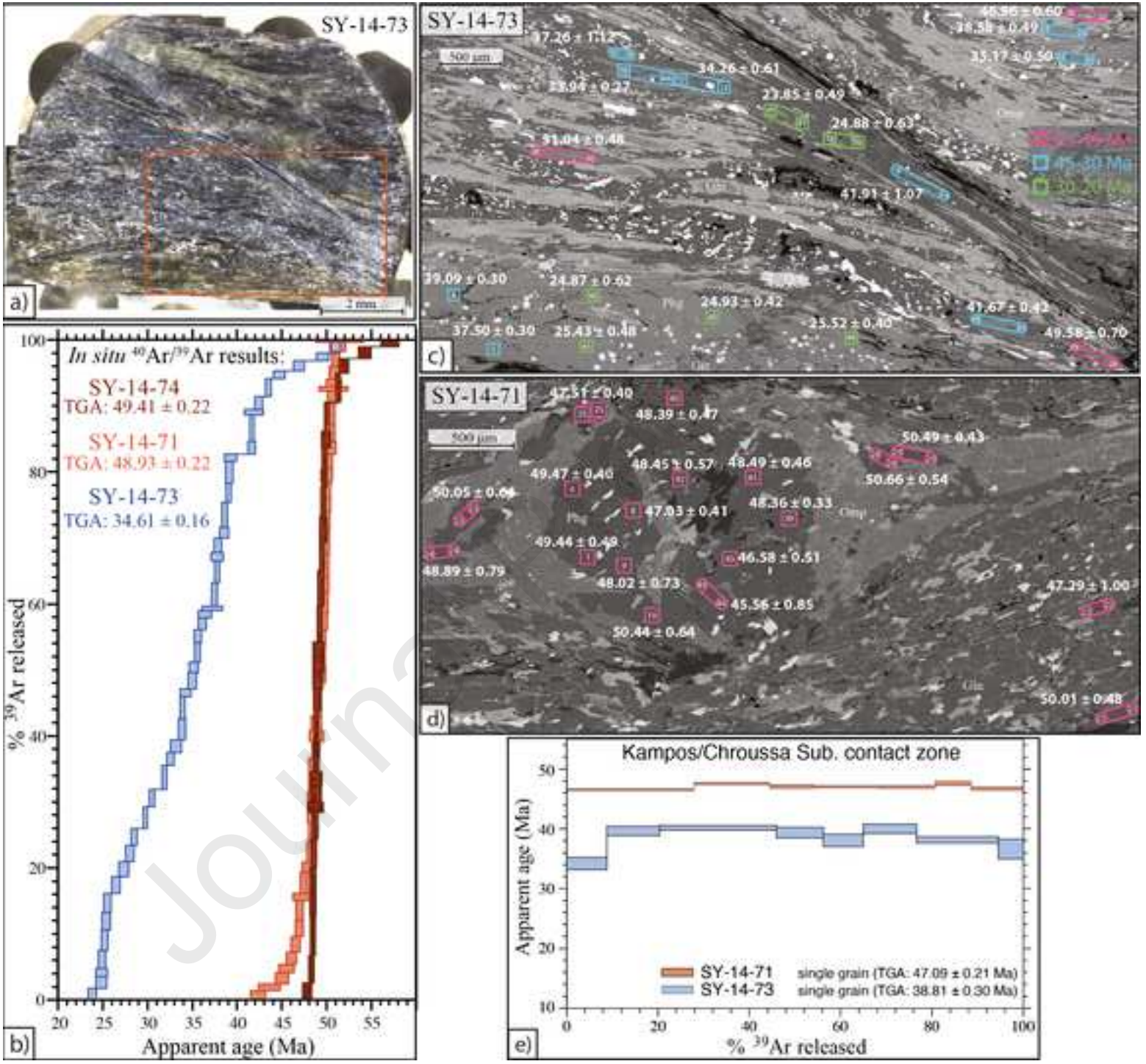

Figure 13

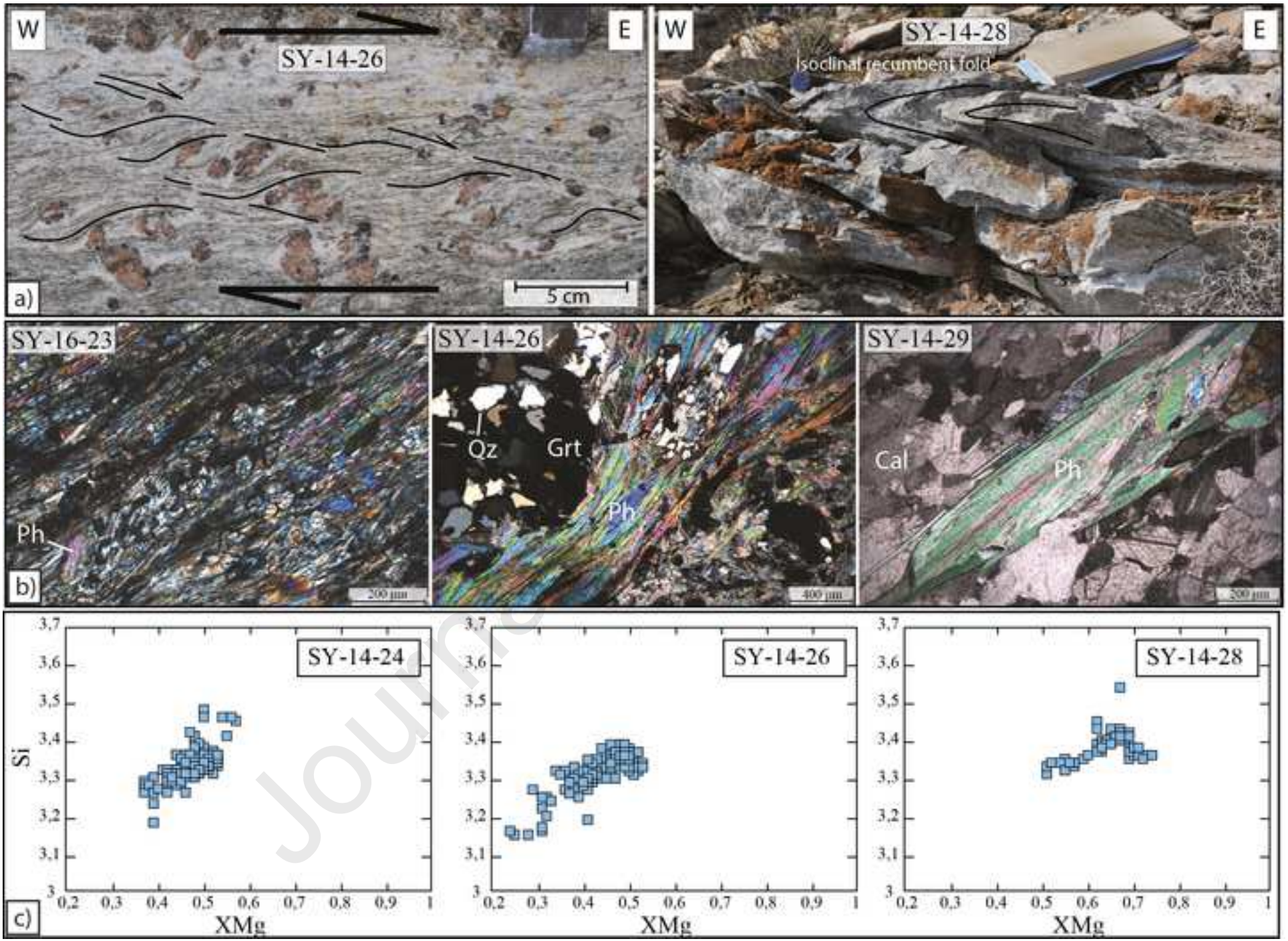

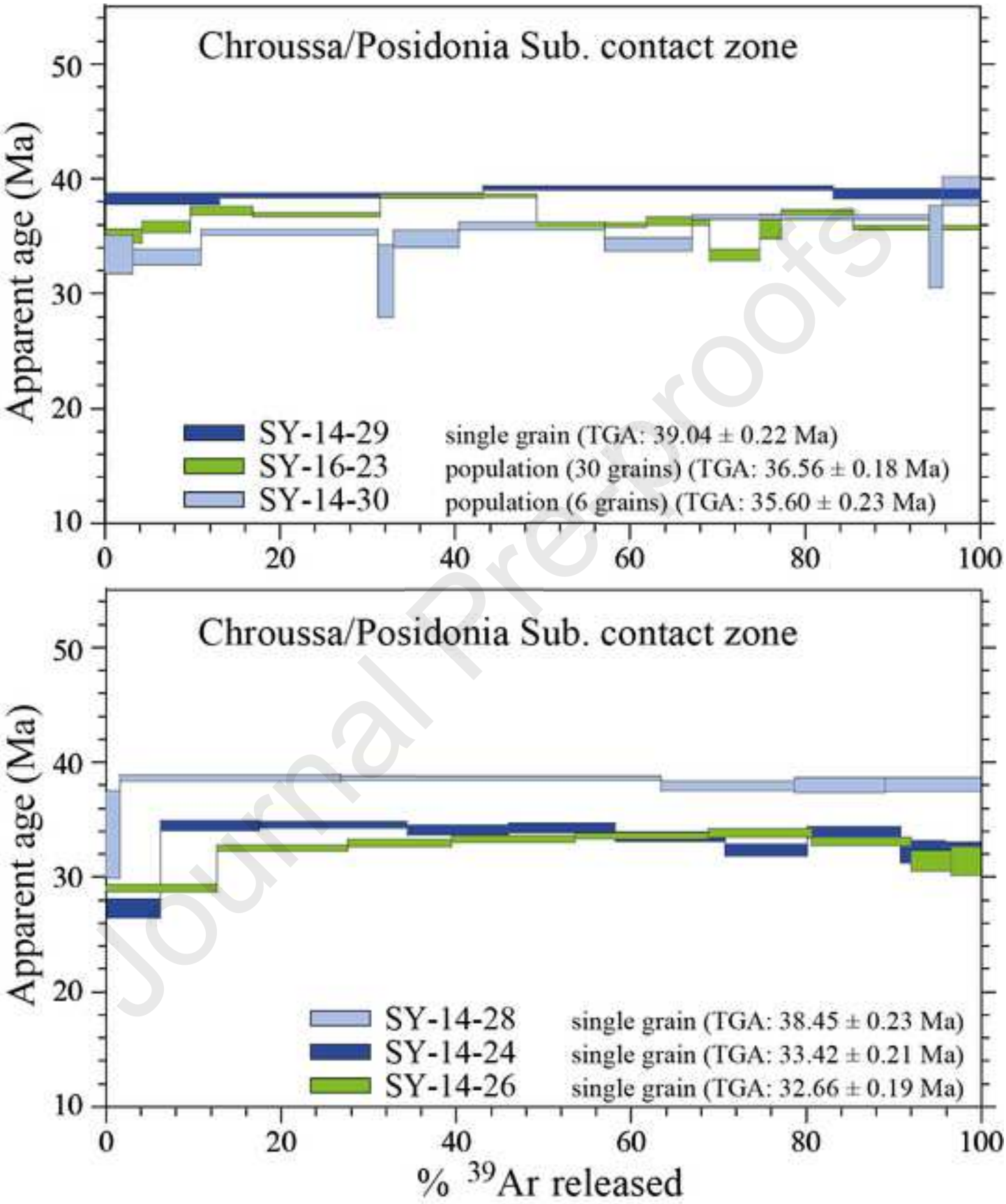

Figure 15

Click here to access/download;Figure;Figure-15.png

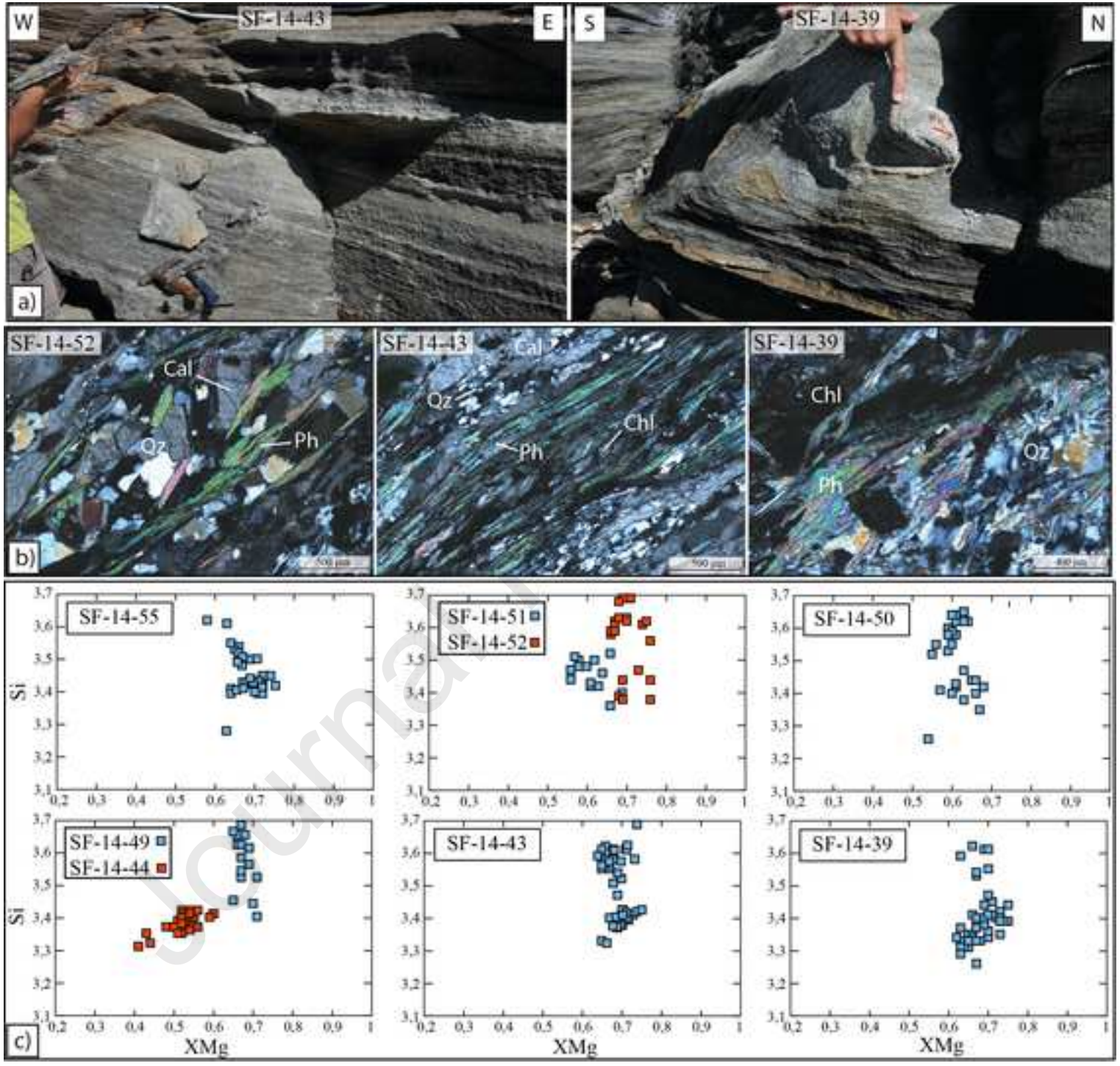

Figure 16

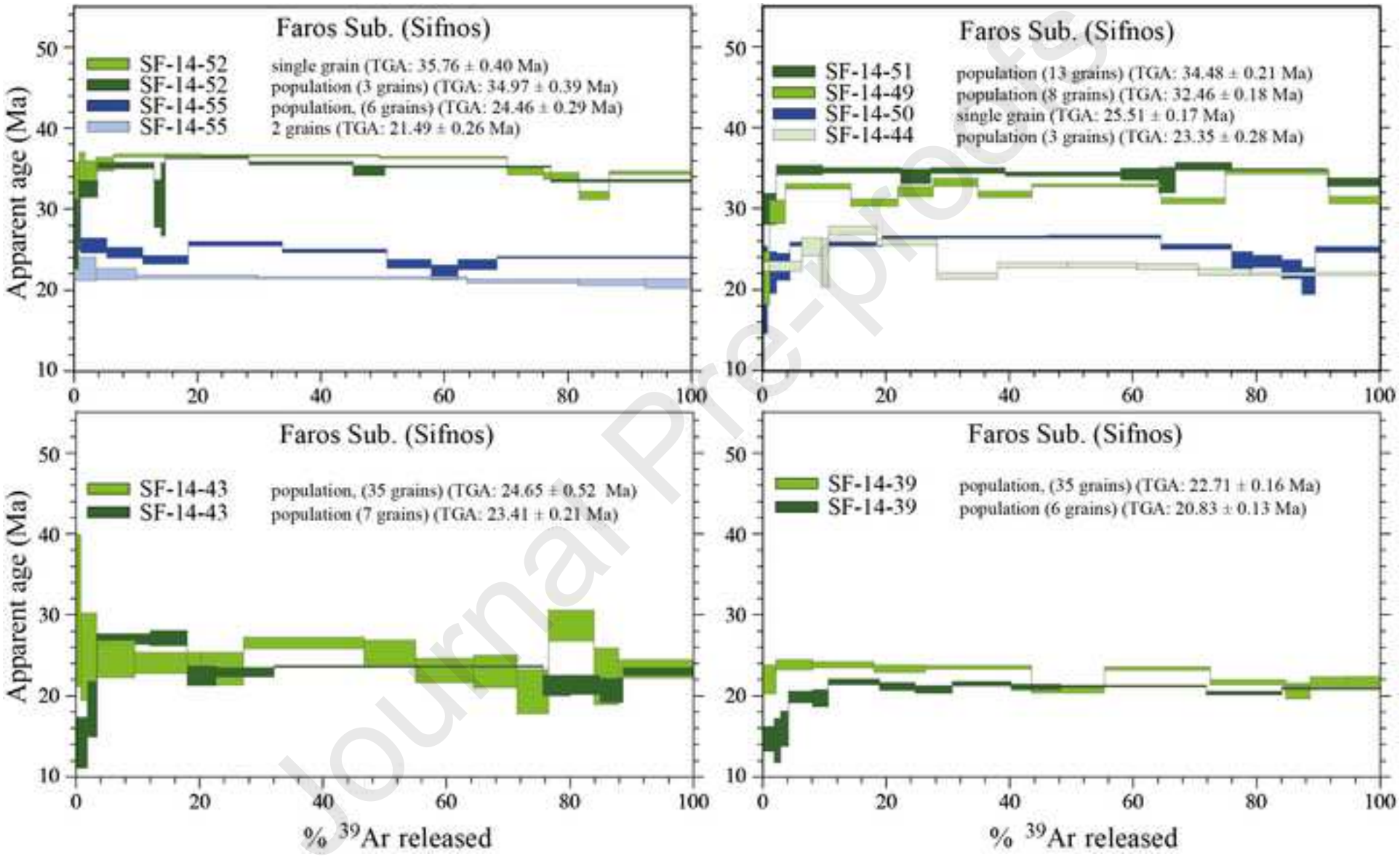

Figure 17

Click here to access/download;Figure;Figure-17.png

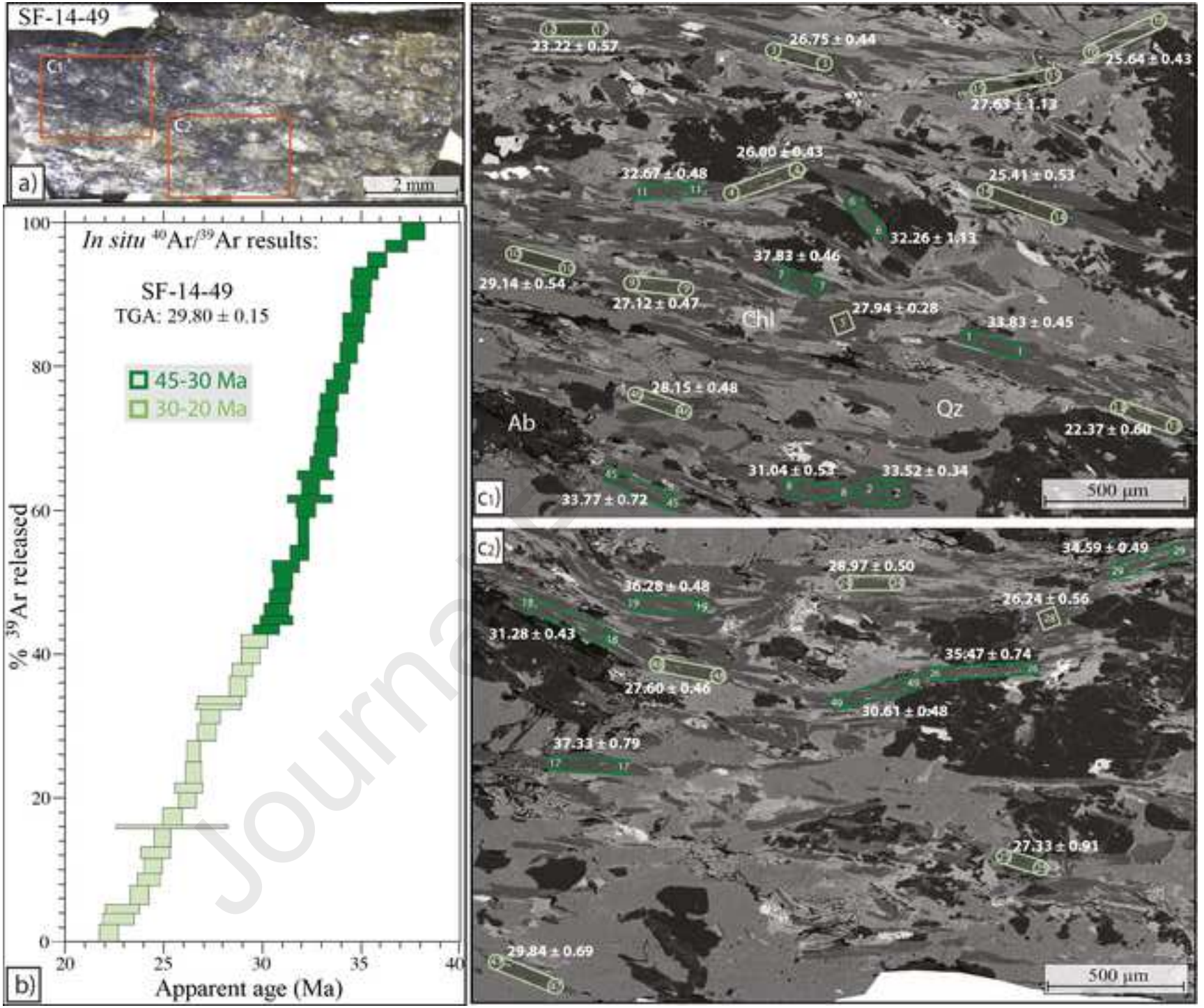

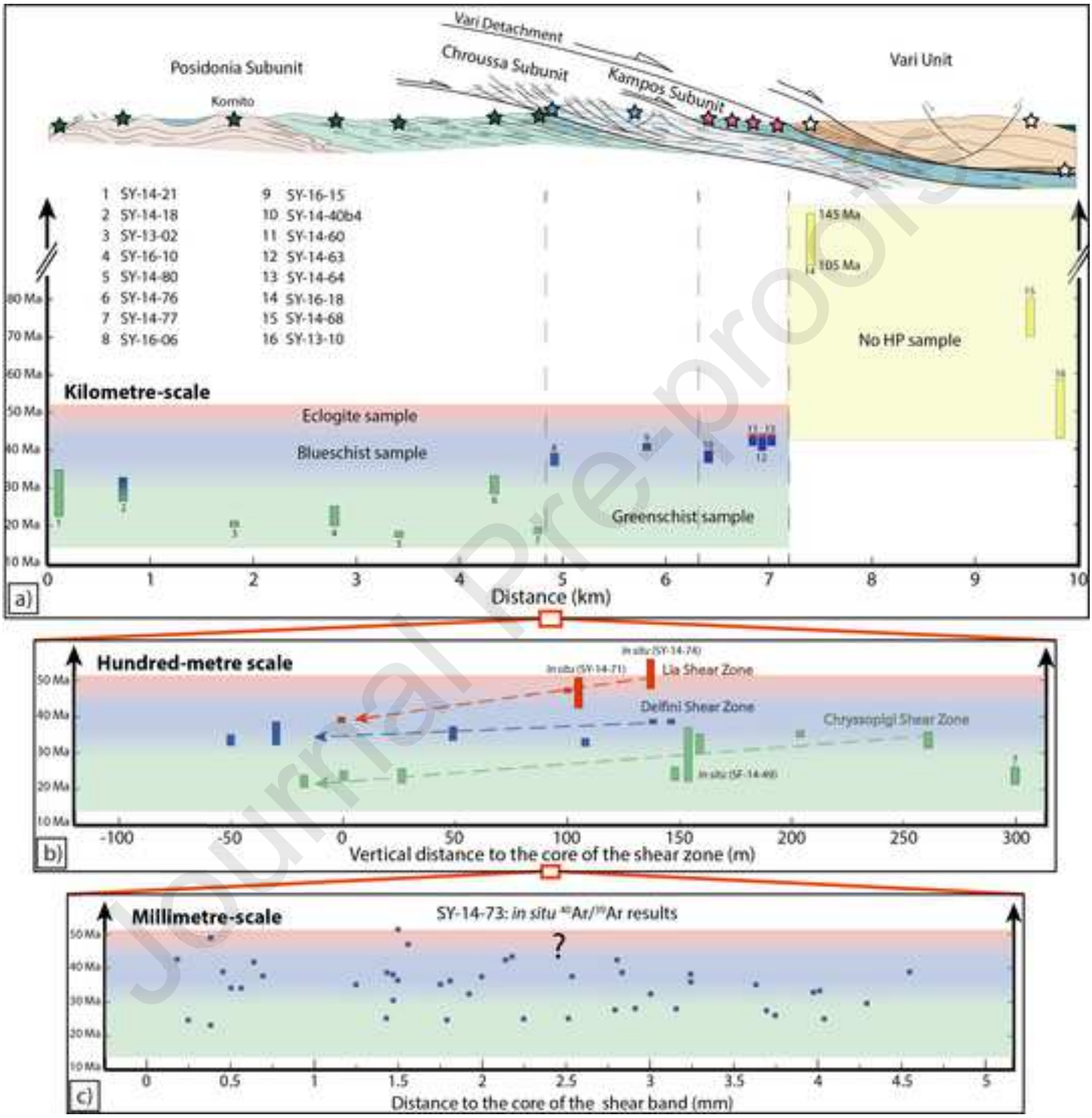

Figure 19

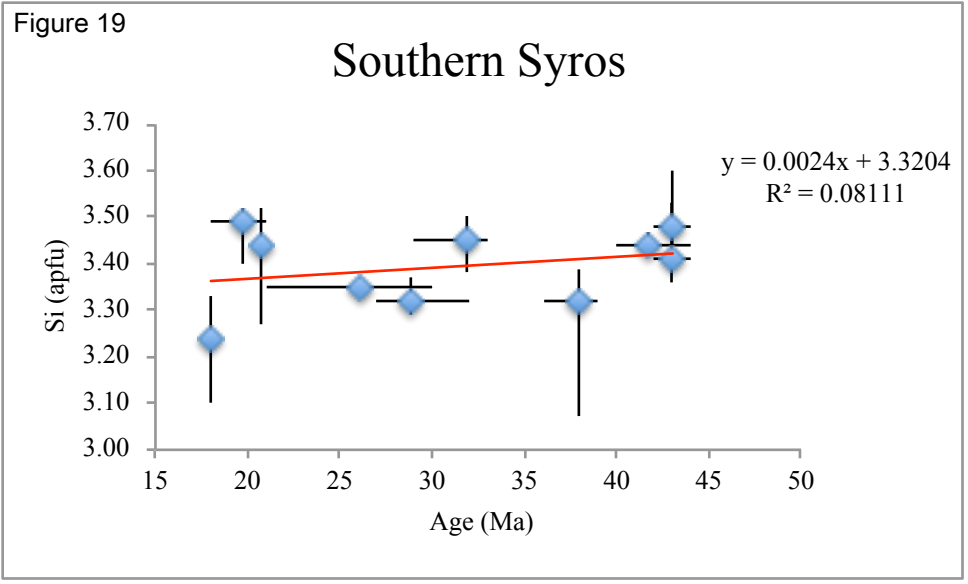

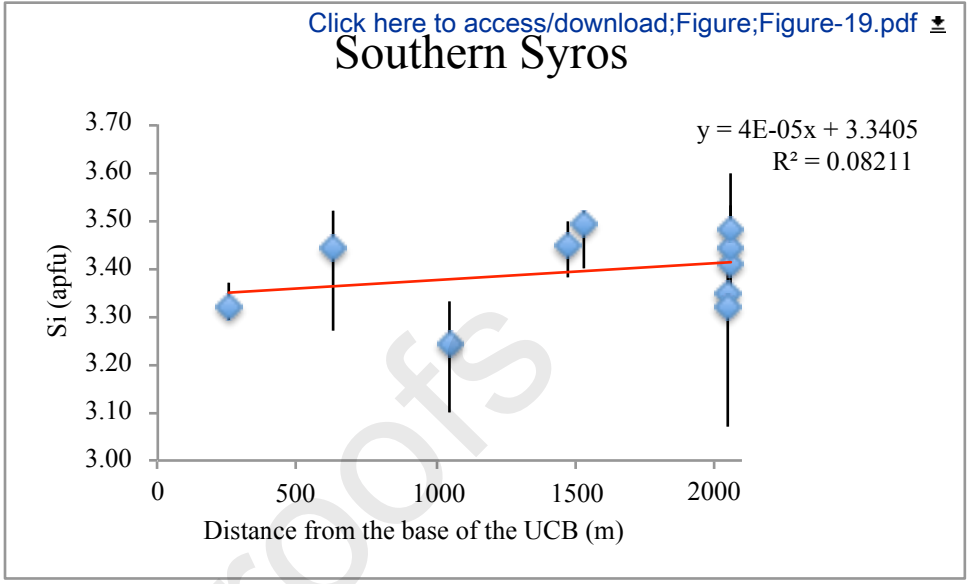

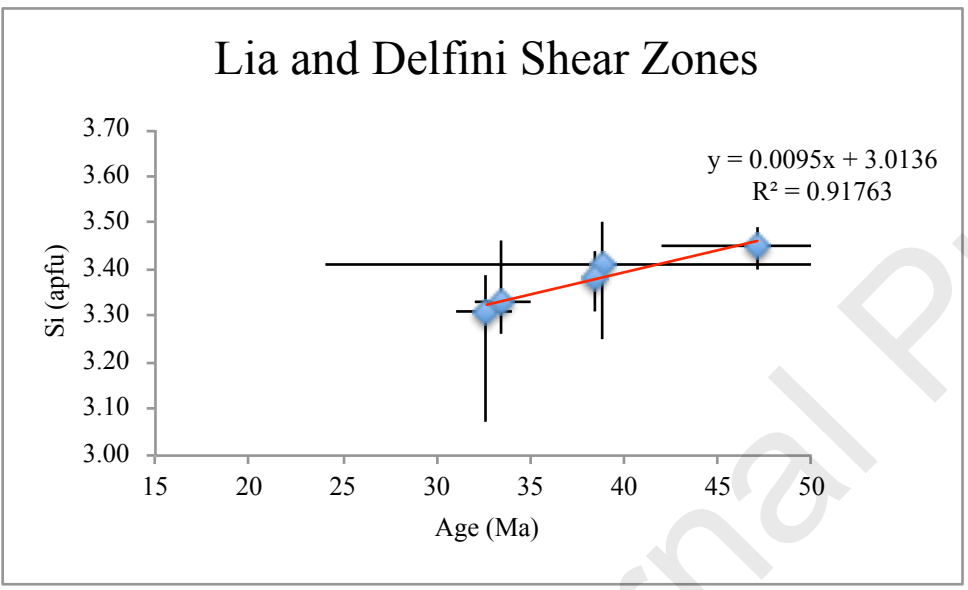

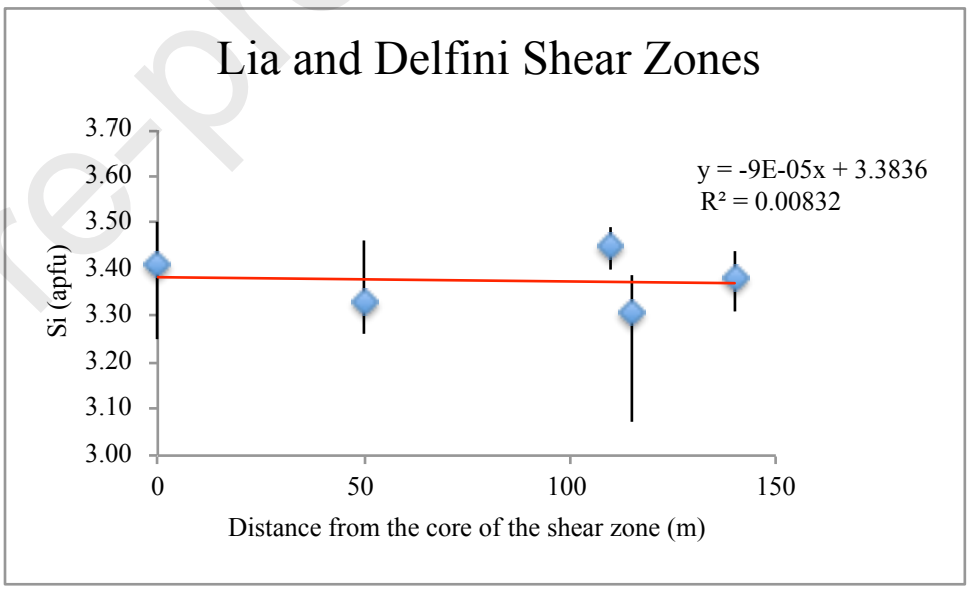

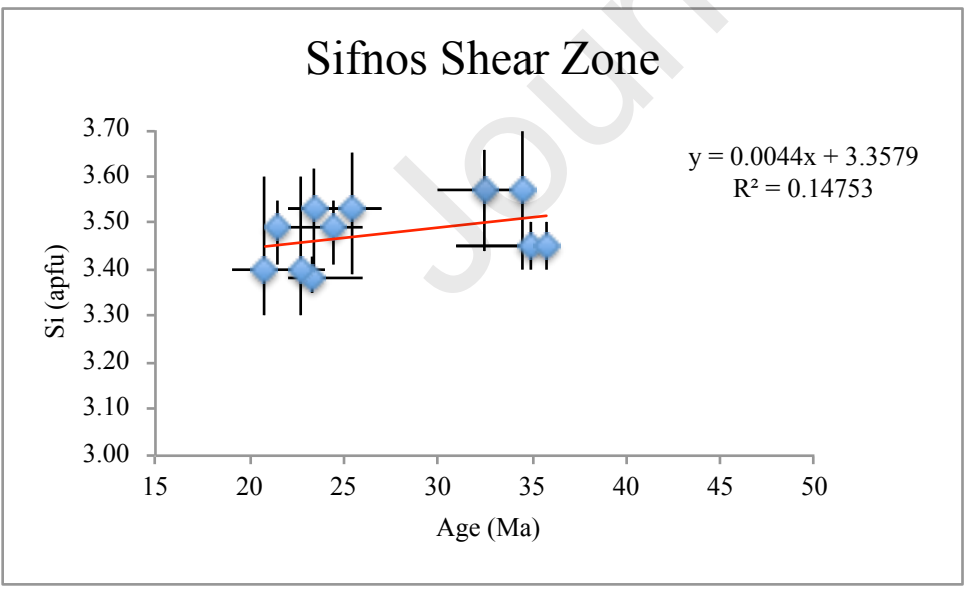

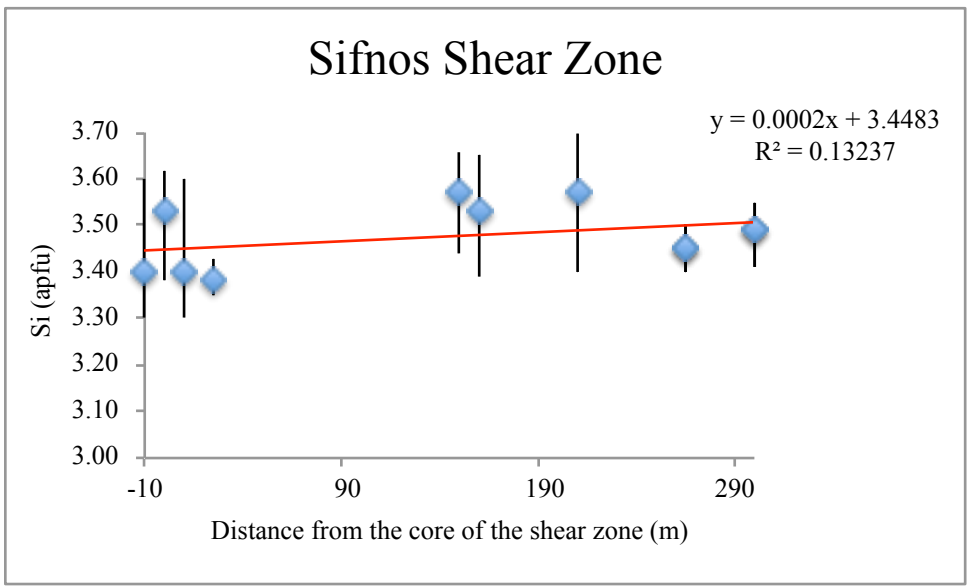

Figure 20

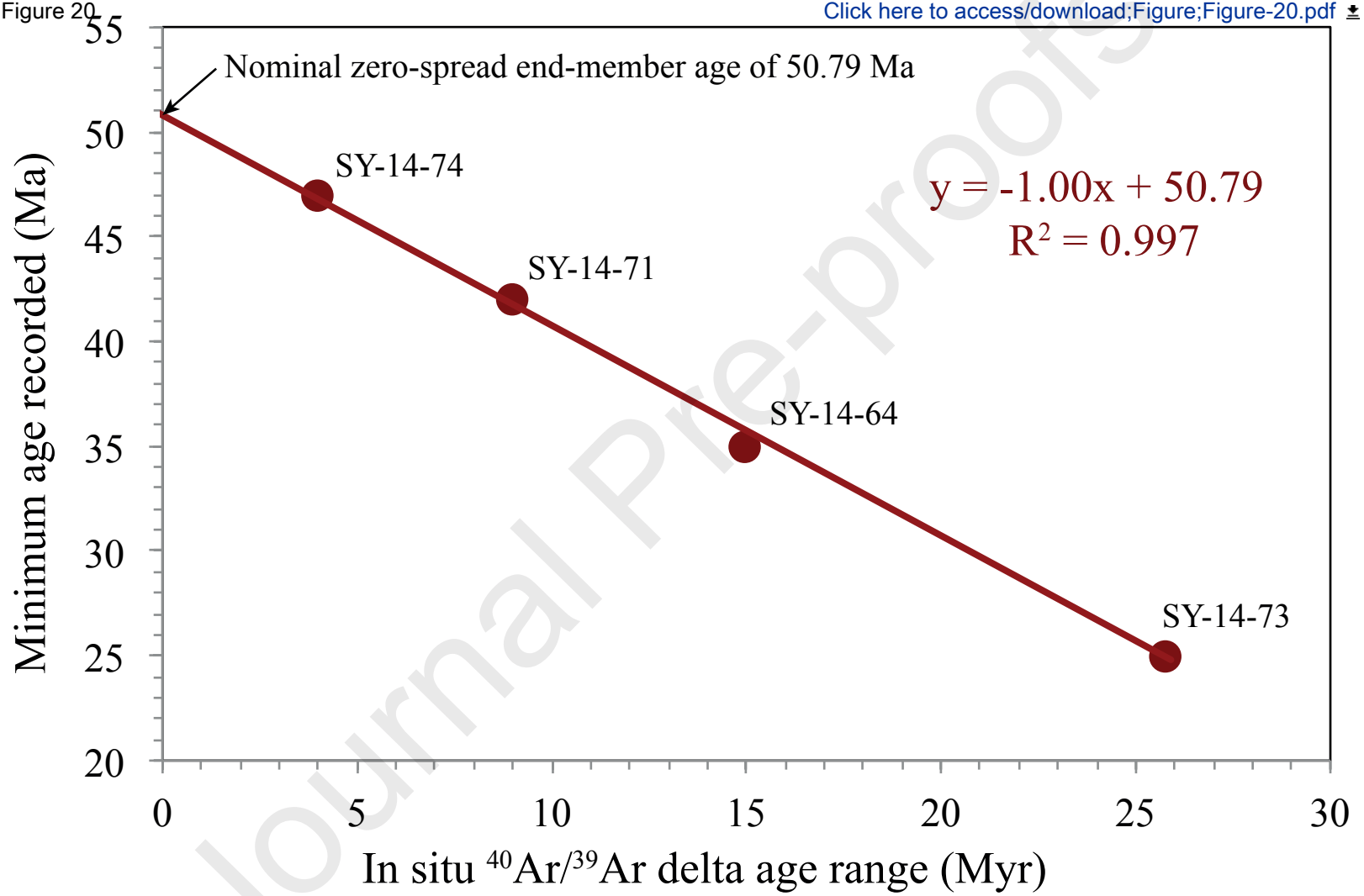

Figure 21

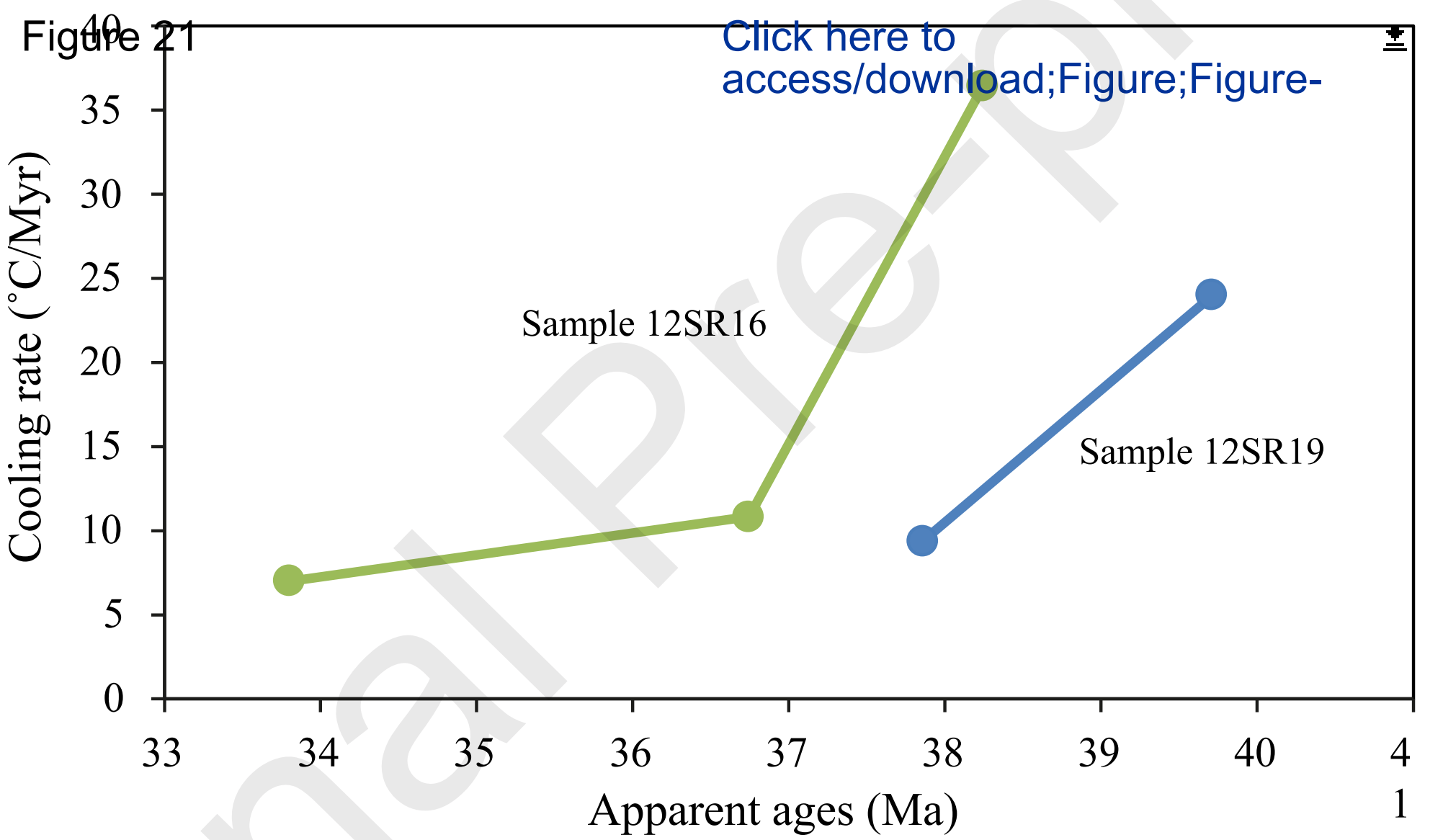

*Declaration of Interest Statement

Declaration of interests

☒ The authors declare that they have no known competing financial interests or personal relationships that could have appeared to influence the work reported in this paper.

☐The authors declare the following financial interests/personal relationships which may be considered as potential competing interests: